Design, Modelling and Analysis of the Discharge of a High-Temperature Concrete Thermal Energy Storage System Coupled to a Power Plant Turbine

Master's Thesis

by

Camilla Nødbak Gade & Stephanie Sigvert Sørensen

June 2017

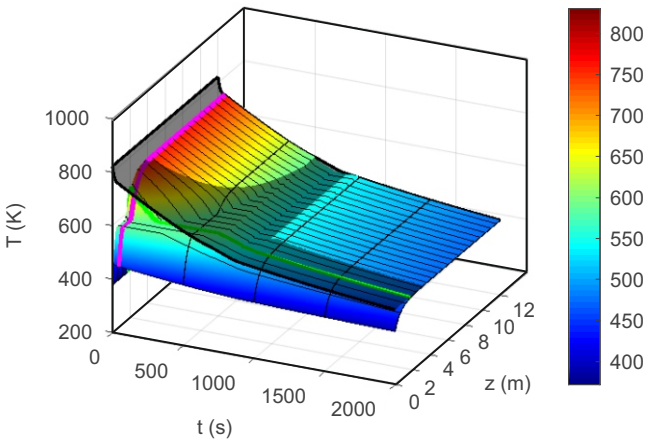

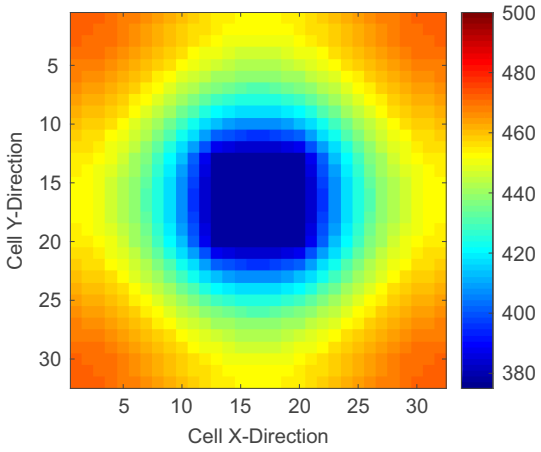

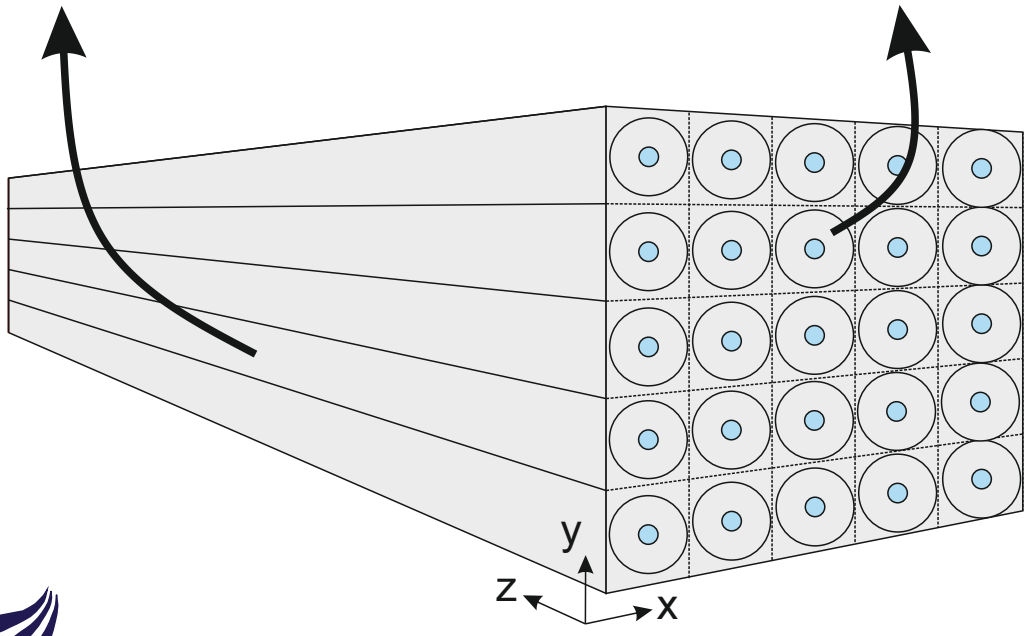

AALBORG UNIVERSITY
STUDENT REPORT

Thermal Energy and Process Engineering
Department of Energy Technology, Aalborg University

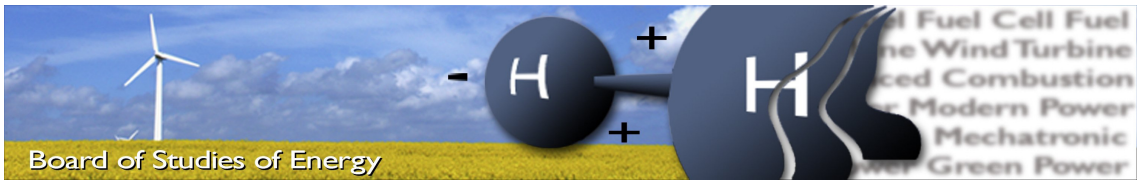

Title:	Design, Modelling and Analysis of the Discharge of a High-Temperature Concrete Thermal Energy Storage System Coupled to a Power Plant Turbine
Semester:	10th
Semester theme:	Master's Thesis
Project period:	01.02.2017 to 01.06.2017
ECTS:	30
Supervisors:	Kim Sørensen & Thomas Condra
Project group:	TEPE4-1002

Camilla Nødbak Gade

Stephanie Sigvert Sørensen

SYNOPSIS:

This Master's thesis concerns the design, modelling and analysis of a thermal energy storage (TES) system using Heatcrete® as storage material and water/steam as heat transfer fluid (HTF). The discharge process of the TES system has been investigated, and the output has been coupled to a simple power plant turbine. Two dynamic models have been developed: a Lumped-Mass-Model and a FVM-Model. The Lumped-Mass-Model simulates the discharge temperatures of the concrete and HTF elements in the pipes. The FVM-Model simulates the temperature gradient throughout the concrete and calculates an average temperature efficiency. The two models are coupled in order to implement the concrete temperature gradient in the Lumped-Mass-Model. Furthermore, different discharge scenarios have been investigated. The thesis concludes that the concrete and HTF temperatures decrease over time, as the TES system is discharged. It is also concluded that the efficiency of the concrete does not affect the heat transfer rate significantly, however it decreases, as the efficiency decreases. Finally, different TES system and turbine outputs are obtained when different scenarios of time and temperature are investigated, and a double size TES system corresponds approximately to the doubled heat transfer rate and turbine output.

Pages, total:	123
Appendices:	A-F
Supplements:	Zip-folder

By accepting the request from the fellow student who uploads the study group's project report in Digital Exam System, you confirm that all group members have participated in the project work, and thereby all members are collectively liable for the contents of the report. Furthermore, all group members confirm that the report does not include plagiarism.

Executive Summary

Modelling of Thermal Energy Storage System

The energy demand, whether residential, public, industrial or others, is generally never steady and requires energy production systems large enough to supply the peak-demand requirements. This typically results in systems often operating at less than full capacity, which results in high and partially inefficient investments.

By implementing an energy storage, a smaller energy production system can operate not *at* but *near* the peak capacity, independent of the instantaneous demands. Energy in excess can then be stored during low-demand periods for subsequent use in high-demand periods. Energy storage thereby offers the possibility for on-demand energy production in peak periods without demanding the peak energy production [Dincer and Rosen, 2011].

This Master's thesis has concerned the design, modelling and analysis of a sensible and passive thermal energy storage (TES) system using a high-temperature concrete mixture (Heatcrete®) as storage material and water/steam as heat transfer fluid (HTF). In the thesis, the discharge process of the TES system has been investigated, and the output of the TES system has been coupled to a simple power plant turbine.

The TES system modelled is inspired by the TES system under development by Aalborg CSP and EnergyNest (see Figure 1), and a simplified TES system (see Figure 2) has been modelled using two different dynamic modelling approaches. The simplifications concern number and location of the concrete elements within the TES system module along with number and size of the pipes.

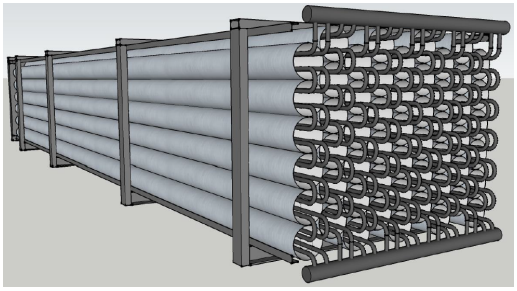

Figure 1. The Aalborg CSP/EnergyNest TES system with 56 concrete elements.

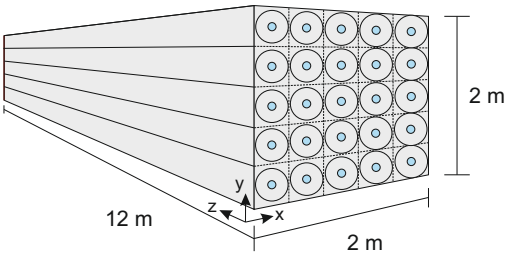

Figure 2. Simplified TES system with 25 concrete elements.

Developed Models and Simulation Results

Firstly, the TES system has been modelled as a lumped mass system, in the y, z-plane, consisting of a lumped concrete block with 25 pipes. This model has resulted in temperature progressions for the concrete and HTF elements along with the system pressure progression, and the turbine work produced over time. Additionally, the TES system (one arbitrary concrete element in Figure 2) has been modelled as finite volumes, in the x, y-plane, in order to study the temperature gradient throughout the concrete block. Besides a temperature gradient over time, the model has resulted in an average efficiency of the concrete block. Results from the two models, termed the Lumped-Mass-Model and the FVM-Model, are given in the figures below.

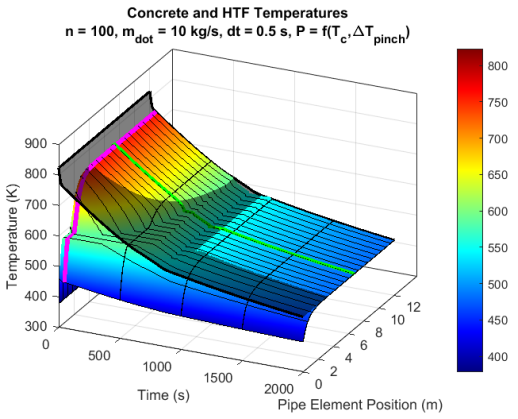

Figure 3. 3D temperature plot in the Lumped-Mass-Model after 2000 s (33 min).

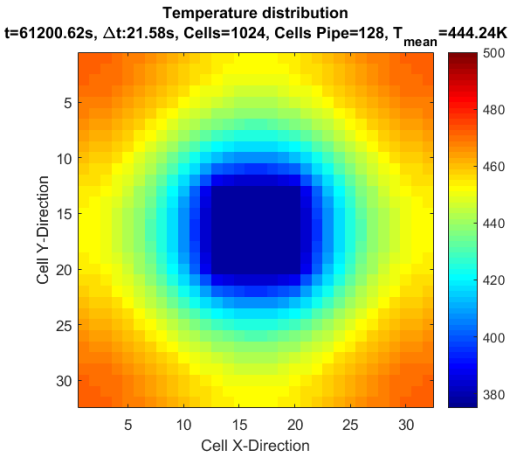

Figure 4. Temperature of the FVM-Model after $\sim 61\,200$ s (17 h).

In Figure 3, the temperature progressions for the concrete and HTF elements are seen after approximately 33 min. The highlighted lines, in **magenta** and **green**, represent a fixed time and HTF element position, respectively. The concrete temperature is seen as a "dark plate" placed partly above the HTF elements. This is due to the lumped mass assumption. In Figure 4, the TES system is shown after approximately 17 h. It should be noted that the discharge times are different in the two models due to different model assumptions. As seen, the FVM-Model applies an additional simplification of replacing the circular concrete element and pipe with squares.

After developing the models, a coupling of the two is analysed in order to study the influence of the temperature gradient, found in the FVM-Model, on the results from the Lumped-Mass-Model. Results from efficiencies of 100% (*i.e.* the lumped mass), 85.92% and 50% are compared. Additionally, several discharge scenarios for the TES system are investigated and analysed concerning mass flow rates, discharge times and TES system sizes.

Thesis Conclusions

- From the Lumped-Mass-Model results, it is concluded that the concrete temperature decreases over time, as expected, since the TES storage is discharged. After approximately 2.78 h, the HTF element temperatures have decreased to the HTF inlet temperature, since no more energy is left in the concrete block.
- From the FVM-Model results, it is concluded that the concrete experiences a decreasing temperature gradient from the outer concrete boundaries towards the centred pipe, as expected. After approximately 34 h, the temperature of the concrete block has decreased to a mean temperature of 388.98 K = 115.83°C. The average efficiency of the FVM-Model is concluded to be 85.92%.
- From the coupling results, it is concluded that the implementation of a temperature gradient decreases the heat transfer rate from the concrete to the HTF elements.
- From the scenario analysis, it is concluded that when discharging to the same temperature, the TES system output varies slightly. However, when discharging to the same time, the short-term TES system has the highest output values. A compromise should therefore be made between the turbine performance and the discharge rate, since the short-term TES system also results in the lowest time range for the pressure decrease.
- When comparing the two different TES system sizes, it is concluded that the double size TES system has a doubled pressure decrease time range and almost doubled amount of heat transferred, however a compromise should be made between the material costs, turbine performance and discharge time.

Preface

This Master's Thesis has been composed by Camilla Nødbak Gade and Stephanie Sigvert Sørensen between February 1st and June 1st 2017 on the final semester of the Master *Thermal Energy and Process Engineering* at Aalborg University.

To obtain the greatest benefit the reader should have knowledge of general thermodynamics, fluid dynamics and heat transfer. During the project the programmes *MATLAB* and *REFPROP* from MathWorks have been used. It is recommended that the reader also has knowledge of these.

Reader Guidelines
Ahead of the report a nomenclature is given alphabetically. The nomenclature is divided into abbreviations, dimensionless numbers, symbols (greek and latin) and subscripts.

Throughout the report literary references are made using the Harvard method, which means the sources are referred to as [Author, Year]. The used sources are listed alphabetically in the back of the report. All sources are listed by author, year and title. Additionally, edition and publisher are given for books, journals for papers and URLs for web pages. Furthermore, lists of figures and tables are given after the bibliography.

Internal references within the report are given according to other chapters and sections within the report. Figures and tables are numbered according to the chapter in which they appear.

Finally, a zip-folder is uploaded together with the report. The folder includes dynamic models (.m), additional scripts used in the project (.m), figures (.png, .pdf and .fig), complete sources named after the Harvard method and a reader guideline. A copy of the Master's thesis is also included in the zip-folder (.pdf).

Acknowledgements
A special thanks is addressed to Jan Kragbæk and Peter Badstue Jensen from Aalborg CSP for their time and inspiration regarding the project proposal. Furthermore, supervisors Associate Professors Kim Sørensen and Thomas Condra are thanked for supervision and feedback. A special thanks is addressed to industrial PhD student Anders Schou Simonsen for assistant supervision and general MATLAB help along with fellow students Marc-André Triebel and Oscar Miralles Perez for inspiration to the FVM modelling.

Nomenclature

Abbreviations

AAU	Aalborg University	(-)
CHP	Combined Heat and Power	(-)
CSP	Concentrated Solar Power	(-)
DLR	Deutsches Zentrum für Luft- und Rumfahrt	(-)
DSG	Direct Steam Generator	(-)
ECO	Economiser	(-)
EVA	Evaporator	(-)
HC	Heatcrete®	(-)
HT	High Temperature	(-)
HTF	Heat Transfer Fluid	(-)
LHS	Latent Heat Storage	(-)
LMTD	Log Mean Temperature Method	(-)
MS	Molten Salt	(-)
PCM	Phase Change Material	(-)
PTPP	Parabolic Trough Power Plant	(-)
SH	Superheater	(-)
SHS	Sensible Heat Storage	(-)
TCHS	Thermochemical Heat Storage	(-)
TES	Thermal Energy Storage	(-)

Dimensionless numbers

Bi	Biot number	(-)
Nu	Nusselt number	(-)
Pr	Prandtl number	(-)
Re	Reynolds number	(-)

Greek symbols

γ	Surface tension	$(\mathrm{N\,m^{-1}})$
ζ	Friction factor	(-)
η	Efficiency	(-)
θ	Weighting parameter	(-)
μ	Viscosity	$(\mathrm{Pa\,s})$
ξ	Layer thickness	(m)
ρ	Density	$(\mathrm{kg\,m^{-3}})$
σ	Stress	$(\mathrm{N\,m^{-2}})$
φ	State variable	Depends on the definition

Latin symbols

A	Area	$(\mathrm{m^2})$
A^*, F	Dimensionless factors	(-)
c_p	Specific heat capacity	$(\mathrm{J\,kg^{-1}\,K^{-1}})$
CV	Control volume	$(\mathrm{m^3})$
dt	Time step	(s)
D	Diameter	(m)
g	Gravitational acceleration	$(\mathrm{m\,s^{-2}})$
E	Energy	(J)
G	Mass flux	$(\mathrm{kg\,s^{-1}\,m^{-2}})$
h	Heat transfer coefficient	$(\mathrm{W\,m^{-2}\,K^{-1}})$
H	Specific enthalpy	$(\mathrm{J\,kg^{-1}})$
k	Thermal conductivity	$(\mathrm{W\,m^{-1}\,K^{-1}})$
L	Length	(m)
m	Mass	(kg)
n	Number of elements	(-)
$\dot{m}$	Mass flow rate	$(\mathrm{kg\,s^{-1}})$
P	Pressure	(bar)
$\dot{q}$	Heat flux	$(\mathrm{W\,m^{-2}})$
$\dot{Q}$	Heat transfer rate	$(\mathrm{J\,s^{-1}})$
r	Radius	(m)
R	Thermal resistance	$(\mathrm{K\,W^{-1}})$
t	Time	(s)

Latin symbols

T	Temperature	(K)
U	Overall heat transfer coefficient	($\mathrm{W\,m^{-2}\,K^{-1}}$)
V	Volume	($\mathrm{m^3}$)
$\dot{W}$	Turbine work produced	(W)
x	Quality	(-)
$\Delta x, \Delta y$	Cell width	(m)

Subscripts

$_1$	Initial	(-)
$_2$	Final	(-)
$_\infty$	Infinity	(-)
$_a$	Actual	(-)
$_c$	Characteristic	(-)
$_{con}$	Concrete	(-)
$_{cond}$	Conductivity	(-)
$_{conv}$	Convection	(-)
$_{elem}$	Element	(-)
$_g$	Gas	(-)
$_{i,in}$	In, inlet	(-)
$_{isen}$	Isentropic	(-)
$_l$	Liquid	(-)
$_{lm}$	Log mean	(-)
$_{o,out}$	Out, outlet	(-)
$_{ref}$	Reference	(-)
$_s$	Surface	(-)
$_{sys}$	System	(-)
$_{tot}$	Total	(-)
$_{turb}$	Turbine	(-)
$_{wall}$	Pipe wall	(-)
$_{wat}$	Water	(-)

Contents

Nomenclature **x**

I Project Introduction **1**

1 Overview of the Master's Thesis **3**

2 Why Energy Storage? **5**
2.1 On-Demand Energy Production 5
2.2 Collaboration Between Aalborg CSP and AAU 6

3 Thermal Energy Storage (TES) **7**
3.1 Storage Technologies 7
3.2 Types of TES-systems 8
3.3 The TES-System Used at Aalborg CSP 10

4 State-of-the-Art **11**

5 Problem Presentation **17**
5.1 Problem Statement 17
5.2 Problem Delimitation 17

II Applied Theory **19**

6 Description of the TES System **21**
6.1 The Aalborg CSP/EnergyNest TES System Design 21
6.2 The Simplified TES System Design Modelled 23
6.3 The Discharge Mode of the TES System 24
6.4 The Processes in the Storage Components 25
6.5 Single- and Multiphase Flow 26

7 Heat Transfer Mechanisms Applied in the TES **29**
7.1 The Conduction and Convection Heat Transfer Mechanisms 29
7.2 Transient Heat Conduction: Lumped System Analysis 31

8 Finite Volume Method (FVM) Theory **33**
8.1 The Finite Volume Method in 2D 33
8.2 The Time-Dependent Finite Volume 33

9 Efficiency Analogy **37**

IIIModelling Approaches **39**

10 Model 1: Lumped-Mass-Model **41**
10.1 Purpose of the Lumped-Mass-Model 41
10.2 Lumped-Mass-Model Assumptions 41
10.3 Lumped Concrete Block Approach 41

10.4 MATLAB Set-Up: The Lumped-Mass-Model Walk-Through . . . 46
10.5 Model Evaluation . . . 47
10.6 Model Validation: The Energy Balance . . . 53

11 Model 2: FVM Model **55**
11.1 Purpose of the FVM-Model . . . 55
11.2 FVM-Model Assumptions . . . 55
11.3 Geometry of the FVM-Model . . . 55
11.4 Boundary Conditions, Weighting Parameter and Time Resolution . . . 56
11.5 The FVM-modelling Approach . . . 57
11.6 MATLAB Set-Up: The FVM-Model Walk-Through . . . 58
11.7 Grid Independence . . . 59
11.8 Model Evaluation . . . 61
11.9 Model Validation: The Energy Balance . . . 62

IV Analysis and Discussion **63**

12 Model Results **65**
12.1 Results from the Lumped-Mass-Model . . . 65
12.2 Results from the FVM-Model . . . 70

13 Model Coupling **73**
13.1 Calculation of the Biot Number . . . 73
13.2 Coupling of the Developed Models . . . 73

14 Discharge Scenarios **77**
14.1 Scenarios Investigated . . . 77

15 Discussion **85**
15.1 Discussion of the Lumped-Mass-Model . . . 85
15.2 Discussion of the FVM-Model . . . 87
15.3 Discussion of the Model Coupling . . . 89
15.4 Discussion of the Charge Mode of the TES System . . . 89

V Project Closure **91**

16 Conclusion **93**

17 Future Work **95**

Literature **96**

List of Figures **101**

List of Tables **104**

Appendix **107**

A Elaboration on TES Technologies and Types **107**

B The Evaporator Parts and Process Explained **111**

C Elaboration on Multiphase Flow **113**

D Elaboration on the Theory Applied in the Lumped-Mass-Model **117**

E Elaboration on the FVM-Theory and Model **119**

F Estimated TES System Material Costs **123**

Part I

Project Introduction

1 Overview of the Master's Thesis

Before opening up the Master's thesis, a report overview is given. The thesis is divided into the parts I-VI, which each have associated chapters. *It should be noted that the problem presentation is in a later chapter (Chapter 5) than is normal practice. This is due to the need for further explanation of thermal energy storing.*

I *Project Introduction*

Chapter 2: This chapter introduces to the topic of this Master's thesis and the collaboration with Aalborg CSP.
Chapter 3 and 4: Chapter 3 introduces and briefly describes the thermal energy storage (TES) technologies and types of TES systems. This leads to the state-of-the-art in Chapter 4, which presents a literature study of 22 scientific papers concerning TES using high-temperature concrete from 2006 to 2016.
Chapter 5: Based on the above, a problem presentation, including statement and delimitation, is presented in this chapter.

II *Theory*

Chapter 6: This chapter gives an overview of the TES system investigated in the Master's thesis, including simplifications of the system, and describes the different processes occurring.
Chapter 7: This chapter briefly presents the theory behind the heat transfer mechanisms occurring in the system. This theory is used to develop the first model in the project (the Lumped-Mass-Model).
Chapter 8: This chapter presents the theory behind the finite volume method, which is used to develop the second model in the project (the FVM-Model).
Chapter 9: This chapter presents the efficiency analogy used to couple the developed models.

III *Modelling*

Chapter 10: This chapter presents the approach used for the Lumped-Mass-Model and gives a walk-through of the model including descriptive figures, a flow diagram and input values along with model evaluation and validation.
Chapter 11: This chapter presents the approach used for the FVM-Model and gives a walk-through of the model including descriptive figures, a flow diagram and input values, along with model evaluation and validation.

IV *Analysis*

Chapter 12: This chapter presents the results obtained from the models presented in Chapter 10 (Lumped-Mass-Model) and Chapter 11 (FVM-Model).
Chapter 13: This chapter presents the approach used for the coupling of the two models along with results hereof.
Chapter 14: This chapter presents different discharge scenarios investigated and the results hereof.

V *Project Closure*

Chapter 15, 16 and 17: Chapter 15 and 16 discusses and concludes the project work, respectively, and Chapter 17 presents possible future work topics.

VI *Appendix*: Elaboration of the chapters 6, 7, 8, 10 and 14.

2 Why Energy Storage?

This chapter opens up the Master's thesis by introducing the need for energy storage and the collaboration between Aalborg CSP and the authors of this thesis from Aalborg University.

2.1 On-Demand Energy Production

The energy demand, whether thermal or electrical, is in general not steady and depends, amongst others, on the behaviour and habits of the citizens. Typically, the energy demand peaks daily, weekly and seasonally, and the variable demand involves both the residential and public sectors as well as commercial, industrial and utility sectors [Dincer and Rosen, 2011].

If no energy storage is implemented in the energy production, a reliable energy availability, in general, requires energy production systems large enough to supply the peak-demand requirements. This typically results in systems operating at less than full capacity most of the time, which results in high and partially inefficient investments [Dincer and Rosen, 2011].

2.1.1 Implementation of an Energy Storage

By implementing an energy storage, a smaller energy production system can operate not *at* but *near* the peak capacity, independent of the instantaneous demands. Energy in excess can then be stored during low-demand periods for subsequent use in high-demand periods. Energy storage thereby offers the possibility for on-demand energy production in peak periods without demanding the peak energy production. The implementation of an energy storage system can furthermore result in significant benefits such as reduced energy costs and consumptions, reduced maintenance costs, reduced equipment size, more effective and efficient equipment utility and increased operation flexibility [Dincer and Rosen, 2011].

Several energy storage technologies exist such as mechanical, chemical, biological, magnetic, thermal and hydrogen storages. Thermal energy storage technology using sensible heat is currently widely investigated, showing promising results, as presented in Table 4.1 page 12. [Dincer and Rosen, 2011] suggests the thermal energy sensible heat storage for fossil-fired power plants. This technology is briefly elaborated in Chapter 3 and Appendix section A.1.

2.1.2 Energy Sources and Energy Storage Applications

The energy source delivering the energy to be stored can be both intermittent renewable energy sources, *e.g.* CSP plants (as seen in Table 4.1 page 12) and wind turbines[1], but also conventional power plants and industrial waste heat can be used [Greiner, 2014]. [Dincer and Rosen, 2011] suggests energy storage applications including utility, industry and co-generation (heat and electricity) along with wind, hydro and solar energy sources.

If a renewable energy source is connected to the energy storage, the energy production typically depends on the weather conditions, which do not necessarily follow the energy demand. A conventional power plant, however, will always typically be able to fulfil the energy demand but might have demands to reduce costs, equipment size etc.

[1] Projects from DTU and Siemens: [McGhie, 2016], [Wittrup, 2014], [Wittrup, 2016].

2.2 Collaboration Between Aalborg CSP and AAU

This Master's thesis is written in collaboration with Aalborg CSP, which is a leading company within the development and supply of innovative renewable technologies. Aalborg CSP is acknowledged for their experience within concentrated solar power (CSP) plant technologies but has several other business areas with thermal energy storage (TES) being one of them[2] [Aalborg CSP, 2017a].

During the recent years, Aalborg CSP has collaborated with the Norwegian company EnergyNest on developing a thermal energy storage using high-temperature steam as heat transfer fluid and Heatcrete®, a special concrete mixture, as storage material [Aalborg CSP, 2017b]. During the Spring of 2017 Aalborg CSP has entered a collaboration with Aalborg University about developing a TES for the Danish CHP plant, Nordjyllandsværket.

Ahead of the project start-up, a project proposal has been given from Aalborg CSP regarding their TES system under development using high-temperature concrete and water/steam as heat transfer fluid (HTF). This thesis has taken inspiration from this project proposal, and Aalborg CSP has, during the project period, provided further understanding of the TES system.

In the following chapters, TES technologies and types will be explained briefly, and a state-of-the-art study within this topic is presented.

[2] Aalborg CSP business areas: CSP power plant technologies, integrated energy systems, solar district heating, industrial solar technologies and thermal energy storage [Aalborg CSP, 2017a].

3 Thermal Energy Storage (TES)

This chapter briefly presents different TES technologies and types. The advantages and disadvantages of these are presented in tables. The technologies and types are further elaborated in Appendix A. Additionally, the TES technology and materials used at Aalborg CSP are presented.

3.1 Storage Technologies

In the following, three storage technologies are presented: sensible, latent and thermochemical heat storage. Each technology is briefly explained, and the advantages and disadvantages are given. An overview of the three technologies is given in Figure 3.1.

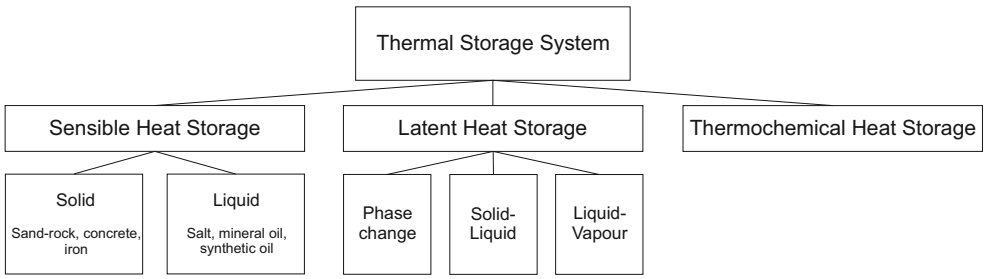

Figure 3.1. Overview of the three TES technologies.

From Figure 3.1 it is seen that sensible heat storage is divided into solid and liquid storage materials, and latent heat storage is divided into phase change, solid-liquid and liquid-vapour transitions. The storage technologies, including materials, are briefly explained below and further elaborated in Appendix A.

3.1.1 Sensible Heat Storage (SHS)

Sensible heat storage (SHS) is a technology in which the thermal energy is stored during changes of temperatures of a solid or liquid thermal storage material [Tian and Zhao, 2012]. The temperature is increased during charging of the storage and decreased when the stored energy is used during discharging. The storage system consists mainly of three components: a container, a storage material and inlet/outlet devices. The container, which is typically a tank, must retain both the storage material and prevent thermal energy losses, since it is desired to have a temperature change across the storage [Gil et al., 2009].

3.1.2 Latent Heat Storage (LHS)

Latent heat storage (LHS) is a technology in which the thermal energy is stored almost isothermally in substances as the latent heat of phase change, as heat of fusion (solid-liquid) or as heat of vaporisation (liquid-vapour). Today, the heat of fusion is mainly used, and the substances used for this technology are phase change materials (PCMs) [Gil et al., 2009]. The PCMs can store and release heat when their phase structures are re-formed during melting and solidification processes [Tian and Zhao, 2012].

LHS systems has a much higher storage density than SHS systems, as the phase-transition enthalpy of PCMs typically are higher than sensible heat [Tian and Zhao, 2012]. Furthermore, the LHS

systems using PCMs can be reduced in size compared to single-phase SHS system. The energy can thus be stored in relatively small tanks, which results in low storage costs. The heat transfer design and selection of material is, however, more difficult, and it is shown from experience with low-temperature salt, that the material performance may degrade after several freeze-melt cycles [Gil et al., 2009].

3.1.3 Thermochemical Heat Storage (TCHS)

Thermochemical heat storage (TCHS) is a technology in which the thermal energy is absorbed or released in some special chemicals, when the chemicals break or form certain chemical bonds during endothermic and exothermic reactions [Tian and Zhao, 2012]. When charging, heat induces the chemical bonds to break and the chemicals are subsequently stored separately. When discharging, the chemical bonds re-form, releasing the heat [Jerz, 2015].

3.1.4 Advantages and Disadvantages of SHS, LHS and TCHS

The advantages and disadvantages of the three previously presented technologies are listed in Table 3.1.

	Advantages	**Disadvantages**
SHS	Packed beds favour thermal stratification; Low cost	Possibility of a high pressure loss and parasitic energy consumption; Requires non-mixing mechanism
LHS	Almost isothermal process; High storage density compared to SHS; Can be stored in relatively small tanks	The heat transfer design and selection of material can be difficult; Low thermal conductivity; Requires heat transfer enhancement technologies
TCHS	Relatively low costs; High storage density compared to the other two; Indefinitely long storage duration near ambient temperature	Requires chemical reversibility, large chemical enthalpy change and simple reaction conditions; Not yet extensively researched; Complex; Limitation regarding applications

Table 3.1. Advantages and disadvantages of SHS, LHS and TCHS.

3.2 Types of TES-systems

The different types of TES-systems are briefly presented in the following and further elaborated in Appendix A. Active systems are presented first, which can be either direct or indirect, subsequently passive systems are presented. At the end of this section, the advantages and disadvantages of the presented types are given in a table. An overview of the different types of systems are given in Figure 3.2.

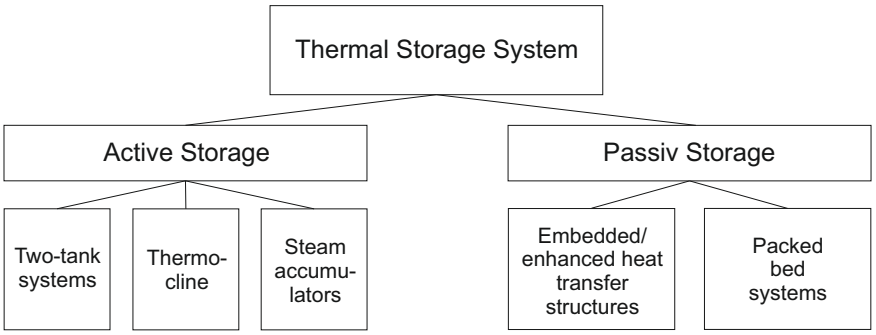

Figure 3.2. Overview of the active and passive TES-systems.

From Figure 3.2 an overview of the active and passive TES-systems is given. It is seen that an active system can be a two-tank system, a thermocline system or steam accumulators. Furthermore, it is seen that passive systems can be systems with embedded or enhanced heat transfer structures or packed bed systems.

3.2.1 Active Storage

An active TES system is a system, where the storage material is a fluid flowing between tanks. The type is characterised by forced convection heat transfer into the storage material. The system can be either direct or indirect and can use one or two tanks as storage media [Gil et al., 2009]. In direct systems, the storage material is also used as the HTF. In indirect systems, the storage fluid and HTF are not the same, and there is a need for an additional heat exchanger [Kuravi et al., 2013].

3.2.2 Passive Storage

A passive TES system is a system, where the storage material is a solid and the HTF only passes through the storage material when charging and discharging. A major parameter in this type of system is the arrangement for the HTF to flow through the storage material, since it dictates the heat transfer in the unit. Passive systems are often dual storage systems, which is also called regenerators [Gil et al., 2009]. The solid in a passive system may be inexpensive solids like rocks, sand or concrete in SHS systems and PCMs in LHS systems [Kuravi et al., 2013].

3.2.3 Advantages and Disadvantages of Active and Passive Systems

The advantages and disadvantages of the different types of TES-system are listed in Table 3.2.

	Advantages	**Disadvantages**
Active	*Two-tank systems*: Cold and hot materials are stored separately; Low-risk approach; Possibility to raise the output temperature to 450-500°C	*Two-tank systems*: High costs of the HTF, storage material and heat exchangers; A need for two tanks; Relatively small temperature difference
	Thermocline systems: Possibility of reducing the costs due to one tank; Low costs of filler materials	*Thermocline systems*: Relatively high freezing points; Difficulty of separating the fluids; Losses due to high outlet temperatures; Requires controlled discharge; Requires methods to avoid fluid mixing; Complex design
	Steam accumulators: Widely investigated and used for fossil fuel fired power plants	*Steam accumulators*: Only saturated steam is obtained; Design and operation needs to meet the turbine cycle needs
Passive	Low cost; High heat transfer rates due to good contact; Facility of handling of the material; Low degradation of the heat transfer	High costs of heat exchangers; Possibility of a more problematic and low heat transfer

Table 3.2. Advantages and disadvantages of different types of TES-system.

3.3 The TES-System Used at Aalborg CSP

In the TES system by Aalborg CSP a sensible, passive storage system is currently being developed. The system is a direct-steam-to/from concrete storage system, which indicates that the storage material is concrete (Heatcrete®), and the HTF is water/steam [Aalborg CSP, 2017b]. The storage system is sketched in Figure 3.3.

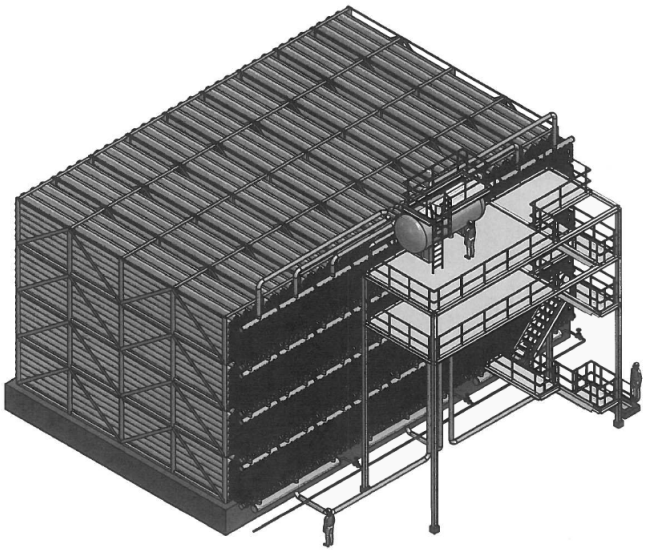

Figure 3.3. The TES system developed at Aalborg CSP [Jensen, 2017].

The figure illustrates the structure of the storage system, which can be seen as a concrete block with an "embedded" boiler. The system consists of different processes in which the steam/water is heated/cooled by the concrete surrounding it. The system is further described in Chapter 6, where the system design, materials and processes are presented and explained.

This chapter has presented different TES technologies, materials and types along with the TES system used at Aalborg CSP. In the following chapter a state-of-the-art within the above topics is presented.

4 State-of-the-Art

This chapter presents a literature study conducted in order to investigate the state-of-the-art within the topic of thermal energy storage using high temperature-concrete mixtures. 22 scientific papers have been studied in total concerning reviews, storage concepts and materials, modelling, projects and concrete mixtures. For the literature study five published reviews have been addressed: [Herrmann and Kearney, 2002], [Gil et al., 2009], [Medrano et al., 2009], [Tian and Zhao, 2012], [Kuravi et al., 2013]. These are briefly summarised in the following.

[Herrmann and Kearney, 2002] briefly addresses the state-of-the-art of parabolic trough power plants using thermal energy storage before 1990 and give a detailed state-of-the-art between 1990 and 2002. Before 1990 only three storage systems were fully investigated: dual medium sensible heat systems, sensible heat molten salt systems and phase-change systems. Between 1990 and 2002 an overview of the TES progression is given in which the three technologies using concrete, PCMs and chemical reactions as storage media are investigated. Between 1991 and 1994 successful results from laboratory-scale testing of concrete were achieved by ZSW[1]. Additionally, experience from the Solar Two project that operated from 1995 to 1999 is presented.

[Gil et al., 2009] and [Medrano et al., 2009] comprise part 1 and 2 of a state-of-the-art between 1981 and 2009. Part 1 primarily concerns concepts, materials and modellization whilst part 2 concerns experiences from 11 projects[2] that are or has been in use along with two proposals for future approaches. In the time period investigated only liquid SHS systems have been in operation, and most concepts have been active systems. Two types of molten salts are typically used but new salt mixtures are currently being investigated. Recently, concrete and castable ceramics have been investigated showing promising results.

[Tian and Zhao, 2012] addresses the state-of-the-art between 1984 and 2012. The paper presents a review of solar collectors divided into non-concentrating collectors and concentrating collectors. Additionally, the paper gives a review of thermal energy storage systems for which design criteria, materials and heat transfer enhancement technologies are presented. Finally, an overview of existing and future solar power stations is given. Storage materials have been compared, and it is concluded that molten salts are the ideal high-temperature storage material for this study.

[Kuravi et al., 2013] concerns state-of-the-art up to 2013. The review is divided into plant, component and system level considerations and discusses TES designs and power plant integration. The case study by [Gabbrielli and Zamparelli, 2009] is discussed, in which an optimum tank design is presented. Furthermore the paper addresses modelling approaches on the system level and development activities in TES, among others. It is assessed that encapsulated PCMs is a promising technology to be commercial in the near future, and it is concluded that a solution could be the combination of different types of storage technologies.

Apart from the above reviews, 14 scientific papers concerning projects have been studied. Key information are presented in Table 4.1. The following abbreviations are used: PTPP for "parabolic trough power plant", DSG for "direct steam generation", HT for "high-temperature", MS for "molten salt" and PCM for "phase change material". If the system capacity is not applicable, the system power is given in (). The presented papers are further discussed below the table.

[1] ZSW: Center for Solar Energy and Hydrogen Research in Stuttgart, Germany.

[2] A DSG-project in Spain, "PS10" in Spain, "Solar One" in California, "SEGS I" in California, "Solar Two" in California, "Solar Tres" in Spain, "Andasol I" in Spain, a CLHS-project by Luz, "WESPE" in Spain (funded by DLR), a prototype in Germany (funded by DLR) and a pilot plant by ANU in Australia.

Author, year	Project, Location	Type	Technology	Storage material	HTF	Capacity (or Power)	Temp. (°C)	Notes
[Laing et al., 2006]	WESPE, Spain	PTPP	Sensible, solid	Ceramic and HT-concrete	Synthetic oil	350 kWh	340-390	Pilot-scale
[Laing et al., 2008]	WANDA, Germany	PTPP	Sensible, solid	Liquid salt	Synthetic oil	N/A	350-390	Lab-scale
[Laing et al., 2009]	Test setup, Germany	PTPP	Sensible, solid	HT-concrete	Thermal oil	1100 MWh	300-400	Lab-scale
[Laing et al., 2010a]	Litoral, Spain	PT-DSG-PP	Combined sensible/PCM	HT-concrete and PCM	Water/steam	1 MWh	up to 400	Pilot-scale
[Laing et al., 2010b]	Litoral, Spain	PT-DSG-PP	Combined sensible/PCM	HT-concrete and PCM	Water/steam	1 MWh	up to 500	Pilot-tested up to 400°
[Bai and Xu, 2011]	Based on Dahan Power Plant, China	Solar power tower	Sensible, solid	HT-concrete	Steam	(1 MW)	from 390	Simulation of discharge
[Laing et al., 2012]	Test setup, Germany	PTPP	Sensible, solid	HT-concrete	Thermal oil	1100 MWh	200-500	Tested up to 400°C
[Wu et al., 2013]	None	CSP system	Sensible, solid	HT-concrete	Thermal oil	N/A	290-390	Simulation of discharge
[Salomoni et al., 2014]	SolTeCa-project, Italy	CSP system	Sensible, solid	HT-concrete	Water	(4500 kW)	80-300	Simulation
[Bergan and Greiner, 2014]	Pilot plant, Abu Dhabi	Beam-Down	Sensible, solid	HT-concrete	Synthetic oil	1 MWh	up to 400	Pilot-scale
[Miro et al., 2014]	Projects by [1], [2], [3][3]	CSP system	Sensible and latent	HT-concrete, MS, MS/PCM	N/A	350 kWh, 600 MWh, 100 kWh	up to 390, 200-550, N/A	Pilot-scale, real system, pilot-scale
[Jian et al., 2015]	None	PTPP	Sensible, solid	HT-concrete	N/A	N/A	290-390	Simulation
[Martins et al., 2015]	Pilot plant, Abu Dhabi	Beam-Down	Sensible, solid	HT-concrete	Synthetic oil	1 MWh	393	Using Heatcrete®
[Hoivik et al., 2016]	Pilot plant, Abu Dhabi	Beam-Down	Sensible, solid	HT-concrete	Synthetic oil	1 MWh	up to 393	Using Heatcrete®

Table 4.1. State-of-the-art between 2006 and 2016.

[Laing et al., 2006] described the WESPE-project, which researched two solid media SHS materials: castable ceramic and high-temperature concrete. The focus of the project was to develop a cheap and efficient storage material, and it was concluded that both investigated materials were suitable. After 60 cycles, no degradation of heat transfer was found between the heat exchanger and the storage materials, respectively. However, high-temperature concrete was concluded to be more favourable due to *"lower costs, higher material strength and easier handling"*.

Two years later, [Laing et al., 2008] published the research from the follow-up project WANDA, which focus was to reduce the cost of the heat exchanger along with an analysis, including cost assessment, of concepts of modular storage operation. Tubeless and encapsulated storage designs were investigated along with enhancements of the heat transfer. [Laing et al., 2008] concluded that there are several ways to improve the performance of the storage but most of the investigations do not improve the economical aspect of the storage. It was assessed that the tube register with straight parallel tubes, without additional structures, was the best structural solution.

The following year, [Laing et al., 2009] built a test setup in Stuttgart, Germany, for live tests and further improvements of the storage material, storage capacity, thermal conductivity and handling of vapour pressure. In this test setup, cost reductions in the heat exchanger and storage material were the major focus. The first test conducted failed, since the test module was damaged due to insufficient permeability of the concrete. This led to an improvement of the concrete mixture, for which a successful start-up and operation of the test module was achieved. Based on experimental tests up to 400°C it was concluded, that the concrete storage technology investigated was qualified for storing sensible heat. Furthermore, it is concluded that the design using modules makes it possible to scale the storage module from kWh to GWh, and a storage suggestion for an ANDASOL-type parabolic trough power plant in Spain, including total price, was given.

[Laing et al., 2010a] and [Laing et al., 2010b] both presented a TES that combined SHS and LHS units (published in two different journals). The papers presented a three-part storage system in which the SHS uses concrete as storage material for the preheating and superheating of water and steam, respectively, and a PCM storage was used for evaporation. [Laing et al., 2010a] used pinch analysis to dimension the sensible and latent components and presented both laboratory-scale and pilot-scale test modules. [Laing et al., 2010b] only elaborated the pilot-scale test module and otherwise referred to the work in [Laing et al., 2010a]. The papers concluded that the three-part storage system was a promising option for storing thermal energy in DSG power plants. After 172 cycles, no degradation was found in the PCM-module, and the HT-concrete was found suitable as SHS material up to 500°C. During publication, a storage system at the power plant Litoral in Spain was built based on the research of the combined sensible and LHS systems presented in the papers.

[Bai and Xu, 2011] analysed a two-stage TES system consisting of a HT-concrete storage stage and a LT-storage stage using steam accumulation. The paper was based on the first Chinese 1 MW solar power tower demonstration plant, however, with a concrete storage system instead of a HT-oil storage system. A numerical simulation based on the conservation principle of mass and energy was developed, and the thermal performance of the system was analysed. Different thermal conductivities of the concrete along with different discharge times was investigated. It was concluded that the performance of the concrete storage unit was affected by the thermal conductivity of the material and the spacing between the steel tubes. The higher the conductivity, the more uniform the temperature distribution, thus the higher the energy efficiency. Regarding spacing, it was concluded that the smaller the distance between the tubes, the more metal tubes are needed for reaching the same capacity, thus increasing the costs of the system. Furthermore, it was concluded that heat behaviour in the concrete was directly affected by the discharge time of the steam accumulator.

[3] [1] [Laing et al., 2006], [2] [Gabbrielli and Zamparelli, 2009] and [3] [Bayon et al., 2010].

[Laing et al., 2012] analysed storage material aspects and system performance using test modules up to 500°C. Mass losses at different temperatures were investigated and oven experiments of concrete mixtures were analysed and compared with measurements from the test facility in Stuttgart presented in [Laing et al., 2009]. The paper referred to the ANDASOL-type parabolic trough power plant, as [Laing et al., 2009], and a system simulation of the annual electricity generation was presented. It was concluded that up to 150°C the mass losses were dominated by evaporating water, and in the range 450-500°C the mass losses were dominated by the aggregates. After a given time and number of thermal cycles, the mass loss and strength values from the oven experiments and strength measurements stabilised. The simulation results showed that both the energy accumulation and electricity generation could be increased by controlling the mass flow rates when comparing to the reference case.

[Wu et al., 2013] investigated how the thermal performance of a tank-type concrete TES was affected by the concrete structure. Four typical concrete structures were studied, and the thermocline behaviours during discharge were analysed by changing two variables: feature size and fluid inlet velocity. The lumped mass method was used, and from this analysis the discharge efficiencies and times were found. The four structures resulted in different thermoclines, and it was concluded that the packed bed structure had the best thermal performance, since this structure had the thinnest thermocline region. Additionally, it was concluded that the larger the feature size, the lower the discharge efficiency. The fluid inlet velocity only affected the packed bed structure slightly, and the remaining structures more notably.

[Salomoni et al., 2014] presented concrete storage design guidelines along with guidelines for integration into a solar plant. Simplified procedures were used for a first module design, and the finite element method (FEM) was used to check and upgrade the design. During the publication, the authors planned to start up an experimental phase on a scaled storage prototype, which would be used to complete the setup, development and integration of the storage. It has not been possible to find any further information on whether this plan has been accomplished.

[Miro et al., 2014] investigated the three different TES systems presented by [Laing et al., 2006], [Gabbrielli and Zamparelli, 2009] and [Bayon et al., 2010] concerning SHS using concrete, SHS using molten salt and LHS using molten salt, respectively. In [Miro et al., 2014] the environmental impact was accounted for by calculating the embodied energy in the components of the systems. The calculations of the three TES systems were compared, since the dimensions of all three systems underwent a normalisation keeping the same designs and operation temperatures. [Miro et al., 2014] concluded that SHS using concrete had the least impact on the environment, while the remaining two had a higher impact primarily due to the nitrate mixture in the storage material.

[Bergan and Greiner, 2014], [Martins et al., 2015] and [Hoivik et al., 2016] all concern the pilot plant at the Masdar Institute of Science and Technology in Abu Dhabi built in collaboration with EnergyNest.

[Bergan and Greiner, 2014] was published before the final construction of the plant and described the technology behind the TES system and the building of the pilot plant. During the Autumn of 2014 the construction was planned to be finished, which the authors found has been accomplished.

[Martins et al., 2015] tested the concrete mixture Heatcrete® proposed by EnergyNest and compared concrete material characteristics from previous tests by [Laing et al., 2012] (DLR) and [John et al., 2013] (University of Arkansas) with Heatcrete®. Furthermore, the mechanical properties of Heatcrete® were tested based on the knowledge of possible mechanical issues found by DLR and University of Arkansas. The results were planned to be compared to real experimental results from the pilot plant, which started operating in the beginning of 2015. Furthermore, [Martins et al., 2015] presented the solar testing facility and the hot-oil loop design. As [Laing et al., 2009], [Martins et al., 2015] concluded that a TES system using concrete is an attractive

alternative for storing sensible heat, and laboratory and prototype tests proved Heatcrete® to be thermally and mechanically superior.

[Hoivik et al., 2016] presented experimental results from the now operating pilot plant in Abu Dhabi. Simulations of the TES system performance were made prior to the operating plant results, and good agreement between simulation and experimental results was found. The EnergyNest simulation tool was concluded to have a high degree of accuracy and has therefore been used to simulate larger storage systems, which was compared to conventional two-tank molten salt storage systems. The simulation tool indicated that the system performance can be improved by using the EnergyNest storage system.

[Jian et al., 2015] has developed a 1D-unsteady model for a cylindrical TES unit based on a modified lumped mass method. Furthermore, they proposed a control strategy for a modular charging/discharging in order to improve the use of the solid storage material. The control strategy aimed at a higher storage material temperature after charge and a lower temperature after discharge. It was concluded that the use of the storage material can be increased by 14% using this strategy. The results were concluded promising and feasible in regard of using the modular control strategy mode.

Additionally, three scientific papers concerning concrete mixtures and cracking have been found: [John et al., 2013], [Shi et al., 2014] and [Skinner et al., 2014].

[John et al., 2013] experimentally investigated the mechanical and thermal properties of 26 concrete mixtures along with their compatibility with molten salt in molten salt baths. The paper concluded the mixtures 15 and 16[4] to be the best. However, further investigation was required.

[Shi et al., 2014] compared a numerical and experimental study of composite concrete with PCMs and concluded that the effective thermal conductivity of the concrete decreased with an increase of porosity of paraffin or basalt fiber.

[Skinner et al., 2014] experimentally investigated the formation of cracks in concrete. Two types of interface materials and a helical fin configuration were tested, and a 2D FEM model was developed to study the interface stress. It was concluded, that fibered past reduced the cracks, however not as much as desired. The fins increased the rate of heat transfer, however large cracks formed at the fin-to-tube interface.

A state-of-the-art within the topic of thermal energy storage using HT-concrete mixtures has now been presented. It is found, that several of the studied scientific papers conclude HT-concrete mixture to be a promising potential for being storage material in future SHS systems, compared to molten salt that previously has been widely used. The latest findings within the development of HT-concrete mixtures is Heatcrete® by EnergyNest, which has recently been tested by [Martins et al., 2015] and [Hoivik et al., 2016], partly in the pilot plant at the Masdar Institute of Science and Technology in Abu Dhabi.

In the following chapter, the problem presentation of the Master's thesis will be given.

[4] The mixtures contained various amounts of sandstone and washed river sand as fine aggregates [John et al., 2013].

5 Problem Presentation

This chapter presents the problem statement and the problem delimitation for this Master's thesis.

5.1 Problem Statement

In this thesis a concrete TES-system using water/steam as HTF and Heatcrete® as storage material is designed, modelled and analysed for the purpose of discharging surplus thermal or electrical energy from the TES system to the location of use. The thesis focuses on the configuration of the economiser, evaporator and superheater components in the TES system seen in Figure 6.8 page 24.

The main objectives of the thesis can be summarised to:

- Dynamic modelling of the TES system
  - Dynamic modelling of temperature progressions, during discharge, within the three components (the Lumped-Mass-Model)
  - Dynamic modelling of the temperature gradient, during discharge, from the internal pipe throughout the concrete block using FVM (the FVM-Model)
  - Dynamic modelling of temperature progressions within the three components from the Lumped-Mass-Model including the effects from the temperature gradient as an efficiency from the FVM-Model
- Analysis of different discharge scenarios for the designed TES system
  - Analysis of the discharge process with initial temperatures of $T_{con} = 823.15\,\mathrm{K} = 550°\mathrm{C}$ and $T_{wat} = 378.15\,\mathrm{K} = 105°\mathrm{C}$

5.2 Problem Delimitation

This Master's thesis only focuses on designing, modelling and analysing the discharge mode of the investigated TES system (the charge mode is only considered briefly in Chapter 15). Nordjyllandsværket, which is the intendent recipient of the discharged energy, is not further described, and Heatcrete® is not further analysed apart from what is found in the references and presented in the chapters 4 and 6. The thesis does not model nor explain the components before, after or in-between the economiser, evaporator and superheater parts in the TES system (apart from the steam drum, which is briefly described in Appendix B.1). Sensible, latent and thermochemical TES-systems are not further explained than what is briefly presented in the chapters 3 and 4 along with Appendix A. In the modelling of the TES system, the concrete is assumed to have a constant specific heat, the heat loss in the TES system is assumed to be less than 1% of the storage capacity, and the contact resistance between the concrete and the HTF pipe is assumed to be zero [Condra, 2017]. Additionally, the practical layout of the Rankine cycle is not considered.

The following chapters present the TES system investigated and the theory applied in order to model the TES system dynamically.

Part II

Applied Theory

6 Description of the TES System

This chapter introduces the TES system investigated and the technology behind it. In the following, descriptions of the Aalborg CSP/EnergyNest TES system and the simplified TES system along with components and processes are given.

6.1 The Aalborg CSP/EnergyNest TES System Design

The TES system designed by Aalborg CSP/EnergyNest is the system considered in this project. This system is basically a concrete storage, using the material Heatcrete®, with integrated heat exchangers cast into the concrete. The design of the system is modular, which makes it possible to scale the system [Hoivik et al., 2016]. The scalable Aalborg CSP/EnergyNest TES system is illustrated in Figure 6.1 [Hoivik, 2016].

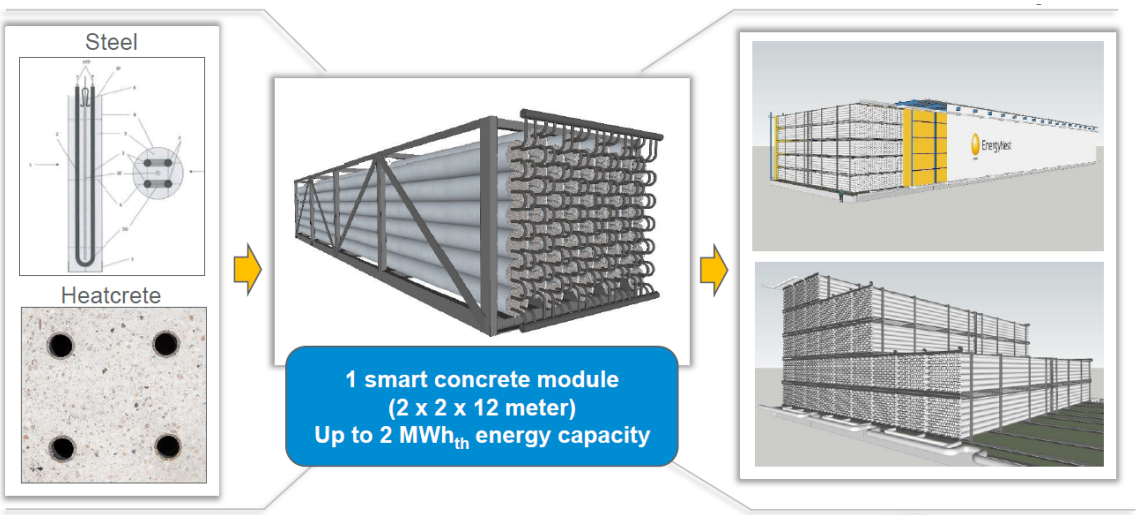

Figure 6.1. Illustration of the Aalborg CSP/EnergyNest TES system design [Hoivik, 2016].

In more detail, the TES system consists of [Hoivik et al., 2016]:

- Steel frames (called "cassettes") with multiple cylindrical heat exchanger elements inside. The cassettes are dimensioned to fit into standard containers.
- Tubes inside the elements, which are configured with parallel U-shaped tubes in order for the HTF to flow in and out of one element as seen to the left in Figure 6.1. This minimises axial thermal stress, since the dominating temperature gradient is in the radial direction.
- Modules, which are the cassettes cast with the concrete material Heatcrete®. Several modules form a block, and several blocks form a complete storage system as seen to the right in Figure 6.1 [EnergyNest, 2017].
- 24 modules are placed, in series, on thermally insulated loadbearing foundation constructed in Foamglas®.
- Rockwool insulation surrounds the modules for thermal insulation.

The Aalborg CSP/EnergyNest TES system is further illustrated in the figures 6.2 and 6.3.

Figure 6.2. Cross-sectional view of a cylindrical concrete element [Hoivik et al., 2016].

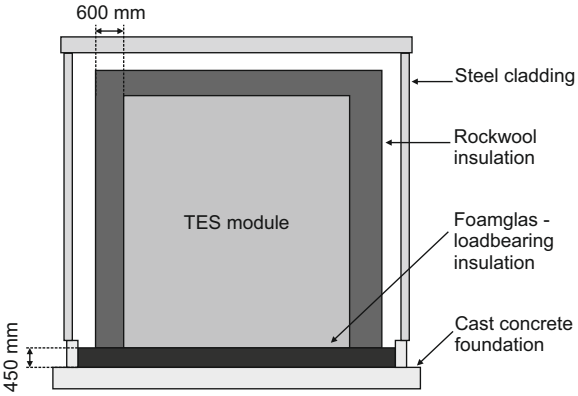

Figure 6.3. Illustration of the Aalborg CSP/EnergyNest TES system, inspired by [Hoivik et al., 2016].

In Figure 6.2 a cross-sectional view of a cylindrical concrete element is shown. It is possible to see, how the tubes are cast into the Heatcrete®. In Figure 6.3 the TES system is illustrated with some dimensions and the different layers within the TES structure, including insulations, are seen.

6.1.1 Heatcrete®

Heatcrete® is a unique recipe of concrete developed by EnergyNest and Heidelberg Cement. The two companies have be working on the recipe since early 2012, and their desire have been to develop a material, which has *"superior thermal properties, chemical stability and strength to withstand repeated thermal cycles at high temperatures"* [EnergyNest, 2017].

The Heatcrete® material is developed with a significantly higher thermal conductivity compared to regular concrete, which increases the dynamics of the system and implies chemically stability at high temperatures along with very effective heat transfer [Hoivik et al., 2016]. Furthermore, the heat capacity of Heatcrete® is very high, which makes it possible to reduce the volume of the storage [EnergyNest, 2017]. The improved thermal conductivity and heat capacity is seen in Figure 6.4.

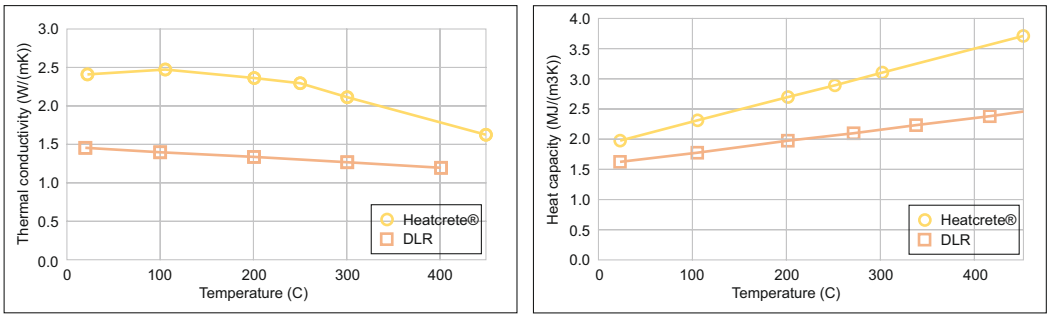

Figure 6.4. Thermal properties for Heatcrete® and DLR-concrete, inspired by [Hoivik, 2016].

The properties of Heatcrete® have been tested and verified by other laboratories[1] with the competences and equipment to do so. They have tested the following properties: heat capacity, thermal conductivity and coefficient of thermal expansion along with compressive and tensile strength, as

[1] SP Technical Research Institute of Sweden, the Norwegian University of Science and Technology, and Masdar Institute in Abu Dhabi [EnergyNest, 2017].

mentioned in Chapter 4. [Martins et al., 2015] also compare Heatcrete® with other types of concrete in different tests. The results showed that Heatcrete® is thermally and mechanically superior. Based on Figure 6.4, expressions for the specific heat capacity, c_p, and the thermal conductivity, k, are found:

$$c_{p,\mathrm{DLR}} = 694.13 + 0.8691 \cdot T \quad (\mathrm{J\,kg^{-1}\,K^{-1}}) \quad (6.1) \qquad k_{\mathrm{DLR}} = 1.446 - 0.0008 \cdot T \quad (\mathrm{W\,m^{-1}\,K^{-1}}) \quad (6.2)$$

$$c_{p,\mathrm{HC}} = 820.42 + 1.9238 \cdot T \quad (\mathrm{J\,kg^{-1}\,K^{-1}}) \quad (6.3) \qquad k_{\mathrm{HC}} = 2.5259 - 0.0017 \cdot T \quad (\mathrm{W\,m^{-1}\,K^{-1}}) \quad (6.4)$$

where DLR corresponds to the expressions given in [Laing et al., 2012], and HC are the expressions found for Heatcrete®. $T = \frac{T_c + T_w}{2}$ is an average temperature given in °C. The expressions are found by curve fitting the data in Figure 6.4.

In this project, the above TES design is the basis for the TES system modelling, however with some simplifications which are presented and explained below.

6.2 The Simplified TES System Design Modelled

The TES system seen in Figure 6.1 page 21 illustrates the TES system developed by Aalborg CSP and EnergyNest. As mentioned above, the system modelled is however simplified. The simplification is shown in the figures 6.5 and 6.6 below. The size of the modules shown are 2 x 2 x 12 meter.

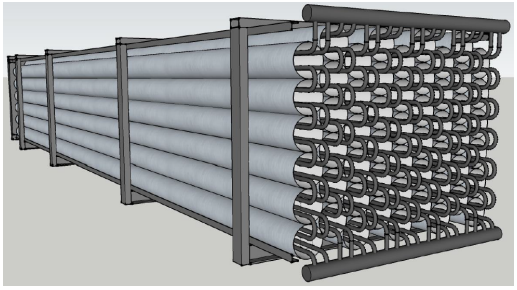

Figure 6.5. The Aalborg CSP/EnergyNest TES system with 56 concrete elements.

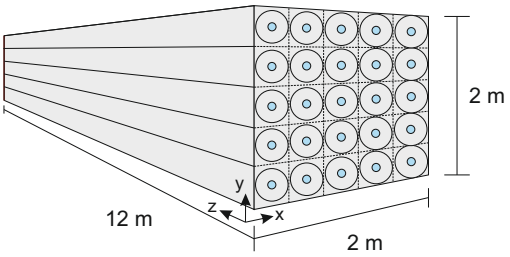

Figure 6.6. Simplified TES system with 25 concrete elements.

In Figure 6.5 the Aalborg CSP/EnergyNest TES system is shown with 56 concrete elements placed shifted, which each have four pipes as seen in Figure 6.2. In Figure 6.6 the simplified TES system is shown with 5 x 5 = 25 concrete elements. Additionally, it is seen that the four pipes in each concrete element are replaced with one pipe. This is further illustrated in Figure 6.7.

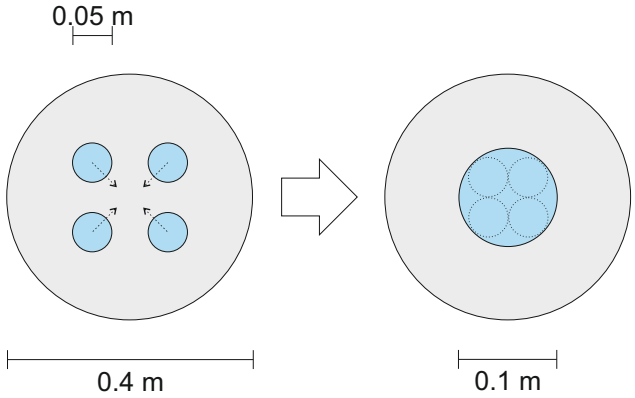

Figure 6.7. The TES system pipe simplification.

Figure 6.7 shows how the four water pipes in each concrete element are merged into one single water pipe, placed in the center. The merging makes the total pipe volume the same in both concrete elements shown. The simplified TES system is the system considered henceforth in the report.

6.3 The Discharge Mode of the TES System

In this section the three different processes occurring in the discharge of the TES system are presented. The three components in which the processes occur are:

- Economiser (ECO)
- Evaporator (EVA)
- Superheater (SH)

During discharge, the HTF first enters the economiser, then the evaporator and finally the superheater, as shown in Figure 6.8. The blue valves are open, the red valves are closed, and the white valves are additional valve suggestions. The HTF runs through the blue/black pipe strings in the directions of the light blue arrows.

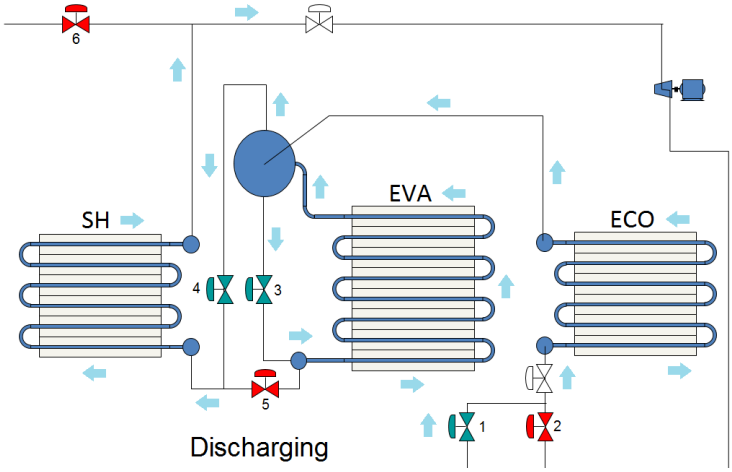

Figure 6.8. Simplified overview of the processes occurring during discharge.

As seen in the figure, the entire process in the TES is divided into the three parts explained above. The discharge process is further explained in the following:

- Economiser
  - Water enters the TES system from the feed water supply (not shown) through valve 1.
  - The water enters the economiser at approximately 105°C.
  - In the economiser the temperature increases, as the water is heated by the Heatcrete® (seen in grey) surrounding it, thus discharging the TES. The temperature increases to approximately 10 degrees below the saturation temperature (further explained below).
- Evaporator
  - With increased temperature, the water enters the steam drum, where it mixes with the existing water [Teir and Kulla, 2002].
  - From the steam drum the water is led through the evaporator (seen in grey), through valve 3. In here the temperature remains constant, while the water is heated to saturated steam, while rising to the evaporator top.
  - The HTF enters the steam drum once more, where remaining water droplets and steam are separated. The remaining water runs through valve 3 once more, while the saturated steam continues through valve 4.

- Superheater
  - The saturated steam enters the superheater, where the temperature of the steam is increased by the Heatcrete® surrounding it, further discharging the TES. The temperature goes from being saturated to superheated.
  - After leaving the superheater, the hot steam is led to a steam turbine, which converts the energy into electricity.

From Figure 6.8 and the processes explained above, it is seen that the HTF flow is controlled by several valves in the system. The blue valves, 1, 3 and 4 leads the HTF correctly through the TES while discharging. The red valves, 2, 5 and 6, ensures that the HTF does not continue in the wrong pipe strings intended for charging. When charging, the red valves, 6, 5 and 2 are opened, while the blue valves, 4, 3 and 1 are closed.

6.4 The Processes in the Storage Components

The three processes, seen in Figure 6.8, can be considered as part of the Rankine cycle, which is shown in Figure 6.9.

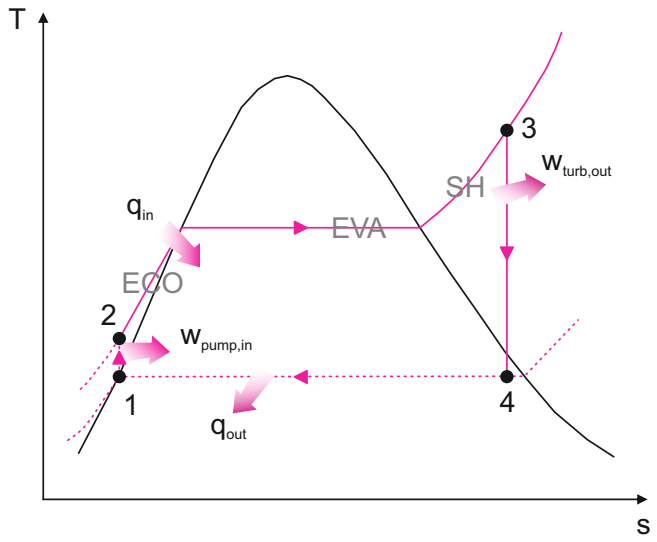

Figure 6.9. The ideal Rankine Cycle, inspired by [Cengel et al., 2012].

In Figure 6.9, the processes occurring in the TES corresponds to the process from point 2 to 3, which is the boiler section, including superheating, in the cycle. From point 2 to the saturation line, the fluid is heated through the economiser. Through the following evaporation the fluid becomes saturated vapour at constant temperature, which is seen as a constant horisontal line, and from the saturation line to point 3 the HTF is further heated in the superheater to superheated steam. The three components, including processes, are further explained in the following sections. Additionally, theory of the turbine (placed between point 3 and 4) in Figure 6.9 is briefly explained.

6.4.1 The Process in the Economiser

The purpose of the economiser is to preheat the feed water to a temperature approaching the saturation temperature, before it enters the steam drum connected to the evaporator. The temperature is typically kept 10 K below the boiling temperature in order to prevent the water from boiling in the economiser. The water flow rate in the economiser is controlled by the instruments controlling the steam drum level [Teir and Kulla, 2002] [Odesie, 2014]. The economiser is thereby used as a heat exchanger, where the HTF is preheated by the energy stored in the TES, thus using the saved energy [electrical4u.com, 2017].

6.4.2 The Process in the Evaporator

The purpose of the evaporator is to change the phase of the HTF. An evaporator typically consists of a steam drum and two types of tube modules: risers and downcomers. The purpose of the risers is to lead the heated water from the economiser through the evaporator to the steam drum, as it is heated up and converted to steam. The purpose of the downcomers is, besides to keep the water level in the steam drum, to lead the water, which is not evaporated down to the bottom of the evaporator, such that the water can be heated once more [Odesie, 2014]. The working principle of the evaporator is further explained in Appendix B.

During discharge, the water entering from the economiser is changed into saturated vapour by evaporation. The phase changes are accomplished by keeping the temperature constant. A steam drum is attached to the evaporator in order to separate the water droplets from the vapour to make sure pure steam continues in the system and also as an accumulation buffer. In the steam drum the water level is maintained by a regulator, which controls the feed water pump [IAGT, 2009].

6.4.3 The Process in the Superheater

The purpose of the superheater is to increase the steam temperature above saturation to a superheated temperature to match the following turbine. During discharge, the superheater superheats the HTF, which exits the evaporator as saturated vapour, to the maximum limit, while also eliminating the moisture content in the steam [Learn Engineering, 2016].

6.4.4 The Process in the Turbine

As seen in Figure 6.9 side 25, a turbine is placed after the superheater (point 3 to 4). In the turbine, the steam from the superheater is expanded, ideally isentropically, and work is produced by a rotating shaft connected to an electrical generator. The work produced is calculated from the following [Cengel et al., 2012]:

$$\dot{W}_{turb} = \dot{m} \cdot (H_3 - H_4) \tag{6.5}$$

where $\dot{m}$ is the mass flow rate, H_3 is the enthalpy of the steam leaving the superheater, entering the turbine, and H_4 is the enthalpy of the fluid mixture leaving the turbine. The isentropic efficiency of an adiabatic turbine is given as [Cengel et al., 2012]:

$$\eta_{turb} = \frac{H_3 - H_{4a}}{H_3 - H_{4isen}} \tag{6.6}$$

where $_a$ and $_{isen}$ are the actual and isentropic enthalpies, respectively. [Cengel et al., 2012] states that well-designed, large turbines typically have an isentropic efficiency above 90 percent.

6.5 Single- and Multiphase Flow

The HTF used in the TES system is water/steam, which means that the fluid flow changes from a single-phase flow in the economiser, to a two-phase flow in the evaporator and to a single-phase flow again in the superheater. The development of the different flow patterns in the water/steam flow in the evaporator is given in Figure 6.10. The fundamentals of multiphase flows are further elaborated in Appendix C.

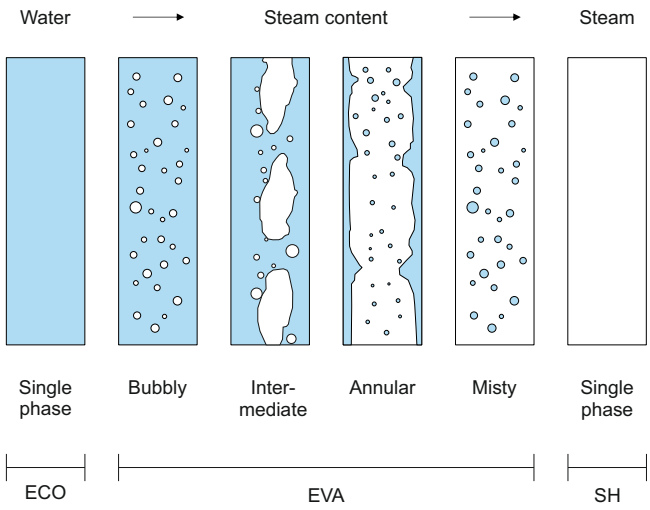

Figure 6.10. Development of the two phases in a water/steam flow, inspired by [Teir and Kulla, 2002].

From Figure 6.10 it is seen how the flow changes from being a single phase flow of water to a single phase flow of steam. In between the single phase flows, the flow is a mixture, and the flow patterns are similar to those found in Figure C.1 page 113. As the figure shows, the flow pattern just after the single phase of water, in the economiser, is a bubbly water flow in which steam bubbles have developed along the flow. The next flow pattern is an intermediate flow which resembles a plug-churn-flow combined, where steam bubbles occur in smaller and larger sizes. Afterwards, an annular flow pattern is developed in which most of the flow is steam with water droplets distributed along the flow. Finally, just before the flow becomes a single phase of steam, in the superheater, a misty flow pattern is developed, where the water wall film number of water droplets have decreased.

This chapter has presented a design description of the TES system investigated along with the processes occurring during discharge including a brief introduction to turbine theory and the multiphase flow occurring in the evaporator. In the following, the heat transfer mechanisms applied in the TES system are briefly presented.

7 Heat Transfer Mechanisms Applied in the TES

The energy in excess is stored as heat in the concrete TES system through several heat transfer mechanisms. In this chapter the heat transfer mechanisms applied in the TES system are briefly presented. The mechanisms are further elaborated in Appendix D.

7.1 The Conduction and Convection Heat Transfer Mechanisms

The thesis focuses on conduction throughout the concrete block to the pipe wall and the convection from the pipe wall to the HTF flow. This is illustrated in the figures 7.2 and 7.1.

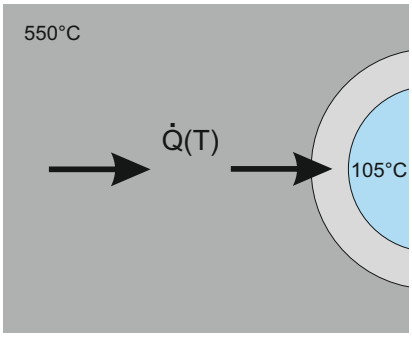

Figure 7.1. Heat transferred through conduction from the concrete to the pipe.

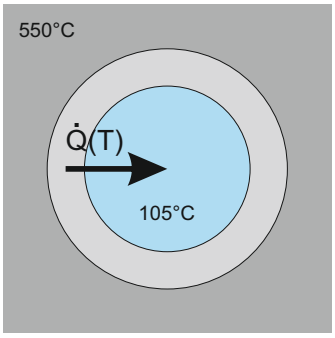

Figure 7.2. Heat transferred through convection from the pipe to the HTF.

From Figure 7.1 it is seen that the concrete is warmer than the pipe separating the fluid and concrete. This results in heat transfer from the concrete to the pipe through conduction. From Figure 7.2 it is seen that the heat, originally transferred from concrete further travels through the pipe material through conduction and reaches the HTF by convection, assuming ideal thermal contact, *i.e.* no slip between the surface of the concrete and piping is assumed [Cengel et al., 2012]. The equations explaining the above are given in Table 7.1:

Discharge mode	*Conduction*	*Conduction*	*Convection*
System location	Concrete → Concrete	Concrete → Pipe	Pipe → Fluid
Equation	$\dot{Q}_{cond} = k \cdot A_s \cdot \frac{dT}{dx}$	$\dot{Q}_{cond} = k \cdot A_s \cdot \frac{dT}{dx}$	$\dot{Q}_{conv} = h \cdot A_s \cdot (T_s - T_\infty)$

Table 7.1. Applied heat transfer mechanisms during discharge.

where k is the thermal conductivity, A_s is the surface area, dT/dx is the temperature gradient, h is the heat transfer coefficient, T_s is the surface temperature and T_∞ is the temperature sufficiently far from the surface [Cengel et al., 2012].

7.1.1 Determination of the Overall Heat Transfer Coefficient

The rate of heat transfer between the concrete and the HTF is calculated from:

$$\dot{Q} = U \cdot A_s \cdot \Delta T_m \tag{7.1}$$

where U is the overall heat transfer coefficient and ΔT_m is the mean temperature difference between the concrete and the HTF[1]. The overall heat transfer coefficient is composed of [Cengel et al., 2012]:

$$\frac{1}{U \cdot A_s} = R_{conv} + R_{wall} + R_{cond} \tag{7.2}$$

$$\Rightarrow \frac{1}{U \cdot A_s} = \frac{1}{h_i \cdot A_i} + \frac{\xi}{k \cdot A_{wall}} + \frac{1}{h_o \cdot A_o} \Rightarrow \frac{1}{U} \approx \frac{1}{h_i} + \frac{\xi}{k} + \frac{1}{h_o} \tag{7.3}$$

where R_{conv} is the convection resistance, R_{wall} is the thermal resistance through the pipe wall, R_{cond} is the conduction resistance, h_i is the inner heat transfer coefficient, h_o is the outer heat transfer coefficient and ξ is the thickness. The resistances are illustrated in Figure 7.3.

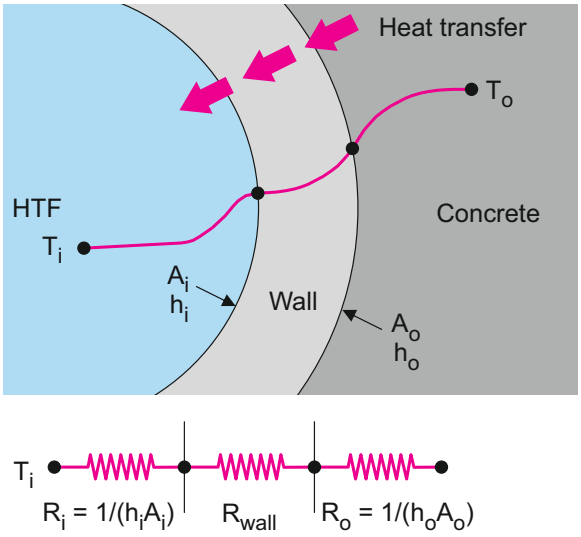

Figure 7.3. Heat transferred from the concrete to the HTF through the pipe, inspired from [Cengel et al., 2012].

From the figure it is seen how heat is transferred through the concrete and pipe walls and how the temperature changes from the concrete block to the HTF.

The thickness of the pipe wall can be calculated as [Engineers Edge, 2017]:

$$\xi = \frac{P \cdot r}{\sigma} \tag{7.4}$$

where σ is the stress in the pipe, r is the mean radius, and P is the internal pressure. Equation (7.4) is also known as the Kessel-equation. For the equation to be valid, the pipe must have a wall thickness of no more that a tenth of its radius [Engineers Edge, 2017].

7.1.2 Variable Heat Transfer Coefficient

The value of the heat transfer coefficient, h_i, varies according to the phases in the processes. [Condra, 2017] suggests, that when in single phase, *i.e.* in the economiser and superheater, the Gnielinski-correlation can be used to determine h_i [VDI Heat Atlas, 2010]:

$$\mathrm{Nu}_{mean} = \frac{(\zeta/8) \cdot \mathrm{Re} \cdot \mathrm{Pr}}{1 + 12.7 \cdot \sqrt{\zeta/8} \cdot (\mathrm{Pr}^{(2/3)} - 1)} \left[1 + (D_c/L)^{(2/3)}\right] \tag{7.5}$$

[1] ΔT_m can be determined from the logarithmic mean temperature difference, ΔT_{LMTD}, or arithmetic mean temperature difference, ΔT_{am} [Cengel et al., 2012].

$$\text{with} \quad \zeta = (1.8 \cdot \log_{10} \cdot \text{Re} - 1.5)^{(-2)} \tag{7.6}$$

$$\Rightarrow h_i = \frac{\text{Nu}_{mean} \cdot k}{D_c} \tag{7.7}$$

where ζ is a dimensionless factor related to the friction in the pipe. Equation (7.5) is valid for fully developed turbulent pipe flow of gases and liquids within the ranges $10^4 \leq \text{Re} \leq 10^6$, $0.1 \leq \text{Pr} \leq 1000$ and $D_c/L \leq 1$. When in the two-phase region, *i.e.* in the evaporator, [Condra, 2017] suggests the Mostinski-correlation in [Collier, 1981]:

$$h_{\text{boil}} = A^* \cdot \dot{q}^{0.7} \cdot F \tag{7.8}$$

$$\text{with} \quad A^* = 0.1011 \cdot P_c^{0.69} \tag{7.9}$$

$$\text{and} \quad F = 1.8 \cdot P_r^{0.17} + 4 \cdot P_r^{1.2} + 10 \cdot P_r^{10} \tag{7.10}$$

where A^* and F are dimensionless factors, $\dot{q}$ is the heat flux, P_c is the critical pressure for the fluid, and $P_r = P/P_c$ is the reduced pressure relating the system pressure and the critical pressure. [Collier, 1981] recommends this correlation for nucleate boiling.

7.2 Transient Heat Conduction: Lumped System Analysis

During transient heat transfer, implying a variation with time, the temperature normally varies with both time and position. If the temperature, however, changes uniformly with the time and thereby does not change with position, as $T(t)$, the system is termed a lumped system. Whether a lumped system analysis approach is applicable is determined from the Biot number given as [Cengel et al., 2012]:

$$\text{Bi} = \frac{\text{Convection at the surface of the body}}{\text{Conduction within the body}} = \frac{h \cdot L_c}{k} \tag{7.11}$$

where h is the convection heat transfer coefficient between the solid and the HTF, and L_c is the characteristic length defined as the concrete diameter (subtracted the pipe diameter) [Xu et al., 2012]. Generally, the lumped system analysis is applicable if [Cengel et al., 2012]:

$$\text{Bi} \leq 0.1 \tag{7.12}$$

If the above is satisfied, the temperature difference between the body and its surroundings remain within 5 percent of the surface temperature throughout the body, which is generally acceptable. The parameters and mechanisms involved in a lumped system analysis in given in Figure 7.4 [Cengel et al., 2012].

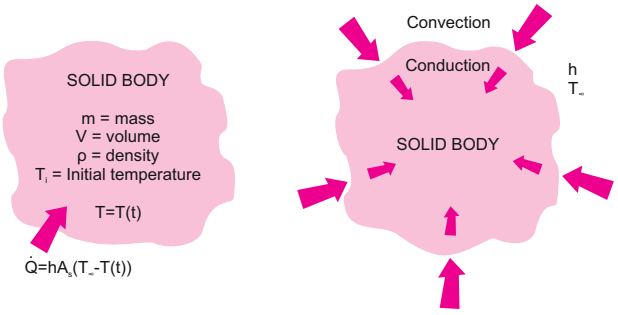

Figure 7.4. Parameters and mechanisms involved in lumped system analysis, inspired by [Cengel et al., 2012].

In Figure 7.4 convection from the surroundings into the body along with conduction within the body are illustrated. Furthermore, the body parameters necessary for the analysis is listed.

This chapter has briefly presented the heat transfer mechanisms occurring during discharge of the TES system. Furthermore, the overall heat transfer coefficient, U and the heat transfer coefficient, h_i, for the three processes in the TES system have been explained. Finally, the lumped system approach has been briefly introduced. The theory presented in this chapter is used in the Lumped-Mass-Model presented in Chapter 10. In the following chapter, the finite volume method is presented.

8 Finite Volume Method (FVM) Theory

This chapter presents the theory used in order to develop the FVM-Model presented in chapter 11. The chapter deals with the finite volume method (FVM) in 2D along with the time-dependent finite volume. General 1D FVM-theory is elaborated in Appendix E and can be applied in 2D as well, with modification, as presented in this chapter.

8.1 The Finite Volume Method in 2D

The nodal point investigated is typically termed P, while its x-directional neighbours are termed W (western neighbour) and E (eastern neighbour), and its y-direction neighbours are termed N (northern neighbour) and S (southern neighbour). The nodal point P and its neighbouring points and faces are seen in Figure 8.1.

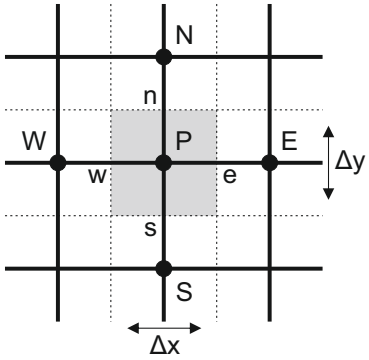

Figure 8.1. Grid generation in 2D, inspired by [Versteeg and Malalasekera, 2007].

From Figure 8.1 it is seen how the nodal point and its neighbours are placed in the 2D grid. In the following the time-dependent finite volume is presented.

8.2 The Time-Dependent Finite Volume

For the state variable φ, the conservation law for transport in an unsteady flow is given as:

$$\rho\frac{\partial\varphi}{\partial t} + \mathrm{div}(\rho\vec{u}\varphi) = \mathrm{div}(\Gamma\ \mathrm{grad}(\varphi)) + S_\varphi \tag{8.1}$$

The four terms, from left to right, are in general known as *the rate of change term*, expressing the rate of increase of φ in the element over time, *the convective term*, expressing the net rate of flow of φ out of the element, *the diffusive term*, expressing the rate of increase of φ due to diffusion, and *the source term* expressing the rate of increase of φ due to sources. "div" is the divergence, and "grad" is the gradient.

The leftmost term, $\rho\partial\varphi/\partial t$, is zero for steady flows but must be included in transient problems, as the one investigated in this project. The equation given in (8.1) must thereby be integrated over both the control volume, dV, and a finite time step, dt.

8.2.1 1D Unsteady Heat Conduction

The approach used to solve the time integration in the problem above is an approach addressing the 1D unsteady heat conduction presented in [Versteeg and Malalasekera, 2007] with $\varphi = T$:

$$\rho c_p \frac{\partial T}{\partial t} = \frac{\partial}{\partial x}\left(k\frac{\partial T}{\partial x}\right) + S \tag{8.2}$$

where c_p is the specific heat capacity of the material, and S is the source term. When integrating equation (8.2), following Figure E.2 page 119, the following is obtained:

$$\int_t^{t+\Delta t}\int_{CV} \rho c_p \frac{\partial T}{\partial t} dV dt = \int_t^{t+\Delta t}\int_{CV} \frac{\partial}{\partial x}\left(k\frac{\partial T}{\partial x}\right) dV dt + \int_t^{t+\Delta t}\int_{CV} S dV dt \tag{8.3}$$

$$\Downarrow$$

$$\int_w^e \left(\int_t^{t+\Delta t} \rho c_p \frac{\partial T}{\partial t} dt\right) dV = \int_t^{t+\Delta t} \left(\left(kA\frac{\partial T}{\partial x}\right)_e - \left(kA\frac{\partial T}{\partial x}\right)_w\right) dt + \int_t^{t+\Delta t} \overline{S}\Delta V dt \tag{8.4}$$

$$\Downarrow$$

$$\rho c_p (T_P - T_P^0)\Delta V = \int_t^{t+\Delta t} \left(\left(k_e A\frac{(T_E - T_P)}{\delta x_{PE}}\right) - \left(k_w A\frac{(T_P - T_W)}{\delta x_{WP}}\right)\right) dt + \int_t^{t+\Delta t} \overline{S}\Delta V dt \tag{8.5}$$

where the superscript ^{0} refers to the temperatures at the previous time, t. In order to evaluate the right hand side of equation (8.5), a weighting parameter θ between 0 and 1 is introduced [Versteeg and Malalasekera, 2007]:

$$I_T = \int_t^{t+\Delta t} T_P \, dt = [\theta \cdot T_P + (1-\theta)\cdot T_P^0]\cdot \Delta t \tag{8.6}$$

where

$$\theta = 0 \Rightarrow I_T = T_P^0 \Delta t \tag{8.7}$$

$$\theta = \frac{1}{2} \Rightarrow I_T = \frac{1}{2}(T_P + T_P^0)\Delta t \tag{8.8}$$

$$\theta = 1 \Rightarrow I_T = T_P \Delta t \tag{8.9}$$

This means, that if $\theta = 0$, only the temperature at the previous time, t, is used, if $\theta = \frac{1}{2}$, the temperatures at both the previous and next times, t and $t + \Delta t$, are used equally weighted, and if $\theta = 1$, only the temperature at the next time, $t + \Delta t$ is used. The values of θ are further explained in Appendix E section E.2.

Using equation (8.6) for T_E and T_W in equation (8.5), and dividing by $A\Delta t$, the following is obtained:

$$\rho c_p \left(\frac{T_P - T_P^0}{\Delta t}\right)\Delta x = \theta\left[\frac{k_e(T_E - T_P)}{\delta x_{PE}} - \frac{k_w(T_P - T_W}{\delta x_{WP}}\right] + (1-\theta)\left[\frac{k_e(T_E^0 - T_P^0)}{\delta x_{PE}} - \frac{k_w(T_P^0 - T_W^0}{\delta x_{WP}}\right] \tag{8.10}$$

$$\Rightarrow \left[\rho c_p \frac{\Delta x}{\Delta t} + \theta\left(\frac{k_e}{\delta x_{PE}} + \frac{k_w}{\delta x_{WP}}\right)\right] T_P = \frac{k_e}{\delta x_{PE}}[\theta T_E + (1-\theta)T_E^0] + \frac{k_w}{\delta x_{WP}}[\theta T_W + (1-\theta)T_W^0]$$
$$+ \left[\rho c_p \frac{\Delta x}{\Delta t} - (1-\theta)\frac{k_e}{\delta x_{PE}} + (1-\theta)\frac{k_w}{\delta x_{WP}}\right] T_P^0 + \overline{S}\Delta x \tag{8.11}$$

Identifying the coefficients a_W and a_E, equation (8.11) can be written as:

$$a_P T_P = a_W[\theta T_W + (1-\theta)T_W^0] + a_E[\theta T_E + (1-\theta)T_E^0] + [a_P^0 - (1-\theta)a_W - (1-\theta)a_E]T_P^0 + b \tag{8.12}$$

with

$$a_P = \theta(a_W + a_E) + a_P^0 \quad (8.13) \qquad b = \overline{S}\Delta x \quad (8.14)$$

and

$$a_W = \frac{k_w}{\delta x_{WP}} \quad (8.15) \qquad a_E = \frac{k_e}{\delta x_{PE}} \quad (8.16) \qquad a_P^0 = \rho c \frac{\Delta x}{\Delta t} \quad (8.17)$$

This chapter has presented the fundamentals of the FVM in 2D including time-dependence and 1D unsteady heat conduction. In Appendix E the problem is extended to 2D, where the final equations used in the FVM-Model is given. In the following chapter an efficiency analogy is presented.

9 Efficiency Analogy

In this chapter an efficiency analogy for coupling the two models developed in Part III. The analogy is drawn from the fin efficiency approach and explained in the following.

A Lumped-Mass-Model, modelling the temperature progression in the simplified TES system in the y, z-plane, is presented in Chapter 10. A FVM-Model, modelling the temperature gradient throughout the concrete block in the x, y-plane, is presented in Chapter 11. The temperature gradient in the concrete block can be accounted for by an approach analogically to the approach used for fin efficiencies. A fin analogy is seen in Figure 9.1.

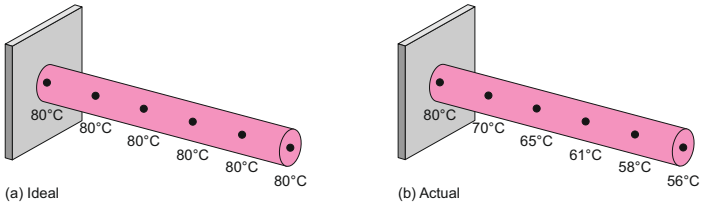

Figure 9.1. Temperature distribution in an ideal (a) and actual (b) fin [Cengel et al., 2012].

From the figure it is seen, that in the ideal case (a) the temperature throughout the fin is constant - as in the lumped mass modelled in the Lumped-Mass-Model. However, in the actual case (b) the temperature varies, as in the FVM-model. This is further illustrated in Figure 9.2.

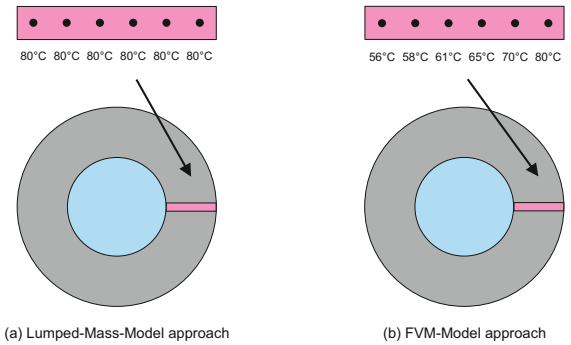

Figure 9.2. Temperature distribution in the concrete, analogue to the fin efficiency theory.

In Figure 9.2, the temperature distribution from the fin analogy in Figure 9.1 is transferred to the simplified TES system. The wall seen to the left in Figure 9.1 corresponds to the pipe wall in Figure 9.2. From the figure it is seen how the temperature distribution is modelled in the Lumped-Mass-model (a) and the FVM-model (b). It should be noticed that the temperature values shown in Figure 9.2 are only for comparison with Figure 9.1 and are not the actual temperatures found in the two models.

In the fin analogy, the fin efficiency is accounted for as following [Cengel et al., 2012]:

$$\dot{Q}_{fin} = \eta_{fin} \cdot \dot{Q}_{fin,max} = \eta_{fin} \cdot h \cdot A_{fin} \cdot (T_b - T_\infty) \tag{9.1}$$

$$\Rightarrow \dot{Q}_{actual} = \eta_{\text{storage}} \cdot \dot{Q}_{lumped} \tag{9.2}$$

where $\dot{Q}_{fin}$ is the actual heat transfer rate from the fin, η_{fin} is the fin efficiency, $\dot{Q}_{fin,max}$ is the ideal heat transfer rate from the fin, A_{fin} is the surface area of the fin, T_b is the base temperature (at the wall), T_∞ is the surrounding temperature, $\dot{Q}_{actual}$ is the actual heat transfer rate (including temperature gradient), η_{storage} is the storage efficiency related to the temperature gradient and $\dot{Q}_{lumped}$ is the heat transfer rate from the lumped mass TES system.

This chapter has presented an efficiency analogy, which is used in Chapter 13, where the Lumped-Mass-Model and the FVM-Model are coupled. In the following chapters the set-up of two developed models are given.

Part III

Modelling Approaches

10 Model 1: Lumped-Mass-Model

This chapter presents the approach and equations used for modelling the simplified TES system presented in section 6.2 page 23. The model is based on a system consisting of a lumped concrete mass with one cylindrical pipe, placed in the center of the block, with water/steam flowing through as the HTF. In the following, this model is termed the Lumped-Mass-Model.

10.1 Purpose of the Lumped-Mass-Model

The Lumped-Mass-Model is set up in order to calculate and understand the temperature change and heat transfer in the TES system during discharge. The output of the Lumped-Mass-Model is the temperatures of the HTF and concrete as functions of time and element, the system pressure and the turbine work produced over time.

10.2 Lumped-Mass-Model Assumptions

For the Lumped-Mass-Model the following assumptions are made:

1. The concrete block in the TES-system can be treated as a lumped mass with a uniform temperature.
2. The pipe in the TES-system is divided into n elements, which are small enough for the changes through each element to be neglected.
3. The piping can be gathered as one centrally placed pipe with the same volume as the four individual pipes in total.
4. Initially, the pipe is filled with water at 105°C (378.15 K).
5. The overall system pressure is constant in each process, *i.e.* no pressure losses in the components are accounted for, but the overall system pressure changes with time.
6. The mass flow rate of the HTF in the pipe is constant.
7. The inlet water and concrete densities are constant.
8. The TES system is completely isolated. No energy losses to the surroundings are accounted for in the model.

10.3 Lumped Concrete Block Approach

The modelled TES system is illustrated in the figures 10.1 and 10.2. The TES system is modelled in 2D in the y, z-plane.

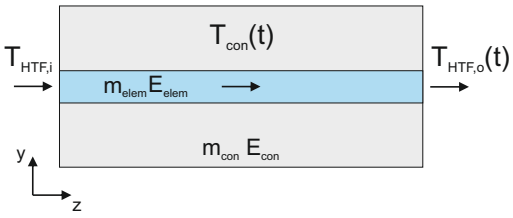

Figure 10.1. Simple lumped TES system with a concrete block and one pipe.

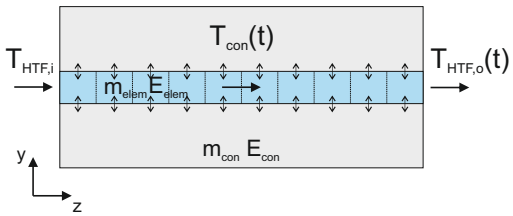

Figure 10.2. Simple lumped TES system divided into elements.

Figure 10.1 shows how the cylindrical pipe is located inside the lumped concrete block. In the figure, three temperatures are visible: the HTF inlet temperature, $T_{HTF,i}$, the HTF outlet temperature,

$T_{HTF,o}$ and the concrete temperature T_c. The latter two are functions of time, as they change, when the HTF flows through the pipe.

Figure 10.2 shows the pipe divided into elements, in this case 10 elements. As mentioned above, the concrete block is modelled as a lumped mass, which is why only the pipe is divided into elements. It is assumed that the pipe is divided into small enough elements, thereby making the temperature difference across the element small enough to model the temperature in each element as one temperature and not an inlet and outlet temperature.

With the above approach the model is set up based on the following steps:

1 System initialisation: Determination of primary variables, m_{elem}, E_{elem}, m_{con} and E_{con}.
2 Determination of secondary variables T_{elem}, h_{ECO}, h_{EVA}, h_{SH}, T_{con} and pressure, P.
3 Definition of the differential equations for m_{elem}, E_{elem}, m_{con} and E_{con}.
4 Solution of the differential equations and calculation of next time step $(t + \Delta t)$.
5 Check of energy balance.

In the following the steps are further elaborated.

10.3.1 Step 1: System Initialisation

In Step 1 the system is fully determined at the initial time, $t = 0$. The pipe, concrete and fluid properties are initialised, and the primary variables - mass (m_{elem}, m_{con}) and energy (E_{elem}, E_{con}) - are determined. This is done for each element in the system, which in Figure 10.2 corresponds to 10 HTF elements and one concrete element. The degrees of freedom (DOF) of the system are thereby 22[1]. This, however, is not true for the actual model, since the number of elements here is larger than 10. This is further elaborated in section 10.5. The primary variables are initially determined from:

$$m_{elem} = V_{elem} \cdot \rho_{wat} \tag{10.1}$$

$$E_{elem} = m_{elem} \cdot H_{elem} \tag{10.2}$$

$$m_{con} = V_{conc} \cdot \rho_{con} \tag{10.3}$$

$$E_{con} = m_{con} \cdot c_{p,con} \cdot T_{con} \tag{10.4}$$

where m_{elem} is identical for each element, since the volume, V_{elem}, and the density, ρ_{wat}, of each element is identical. Thereby also E_{elem} is identical for each element. This is valid for the initialisation, since each element is filled with the same amount of water at the same temperature. The above applies for concrete as well, seen as only one concrete element.

10.3.2 Step 2: Determination of the Secondary Variables

In Step 2 the secondary variables of the system the temperatures, T_{elem} and T_{con}, the heat transfer coefficients, h_{ECO}, h_{EVA} and h_{SH} along with the overall heat transfer coefficient, U, are determined by:

$$T_{elem} = refprop(P, H_{elem}) \tag{10.5}$$

$$T_{con} = \frac{E_{con}}{m_{con} \cdot c_{p,con}} \tag{10.6}$$

$$h_{ECO} = h_{SH} = \frac{Nu \cdot k}{D_{pipe}} \tag{10.7}$$

$$h_{EVA} = 10\,000\,\mathrm{W\,m^{-2}\,K^{-1}} \tag{10.8}$$

$$\frac{1}{U} = \frac{1}{h_i} + \frac{1}{\frac{k}{x}} \Rightarrow U = \frac{k \cdot h_i}{h_i \cdot x + k} \tag{10.9}$$

where equation (10.5) is a *refprop* function of the pressure, P, and the enthalpy, H_{elem}. The heat transfer coefficients in the economiser and superheater processes are calculated from equation (10.7), where the Nusselt number is calculated by the Gnielinski equations (7.5) and (7.6) page 30.

[1] DOF = Number of elements x Number of independent variables → DOF = 11 x 2 = 22.

Equation 7.5 is not valid for the evaporation process. In order to avoid an iterative process using Mostinski's equation (7.8) page 31, since the heat flux $\dot{q}$ depends on the overall heat transfer coefficient, U, a value of $h_{EVA} = 10\,000\,\mathrm{W\,m^{-2}\,K^{-1}}$ is chosen for the evaporation process [Condra, 2017]. When comparing equation (10.9) to equation (7.3) page 30, the outer heat transfer coefficient, h_o, is found to be is neglected, since the contribution from the outer heat transfer is insignificant compared to the other two contributions[2].

Additionally, the pressure of the system is determined as a function of the concrete temperature and the pinch temperature, ΔT_{pinch}:

$$P = refprop(T_c - \Delta T_{pinch}, x) \tag{10.10}$$

where x is the quality (notice: Q in *refprop* notation). The pinch temperature is basically a temperature difference between the concrete temperature and the HTF temperature, and not the typical definition of a pinch temperature. The pinch temperature is evaluated right before the HTF enters the evaporator, *i.e.* at $x = 0$. This is seen in Figure 10.3 at time t.

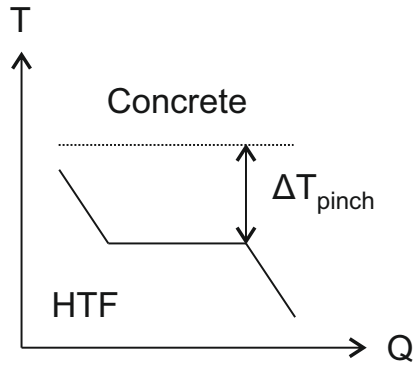

Figure 10.3. Illustration of ΔT_{pinch} evaluation between the concrete and HTF temperatures.

In order for the pressure to be evaluated by *refprop*, an upper pressure limit is implemented, since the temperature difference, $T_c - \Delta T_{pinch}$, starts out relatively large (initially at 803.15 K). The pressure limit used, stated by Aalborg CSP, is 100 bar [Jensen, 2017]. This means that when the temperature difference is too high, the HTF is placed above the critical temperature, and the upper pressure limit is used. Similarly, a lower pressure limit is needed based on the input requirements for the turbine placed after the storage. The lower pressure limit is chosen to be 60 bar, which corresponds to a temperature of 548.8 K. This is seen in Figure 10.4.

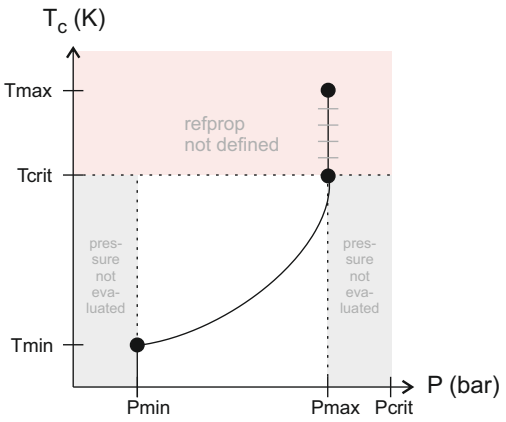

Figure 10.4. Pressure implementation in the Lumped-Mass-Model.

[2] $\frac{1}{U} \approx \frac{1}{h_i} + \frac{1}{k_{wall}/x_{wall}} + \frac{1}{k_{con}/x_{con}} \approx \frac{1}{10^4} + \frac{1}{10^4} + \frac{1}{10^1}$.

Figure 10.4 illustrates how the pressure is evaluated in *refprop*. Within the red area, *refprop* is not defined, since the look-up value is above the saturation curve, and the actual pinch temperature is much higher than defined. Within the grey areas the pressure limits are used, and also here the actual pinch temperature is different from the one defined. Within the white area the pressure is defined based on the difference between the concrete temperature and the ΔT_{pinch} defined along with the quality of the HTF.

10.3.3 Step 3: Definition of the Differential Equations

In Step 3 the differential equations for the primary variables are set up as:

$$\frac{\partial m_{elem}}{\partial t} = \dot{m}_{in} - \dot{m}_{out} = 0 \tag{10.11}$$

$$\frac{\partial E_{elem}}{\partial t} = \dot{E}_{in} - \dot{E}_{out} + \dot{Q} \tag{10.12}$$

Equation 10.11 is the differential equation for the mass change in each element but since $\dot{m}_{in} = \dot{m}_{out}$, the change is zero[3]. Equation 10.12 is the differential equation for the energy change in each element, where $\dot{E}_{in}$ is the energy entering the element, $\dot{E}_{out}$ is the energy leaving the element, and $\dot{Q}$ is the heat transfer rate from the concrete to the HTF. These are giving by:

$$\dot{E}_{in} = H(H_0 : H_9) \cdot \dot{m} \tag{10.13}$$

$$\dot{E}_{out} = H(H_1 : H_{10}) \cdot \dot{m} \tag{10.14}$$

$$\dot{Q} = U \cdot A_s \cdot (T_c - T_w) \tag{10.15}$$

The inlet and outlet energies are calculates from different enthalpies as illustrated in the figures 10.5 and 10.6.

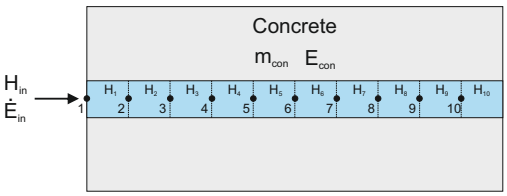

Figure 10.5. Illustration of where the inlet energy are calculated.

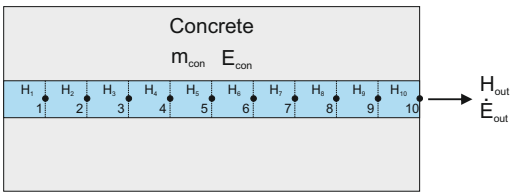

Figure 10.6. Illustration of where the outlet energy are calculated.

In the figures the inlet and outlet locations are marked with a black dot at each elements. In Figure 10.5 it is seen that the first inlet energy is calculated from the inlet enthalpy, and the last inlet energy is calculated from the outlet of H_9. In Figure 10.6 the similar is seen, however, the first outlet energy is calculated from H_1, and the last outlet energy is calculated from H_{10}. The equations for the mass and energy changes in the concrete are given by:

$$\frac{\partial m_{con}}{\partial t} = 0 \tag{10.16}$$

$$\frac{\partial E_{con}}{\partial t} = -\sum \dot{Q} \tag{10.17}$$

Equation (10.16) equals zero, since the concrete mass does not change over time. Equation (10.17) is the sum of the heat transfer rate, since the concrete block is modelled as a lumped mass, and the energy transferred to the HTF flow occurs at the same time for each element. The equation is negative, since the energy is transferred from the concrete to the HTF.

[3]Mass change over time related to HTF phase change is assessed insignificant and therefore neglected.

10.3.4 Step 4: Solution and Calculation of Next Time Step

In Step 4 the differential equation defined in Step 3, equation (10.12), is solved, and the energy in the next time step $(t + \Delta t)$ is calculated. This is done by using Euler's method, which is briefly presented in Appendix D. The energies in the next time step are calculated from:

$$E_{elem}^{t+\Delta t} = E_{elem}^{t} + \frac{\partial E_{elem}}{\partial t} \cdot \Delta t \tag{10.18}$$

$$E_{con}^{t+\Delta t} = E_{con}^{t} + \frac{\partial E_{con}}{\partial t} \cdot \Delta t \tag{10.19}$$

where equation (10.18) calculates the energy in the HTF element, and equation (10.19) calculates the energy in the concrete, both in the next time step $(t + \Delta t)$. Furthermore, the quality of the HTF element in the next time step $(t + \Delta t)$ is defined. This is done such that the three processes can be distinguished. The quality definition is made using *refprop*:

$$\text{Quality} = refprop(P, H^{t+\Delta t}) \tag{10.20}$$

where the enthalpy, $H^{t+\Delta t}$, is calculated from:

$$H^{t+\Delta t} = \frac{E_{elem}^{t+\Delta t}}{m} \tag{10.21}$$

10.3.5 Step 5: Check of Energy Balance

In Step 5 the energy balance of the system is checked:

$$E_{sys,tot} = E_{con} + \sum E_{elem} \tag{10.22}$$

$$E_{sys}(t) = E_{sys,tot,0} + \int_0^t \left(\dot{E}_{in} - \dot{E}_{out}\right)\, dt \tag{10.23}$$

$$\frac{dE_{sys}}{dt} = \dot{E}_{in} - \dot{E}_{out} \Rightarrow \frac{dE_{sys}}{dt} - (\dot{E}_{in} - \dot{E}_{out}) = 0 \tag{10.24}$$

Equation (10.24) states that the change of energy of the system over time has to be equal to the difference of the energy entering the system minus the energy leaving the system. The above presented equations are used in the Lumped-Mass-Model, and the following section gives a walk-through of the model.

10.4 MATLAB Set-Up: The Lumped-Mass-Model Walk-Through

The Lumped-Mass-Model is simulated in MATLAB by solving the presented equations for the pre-defined simulation time, t_{sim}, time step dt and number of elements, n. The input values for the Lumped-Mass-Model are presented in Table 10.1.

Input Parameter	**MATLAB Model Name**	**Value**
Number of pipe elements	n	100
Initial water temperature	Wat.T_Init	$105 + 273.15$ K
Inlet water temperature	Wat.T_Inlet	$105 + 273.15$ K
HTF mass flow rate	m_dot	$10\,\mathrm{kg\,s^{-1}}$ ($1.27\,\mathrm{m\,s^{-1}}$)
ΔT_{pinch}	DT_Pinch	10 K
Density of water	rho	$688.6\,\mathrm{kg\,m^{-3}}$
Initial pressure	P_Init	100 bar $= 10^7$Pa
Initial concrete temperature	Con.T_Init	$550 + 273.15$ K
Concrete specific heat capacity	Con.cP	$750\,\mathrm{J\,kg^{-1}\,K^{-1}}$
Mass of concrete	Con.m	115 200 kg
Length of the TES-system	L	12 m
Total surface area of pipes	A	$94.25\,\mathrm{m^2}$
Heat transfer coefficient (Economiser)	h_ECO	$9000\,\mathrm{W\,m^{-2}\,K^{-1}}$
Heat transfer coefficient (Evaporator)	h_EVA	$10\,000\,\mathrm{W\,m^{-2}\,K^{-1}}$
Heat transfer coefficient (Superheater)	h_SH	$3700\,\mathrm{W\,m^{-2}\,K^{-1}}$
Simulation time	t_sim	20 000 s (5.5 h)

Table 10.1. The Lumped-Mass-Model input values.

Figure 10.7 illustrates the HTF dynamics in the Lumped-Mass-Model.

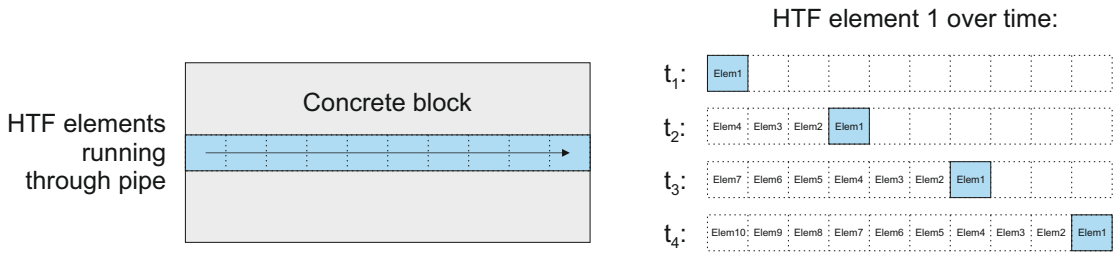

Figure 10.7. HTF element movement in the pipe over time.

To the left in Figure 10.7 the concrete block (grey) and pipe (light blue) is seen. The HTF elements enters the pipe from the left and "runs" through the pipe over time. To the right element 1 (Elem1) is seen at different times. It is seen that the element starts to the left and is pushed rightwards, over time, by the following elements, until the pipe outlet is reached.

The set-up of the Lumped-Mass-Model is given in the following flow diagram, which sums up the steps explained in section 10.3.

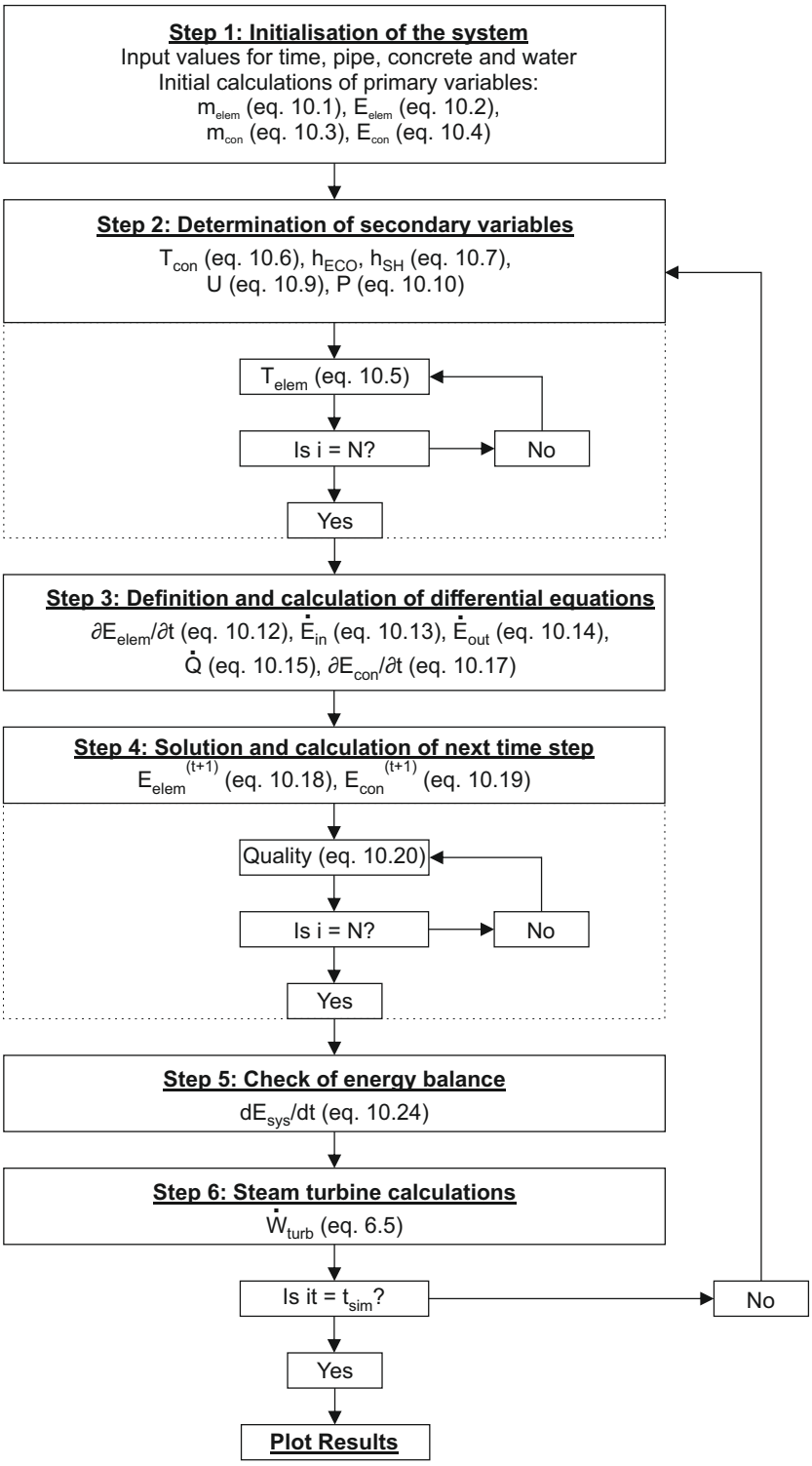

Figure 10.8. Flow diagram showing the set-up of the Lumped-Mass-Model in MATLAB.

10.5 Model Evaluation

This section presents results of a brief parametric study performed in order to understand and physically verify the model, and how selected parameters affect the results. The selected parameters are presented along with a base model for comparison and simulation results.

10.5.1 Selected Parameters

The parameters investigated in this study are presented in Table 10.2.

Input parameter	MATLAB Model Name	Range
Number of elements	n	[50; 100; 150]
HTF mass flow rate	m_dot	[5; 10; 15]
Time step	dt	[0.5; 1]
System pressure (constant)	P	[60; 100]
System pressure (func. of T_c)	P	calculated (Eq. 10.10)

Table 10.2. Parameters investigated in the Lumped-Mass-Model.

10.5.2 Base Model

In order to evaluate the influence from the selected parameters, a base model is set up. In the parameter variation, only one parameter is varied at a time, and the results are compared to the base model and to the mutual results. For the base model, the following values are chosen: n = 100, m_dot = 10 kg s^{-1}, dt = 1 s and P = 100 bar. With the parameter values presented above, the following result is obtained.

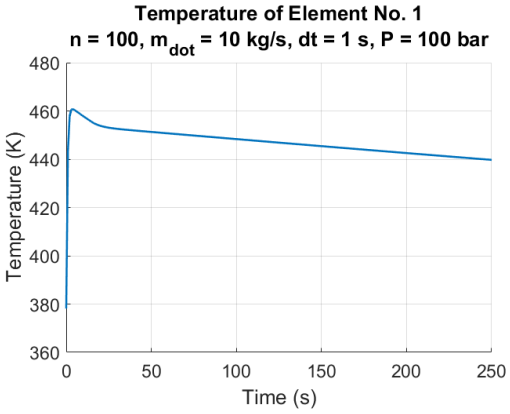

Figure 10.9. Base model result for the first HTF element after 250 s.

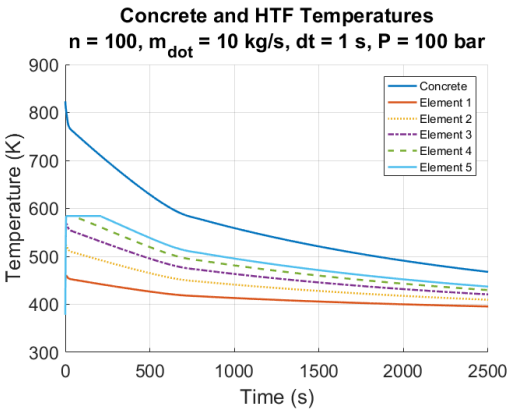

Figure 10.10. Base model result for the first five HTF elements after 2000 s.

From Figure 10.9 it is seen that the temperature of the first HTF element in the pipe first increases rapidly, thereafter decreases over time. This increase is due to the assumption that the pipe initially is filled with water at 378.15 K = 105°C, and therefore the concrete block needs to heat up the water, both existing and incoming, before the temperature decreases, as the TES system is discharged. Additionally, it is seen that the first HTF element never reaches the saturation temperature of approximately 584 K = 311°C. The HTF element is found to peak at reach 461 K = 188°C after 4 s. The saturation temperature is first reached by the fourth HTF element, as seen in Figure 10.10. In the figure the first five HTF elements are shown, where it is seen that the first three elements never reach the saturation temperature due to the assumption of the pipe initially being filled with water. This means that the first three elements have passed through the pipe before receiving enough heat from the TES system to evaporate. A plot of the last element leaving the pipe is seen in Figure 10.11. Figure 10.12 shows 10 HTF elements after 15 000 s.

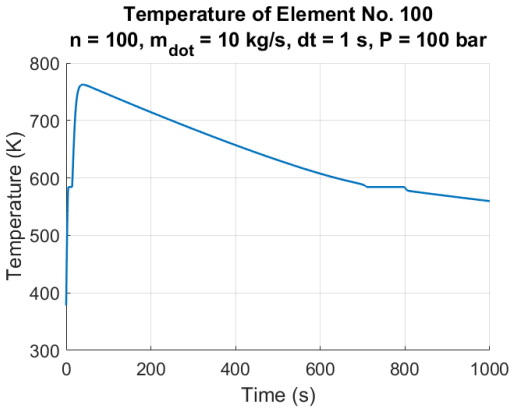

Figure 10.11. Base model result for the last HTF element after 1000 s.

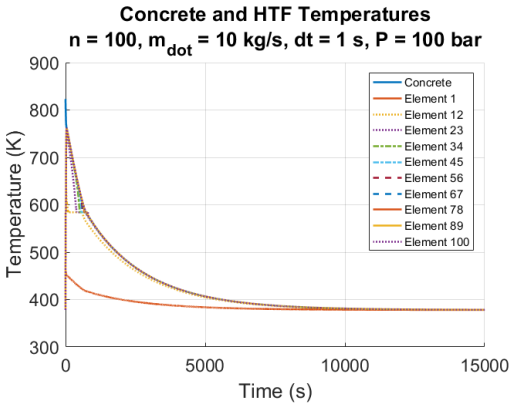

Figure 10.12. Base model result for 10 HTF elements after 15 000 s.

Figure 10.11 shows that the last HTF element reaches a relatively high temperature of approximately 762 K = 489°C after 40 s. Is is also seen that the last HTF element experiences the saturation temperature twice at different times (after 5 and 710 s, respectively). The first experience occurs due to the assumption of the pipe initially being filled with water, and the HTF has to be heated up before the TES system discharges with the HTF as steam as intended. The second experience is due to the temperature of the TES system, which has decreased during discharge resulting in the HTF being saturated before decreasing again, until the water inlet temperature of 378.15 K = 105°C is reached. After approximately 10 000 s = 2.78 h all HTF elements reach the water inlet temperature as seen in Figure 10.12. Figure 10.13 shows a 3D plot of the TES system temperature with all HTF elements and a time range of [0 ; 200] s.

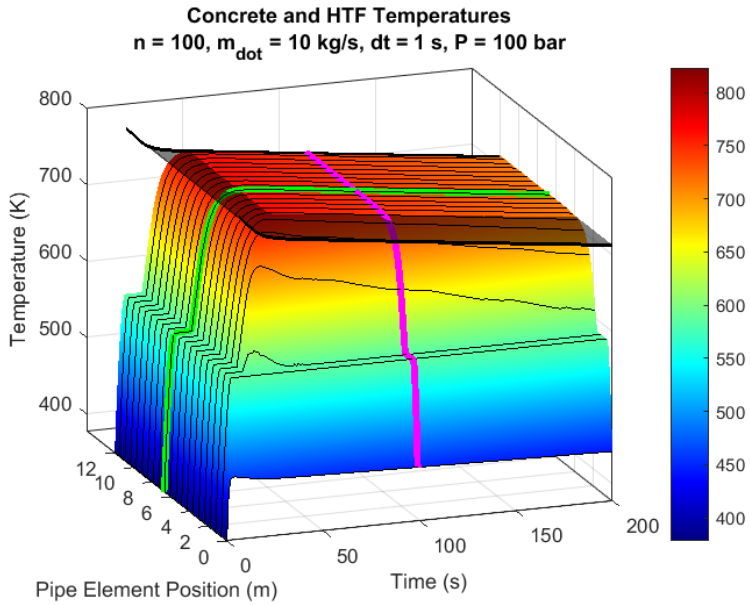

Figure 10.13. 3D plot of the concrete and HTF temperatures after 200 s.

In Figure 10.13 the x-axis is time, the y-axis is temperature and the z-axis is the element position along the pipe. The colourbar used illustrates the decreasing temperature from dark red to dark blue. The highlighted lines, in **magenta** and **green**, represents a fixed time and element position, respectively. The **magenta line** shows the temperature progression along the pipe at $t = 100$ s. The **green line** shows the temperature progression over time at element 56 corresponding to 6.7 meters inside the pipe. The black lines illustrate the temperature progression in every 5th

HTF element from 1 to 100. The concrete temperature is seen as a "dark plate" placed partly above the HTF elements. It is seen that the concrete temperature decreases rapidly in the first approximately 14 s due to the relatively high temperature difference between the concrete and HTF as a consequence of the water initially in the pipe. Additionally it is seen that sometimes the HTF temperature surpasses the concrete temperature, which is due to the simplification of the concrete mass being lumped. This means that the entire concrete block transfers heat to all HTF elements at all times. It should be noticed that Figure 10.13 only shows the first 200 s of the simulation. However, the progression corresponds to the progression seen in Figure 10.12, where all elements have reached the water inlet temperature of 378.15 K = 105°C after approximately 10 000 s = 2.78 h.

10.5.3 Results

In the following sections the results from the various simulations, given in Table 10.2, are presented in 2D and explained. The results are compared with Figure 10.14 for the base model explained in the following. It should be noticed that the x-axes in the following figures vary in order to highlight significant progressions.

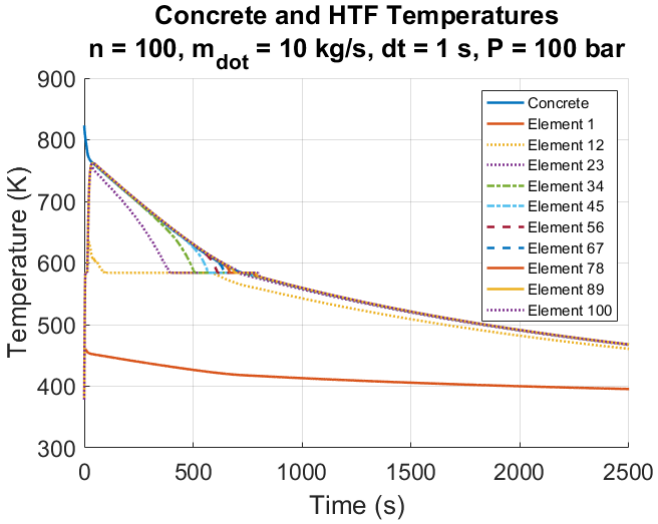

Figure 10.14. Temperature results from the base model for comparison.

Various Number of Elements

In the following, results from n = [100 ; 150] are shown. In each plot 10 HTF elements are shown.

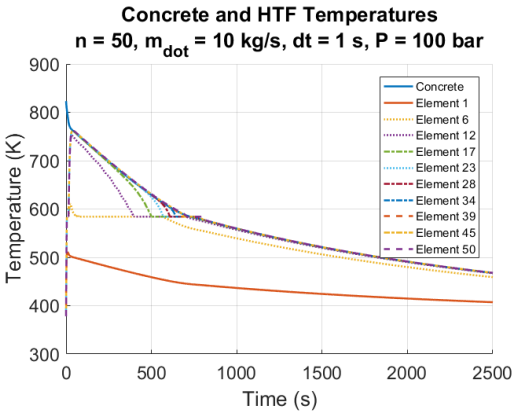

Figure 10.15. Parameter study result for the number of elements ($n = 50$).

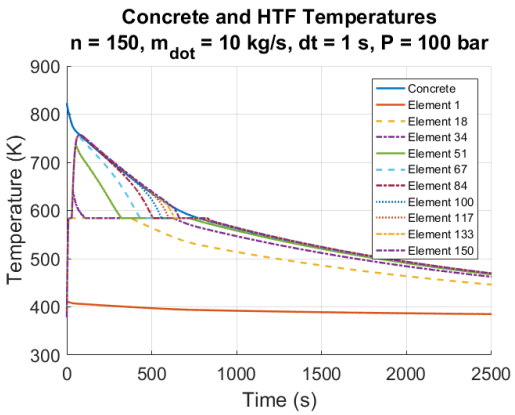

Figure 10.16. Parameter study result for the number of elements ($n = 150$).

In Figure 10.15 it is seen that, when comparing to the base model, the size of the elements have doubled, as 50 elements corresponds to elements of 24 cm each, and 100 elements (the base model) corresponds to elements of 12 cm each. This results in the elements in Figure 10.15 generally reaching a higher temperature and starts decreasing later. This is evident when looking at *e.g.* element 1 (the **red line** in both) and element 12 (the **purple line** in Figure 10.15 and the **yellow line** in Figure 10.14).

In Figure 10.16 it is seen that, when comparing to the base model, the size of the elements have decreased, as 150 elements corresponds to elements of 8 cm each. This results in the elements in Figure 10.16 generally reaching a lower temperature and starts decreasing earlier. This is evident when looking at *e.g.* element 1 (the **red line** in both) and element 34 (the **purple line** in Figure 10.16 and the **green line** in Figure 10.14).

From the above evaluation it is assessed that the number of elements is correctly implemented in the Lumped-Mass-Model, as the size of the elements affects how much the HTF temperature increases and when it decreases in each element.

Various HTF Mass Flow Rates

In the following, results from m_dot = [5 ; 15][4] are shown. In each plot 10 HTF elements are shown.

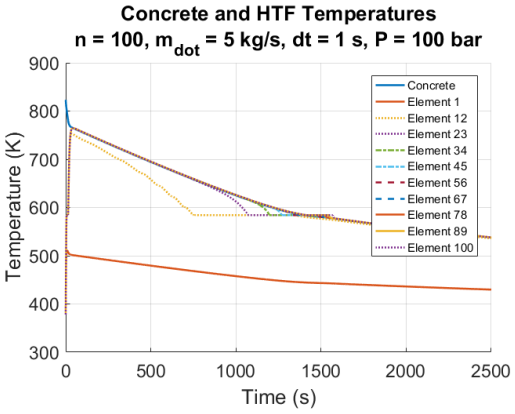

Figure 10.17. Parameter study result for the mass flow rate ($\dot{m} = 5\,\mathrm{kg\,s^{-1}}$).

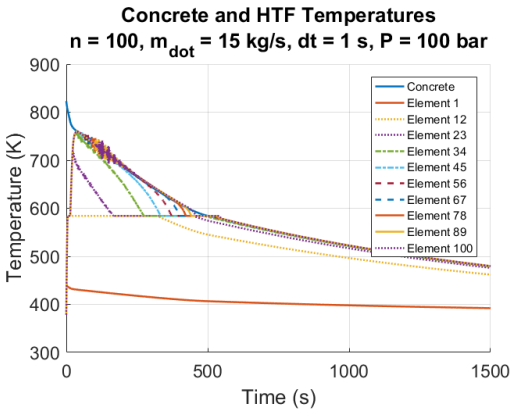

Figure 10.18. Parameter study result for the mass flow rate ($\dot{m} = 15\,\mathrm{kg\,s^{-1}}$).

In Figure 10.17 it is seen that when decreasing the mass flow rate, compared to the base model, the HTF elements experience the same progression but later in time. The HTF elements in Figure 10.17 are cooled down slower, compared to Figure 10.14, resulting in a higher outlet temperature at the end of the simulation. Generally, a higher temperature is reached for $\dot{m} = 5\,\mathrm{kg\,s^{-1}}$ (Figure 10.17), compared to $\dot{m} = 10\,\mathrm{kg\,s^{-1}}$ (Figure 10.14). This is evident when looking at *e.g.* element 1 (the **red line** in both) and element 12 (the **yellow line** in both).

In Figure 10.18 it is seen that when increasing the mass flow rate, compared to the base model, the HTF elements experience the same progression but faster in time. The HTF elements in Figure 10.18 are cooled down faster, compared to Figure 10.14, resulting in a lower outlet temperature at the end of the simulation. Generally, a lower temperature is reached for $\dot{m} = 15\,\mathrm{kg\,s^{-1}}$ (Figure 10.18), compared to $\dot{m} = 10\,\mathrm{kg\,s^{-1}}$ (Figure 10.14). This is evident when looking at *e.g.* element 1 (the **red line** in both) and element 12 (the **yellow line** in both). For the elements 23 and above fluctuating temperatures are seen. This is due to the chosen time step of dt = 1. The observed is further addressed in the following section.

[4] $5\,\mathrm{kg\,s^{-1}}$ corresponds to a fluid velocity of $0.64\,\mathrm{m\,s^{-1}}$, while $15\,\mathrm{kg\,s^{-1}}$ corresponds to a fluid velocity of $1.91\,\mathrm{m\,s^{-1}}$.

From the above evaluation it is assessed that the mass flow rate is correctly implemented in the Lumped-Mass-Model, as the mass flow rate affects how fast the HTF temperature decreases and when the TES system is completely discharged (approximately $20\,000\,\mathrm{s} = 5.56\,\mathrm{h}$ for $\dot{m} = 5\,\mathrm{kg\,s^{-1}}$, $10\,000\,\mathrm{s} = 2.78\,\mathrm{h}$ for $\dot{m} = 10\,\mathrm{kg\,s^{-1}}$ and $8000\,\mathrm{s} = 2.23\,\mathrm{h}$ for $\dot{m} = 15\,\mathrm{kg\,s^{-1}}$).

Various Time Steps

In the following, results from dt = [0.5 ; 1] are shown. In each plot 10 HTF elements are shown.

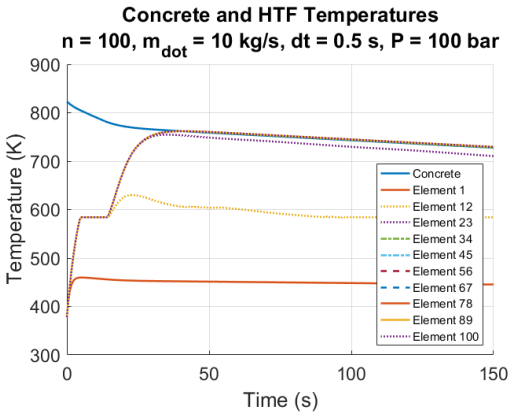

Figure 10.19. Temperature observations at time step dt = 0.5 s.

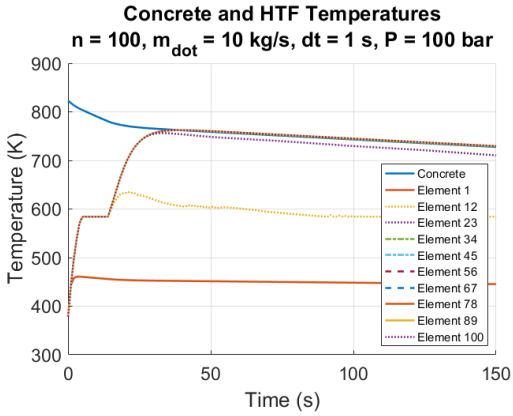

Figure 10.20. Temperature observations at time step dt = 1 s.

When observing element 12 (the **yellow line** in both figures), it is seen that for dt = 1, in Figure 10.20 small temperature ripples are seen over time. This is due to how the differential equations are solved, as explained in section 10.3.4 page 45. When decreasing the time step to dt = 0.5, as seen in Figure 10.19, the ripples are minimised.

From the above it is assessed that the time step should be sufficiently small in order for the numerical error of the solution to be acceptable. A time step of dt = 0.5 is assessed acceptable.

Various System Pressure Relations

In the following, results from the constant system pressure (P = 60 bar) and the temperature-dependent system pressure (P = f(T_c,ΔT_{pinch})) are shown. In each plot 10 HTF elements are shown.

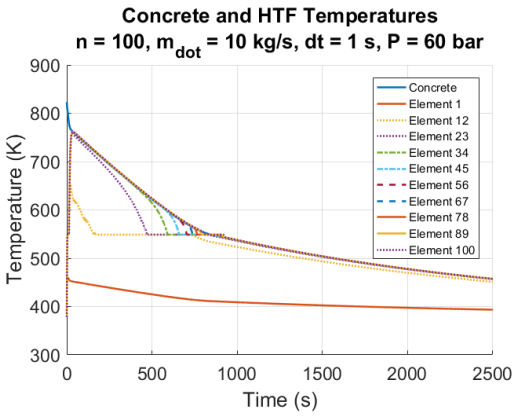

Figure 10.21. Parameter study result for the pressure ($P = 60\,\mathrm{bar}$).

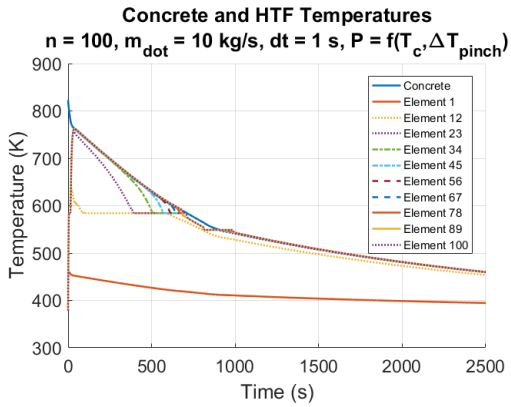

Figure 10.22. Parameter study result for the pressure ($P = f(T_c, \Delta T_{pinch})$.

In Figure 10.21 it is seen that when decreasing the constant pressure from 100 bar (the base model) to 60 bar, the saturation temperature is decreased from 584 K = 311°C to 549 K = 276°C, which corresponds to the decreased pressure. Otherwise, the temperature progressions are similar with generally lower temperatures in Figure 10.21 compared to Figure 10.14.

In Figure 10.22 it is seen that the temperature progression is affected by the varying pressure. In the time range [686 ; 814] s the pressure decreases from 100 to 60 bar, as seen in Figure 10.23 page 53. The decrease in pressure affects the saturation temperature, as seen in the same time range in Figure 10.22, which also decreases. This generally causes the HTF elements to leave the saturation state later, *i.e.* after approximately 990 s in Figure 10.22 compared to approximately 800 s in Figure 10.14.

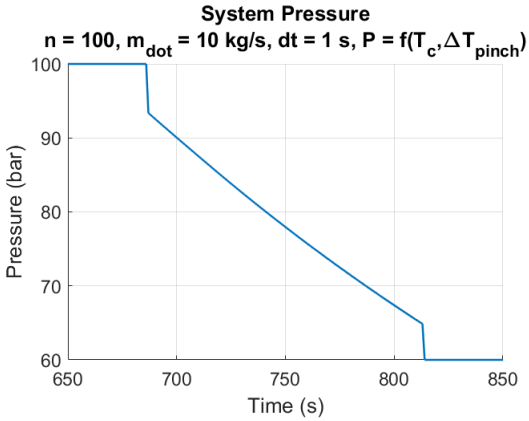

Figure 10.23. System pressure decrease in the base model.

Figure 10.23 shows how the system pressure decreases in the time range [686 ; 814] s, as explained in section 10.3.2 page 42.

From the above evaluation it is concluded that the pressure affects the HTF temperature progression around the saturation temperature based on the definition of the varying pressure. Otherwise, similar progressions are seen.

10.6 Model Validation: The Energy Balance

The Lumped-Mass-Model is validated based on the system energy balance, given in equation (10.24) page 45. The energy balance result is seen in Figure 10.24.

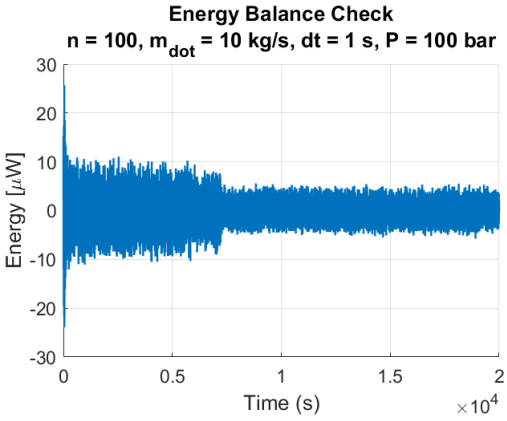

Figure 10.24. Energy balance for the base model.

Figure 10.24 shows the result of the energy balance, which is the difference between the change of energy of the system over time, dE_{sys}/dt, and the difference of the energy entering the system and the energy leaving the system, $\dot{E}_{in} - \dot{E}_{out}$. From the figure it is seen that the difference is in the order of 10^{-5}, which is assessed acceptable, and the system has continuity. The Lumped-Model-Model is thereby validated.

11 Model 2: FVM Model

This chapter presents the approach used for modelling the simplified TES system presented in section 6.2 page 23. This is the second model developed to represent the TES system, and it is based on the FVM theory presented in Chapter 8. The model is in the following termed the FVM-Model.

11.1 Purpose of the FVM-Model

The FVM-Model is set up in order to understand the temperature distribution throughout the concrete block and to evaluate the efficiency of the heat transfer from the concrete to the HTF.

11.2 FVM-Model Assumptions

For the model the following assumptions are made:

1. The TES system can be modelled as a 2D unsteady heat conduction problem.
2. The concrete block can be modelled as quadratic in the x, y-direction.
3. The centrally placed pipe can be modelled as quadratic in the x, y-direction.
4. The piping can be gathered as one centrally placed pipe with the same volume as the four individual pipes in total.
5. There is no heat flux across the outer boundaries of the total control volume due to the symmetric configuration of the entire storage system with multiple concrete elements with pipes.
6. There is no thermal contact resistance between the concrete and the pipe, *i.e.* the thermal contact is ideal.
7. The temperature of the metal pipe is the same as the temperature of the fluid flowing through the pipe, *i.e.* the thickness of the pipe is neglected.
8. The thermal conductivity, k, and the specific heat capacity, c_p, are constant averages based on linear functions throughout the concrete block.
9. In the concrete "slice" considered, along the z-direction, the HTF temperature in the pipe is constant. The model considers the inlet "slice".
10. The widths of the control volumes are constant and identical throughout the concrete block, $\delta x_{we} = \delta x_{sn} = \Delta x$, and $\Delta x = \Delta y$.
11. The geometry investigated is valid to represent the entire cross section of the concrete block.
12. The TES system is completely isolated. No energy losses to the surroundings are accounted for.

11.3 Geometry of the FVM-Model

While the Lumped-Mass-Model considers the xz-axis of the TES system, the FVM-Model considers the xy-axis as seen in Figure 6.6 page 23. In order to simplify the analysis only one of the 25 elements seen in Figure 6.6 is simulated, as it is assumed that one element represents the temperature behaviour in the entire concrete module. As seen in Figure 6.6, the element chosen can be placed anywhere within the module. Additionally, the round concrete element, with one single water pipe seen in Figure 6.7 page 23, is simplified to squares as illustrated in Figure 11.1.

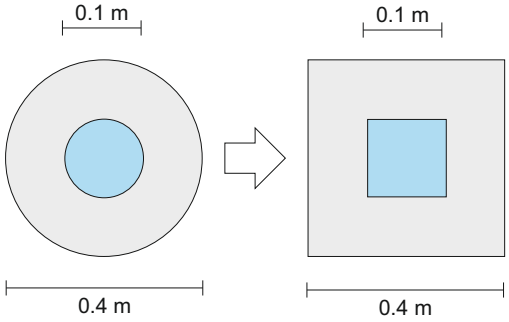

Figure 11.1. Simplification to square geometry chosen for the FVM-Model.

From Figure 11.1 it is seen how the round concrete element and water pipes are simplified to squares of the same dimensions. The geometry to the right is the geometry considered in the FVM-Model. As explained in Chapter 8, the geometry is divided into control volumes as seen in Figure 11.2. Also the control volumes are quadratic. The TES system is modelled in 2D in the x, y-plane.

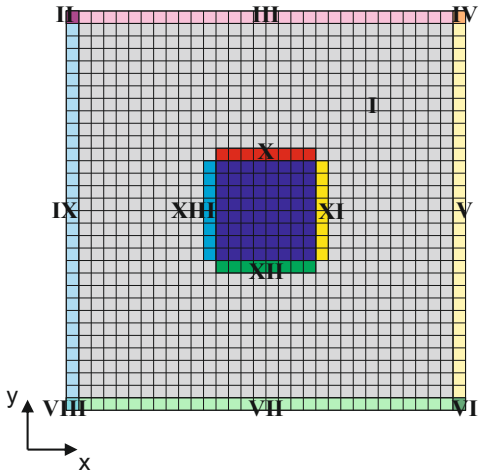

Figure 11.2. The geometry of the FVM-Model divided into quadratic control volumes.

From the figure it is seen that the geometry consists of a number of cells (control volumes), *i.e.* a grid is generated across the geometry, and that 13 different types of equations (indicated by I through XIII) need to be specified in order to evaluate the concrete temperature. These equations are developed from equation (8.10) page 34 and are given in Appendix E page 122.

11.4 Boundary Conditions, Weighting Parameter and Time Resolution

In the following, the boundary conditions, weighting parameter and time resolution used in the model is presented. In the TES system modelled two types of boundaries need to be considered:

1. At the interface between the concrete and the pipe, neglecting the pipe thickness: Here the boundary conditions equal the temperature of the flowing HTF.
2. At the outer boundaries: Here $\partial T/\partial x = 0$, which means that, due to symmetry, there is no heat transfer across the outer boundaries of the concrete-pipe section investigated.

The explicit scheme, resulting in $\theta = 0$, is used to solve the problem. This requires a time resolution of:

$$\Delta t < \rho \cdot c_p \cdot \frac{(\Delta x)^2}{2 \cdot k} \Rightarrow \Delta t < 2250\,\mathrm{kg\,m^{-3}} \cdot 1450.5\,\mathrm{J\,kg^{-1}\,K^{-1}} \cdot \frac{(0.0104\,\mathrm{m})^2}{2 \cdot 1.97\,\mathrm{W\,m^{-1}\,K^{-1}}} \tag{11.1}$$

$$\Rightarrow \Delta t < 129.5\,\mathrm{s} \tag{11.2}$$

The concrete density, ρ, is found in [Laing et al., 2012], while the specific heat capacity, c_p, and the thermal conductivity, k, are found from the equations (6.1) to (6.4) page 23. The calculation in (11.2) results in the physical time step limit for the system. In order to obey the physics, a Δt factor of 6 is chosen resulting in a $\Delta t = 129.5\,\mathrm{s}/6 \simeq 21.58\,\mathrm{s}$.

11.5 The FVM-modelling Approach

The FVM-Model is built up from the following steps:

1. Initialisation of the system
2. Creation of linear system of equations
3. Solution using functions
4. Efficiency calculations

11.5.1 Step 1: Initialisation of the System

In Step 1 the system is initialised. Input values for the number of cells (control volumes), the cells widths, the simulation time, the concrete density, the weighting parameter θ along with the initial water and concrete temperatures are defined. Furthermore, the time resolution is calculated from equation (11.1) page 57, and the specific heat capacity and thermal conductivity of Heatcrete® are calculated from the equations (6.3) and (6.4) page 23.

11.5.2 Step 2: Creation of Linear System of Equations

In Step 2 a linear system of equations, with initial matrix [K] and right side vector Q, is defined along with the initial temperatures T. The model loops for the pipe and the concrete block, respectively, dividing the concrete into upper (first 12 rows), left, right and lower parts (last 12 rows) compared to the location of the pipe cells. This can be seen in Figure 11.2 page 56.

11.5.3 Step 3: Solution using Functions

Before Step 3 two functions are called: "create_Matrix_K" resulting in a matrix and "create_RightSide_Q" resulting in a vector. The functions are composed of different types of equations, as explained in section 11.3 and seen in Figure 11.2 page 56. The equations are presented in Appendix E and are solved using the following built-in relationship in MATLAB [Lund and Condra, 2014]:

$$[K] \cdot \{T\} = \{Q\} \Rightarrow \{T\} = [K] \setminus \{Q\}' \tag{11.3}$$

where K is the left-side matrix, Q is the right-side vector ($'$ for transposed) and T is the concrete temperature. Both functions loop over time until the total simulation time is reached. In Step 3 the function results are used to calculate the concrete temperatures, from equation (11.3), in the cells.

11.5.4 Step 4: Efficiency Calculations

In Step 4 the efficiency calculations are made from one vertical vector, which is extracted from the temperature solutions. The vector extracted is shown in Figure 11.3 as a black arrow.

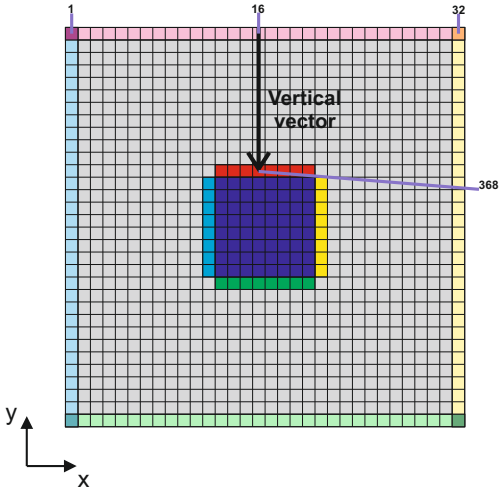

Figure 11.3. Efficiency vectors drawn from the concrete temperature solutions.

From the figure it is seen that the vertical vector covers the cells 16:32:368. The efficiency of the heat transfer through the concrete block is calculated as follows:

$$\text{Deviation}_{\text{storage}} = \frac{(T_{cell} - T_{ref})}{T_{ref}} \cdot 100 \Rightarrow \eta_{\text{storage}} = 100 - \text{Deviation}_{\text{storage}} \tag{11.4}$$

In equation (11.4) the deviation of the calculated temperatures are given compared to the reference temperature, which is the temperature closest to the pipe, *i.e.* cell 368 in the horisontal 8-cell-long red area in Figure 11.3.

In equation (11.4) the efficiency of the storage is calculated related to the simplification of modelling the concrete block as a lumped mass. The efficiency results are given in Chapter 13.

11.6 MATLAB Set-Up: The FVM-Model Walk-Through

In the following the input values to the FVM-Model are presented along with a flow diagram explaining the model walk-through. The input values are presented in Table 11.1.

Input parameter	**MATLAB Model Name**	**Value**
Number of cells in total	NoCells	1024
Number of cells covering the pipe	NoCells_Pipe	8
Weighting parameter	theta	0
Initial temperature of concrete	T_con	550+273.15 K
Temperature of water	T_wat	105+273.15 K
Simulation time	TotalTime	244 800 s (2.83 days)
Width of the concrete block	Width_con	0.4 m (2 m / 5)
Density of the concrete	rho_con	2250 kg m^{-3}

Table 11.1. Input values for the FVM-Model.

Figure 11.4 illustrates a flow diagram explaining the FVM-Model walk-through.

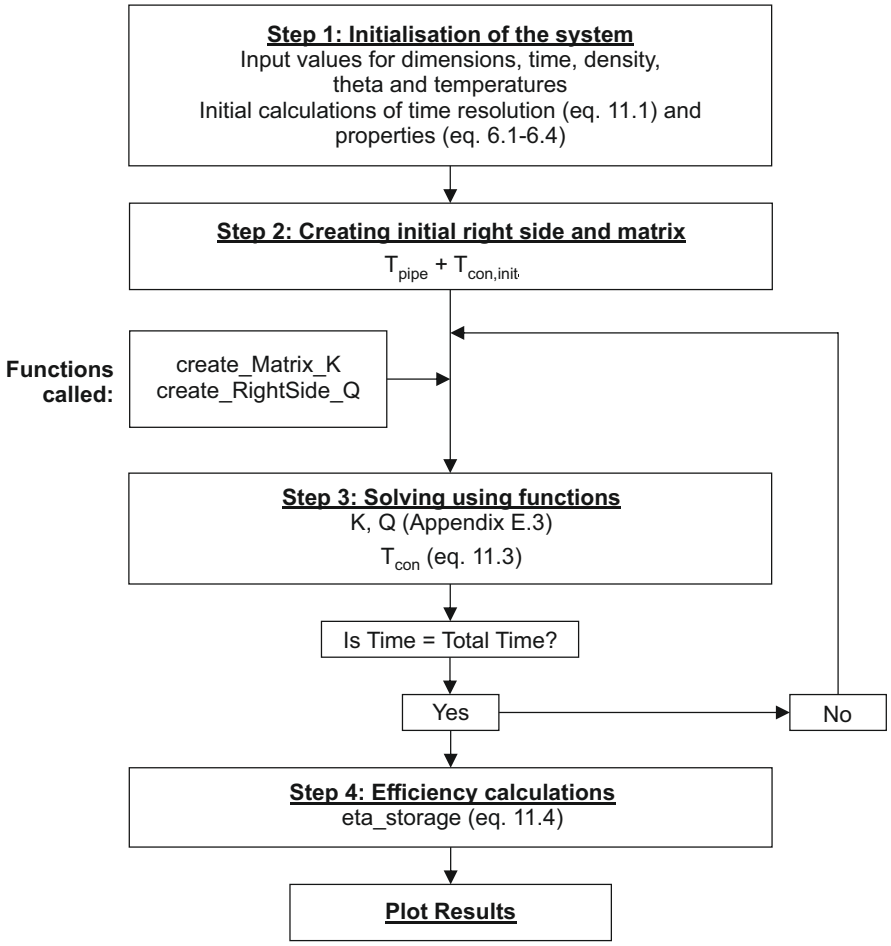

Figure 11.4. Flow diagram showing the set-up for the FVM-Model in MATLAB.

11.7 Grid Independence

Figure 11.2 page 56 is drawn with 1024 cells. However, a grid independence is needed in order to find a sufficiently accurate solution. In Appendix E a grid independence study is conducted with 256 cells (Run 2), 1024 cells (Run 1) and 4096 cells (Run 3), where vertical vectors are extracted from each run and compared. The three geometries to be compared are seen in Figure 11.5.

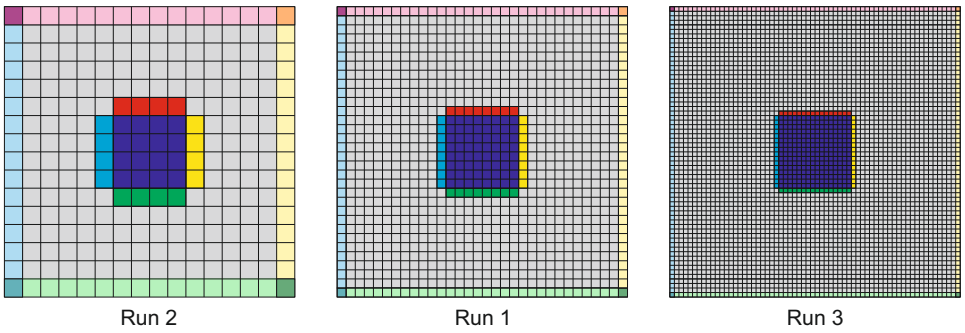

Figure 11.5. Run 1, Run 2 and Run 3 geometries compared in the FVM-Model.

From the figure it is seen that the concrete elements have the same outer dimensions, however with different number of cells. Run 1 corresponds to Run 2 refined, *i.e.* the number of cells are doubled in both directions, while Run 3 corresponds to Run 1 refined. This increases the number of cells covering the pipe along with the number of equations, given in Appendix E page 122, which

are solved in (11.3) page 57. The time resolutions (equation (11.1) page 57) are calculated to be $\Delta t < 21.58\,\text{s}$, $\Delta t < 86.32\,\text{s}$ and $\Delta t < 5.40\,\text{s}$ for Run 1, 2 and 3, respectively.

In order to compare the three simulations, two vectors are extracted from Run 1 (1024 cells), one vector is extracted from Run 2 (256 cells) and four vectors are extracted from Run 3 (4096 cells). Two elements have been chosen to be compared, the first and last element in the vectors. This means that one cell from Run 2 is compared to 4 cells from Run 1 and 16 cells from Run 3. For the first element, this is illustrated in Figure 11.6.

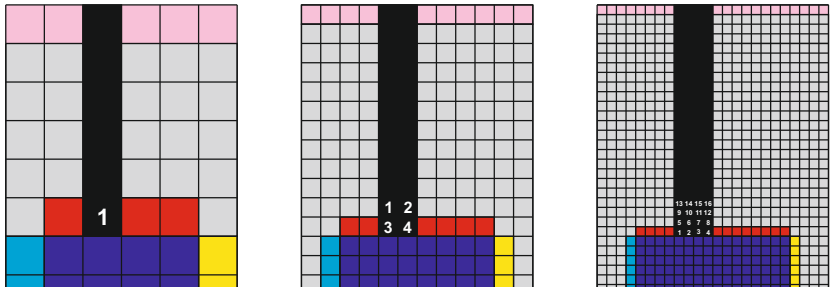

Figure 11.6. Illustration of cells in each run, which are compared in the FVM-Model.

As seen in Figure 11.6 one temperature value from Run 2 is compared to four temperature value in Run 1 and 16 temperature value in Run 3. An average is taken of the temperature values in Run 1 and Run 3 in in order to compare with Run 2. This is done for both the first and last element in the extracted vectors. The differences between the three simulations for the first and last element are given in the figures 11.7 and 11.8.

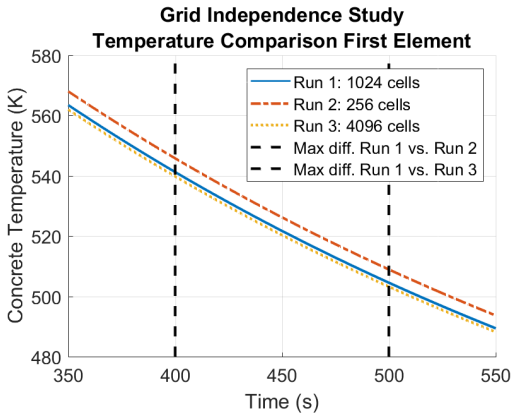

Figure 11.7. Comparison of the first element for Run 1, Run 2 and Run 3.

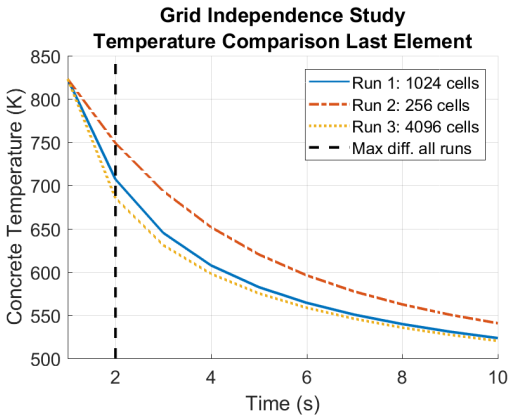

Figure 11.8. Comparison of the last element for Run 1, Run 2 and Run 3.

In Figure 11.7 the comparison of the three simulations in the first element (the arrowhead in Figure 11.3, *e.g.* cell 368) is shown over time. The maximum difference between Run 1 and Run 2 is found at $t = 400\,\text{s}$ and corresponds to at temperature difference of approximately 4 K at that time. The maximum difference between Run 1 and Run 3 is found at $t = 500\,\text{s}$ and corresponds to a temperature difference of approximately 2 K at that time. The similar is shown for the last element (the arrowroot in Figure 11.3, *e.g.* cell 16) in Figure 11.8, where the maximum difference between Run 1 and Run 2 is found at $t = 2\,\text{s}$ and corresponds to at temperature difference of approximately 40 K at that time. The maximum difference between Run 1 and Run 3 is found at $t = 2\,\text{s}$ and corresponds to at temperature difference of approximately 20 K at that time.

The study concludes that the geometry with 1024 cells is assessed acceptable, when the relatively

small deviations for the last element and the computational time is taken into consideration, since Run 3 takes 1.5 h to run, whereas Run 1 only takes approximately 2.5 min.

11.8 Model Evaluation

In this section the $k-$ and c_p-expressions for the DLR-concrete and the Heatcrete®, given in the equations (6.1) to (6.4) page 23, are investigated. The following figures show concrete temperature results after approximately 30 600 s corresponding to 8.5 h.

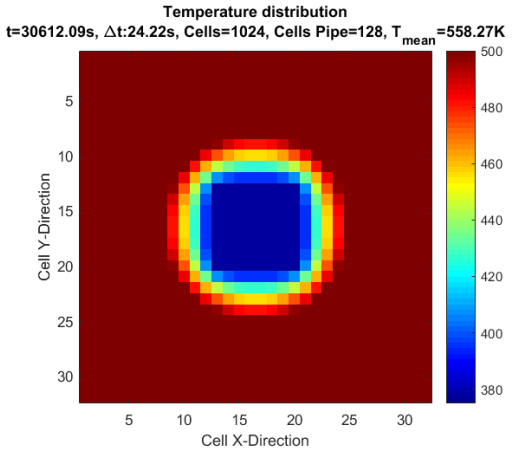

Figure 11.9. Concrete temperature after ∼ 30 600 s (DLR).

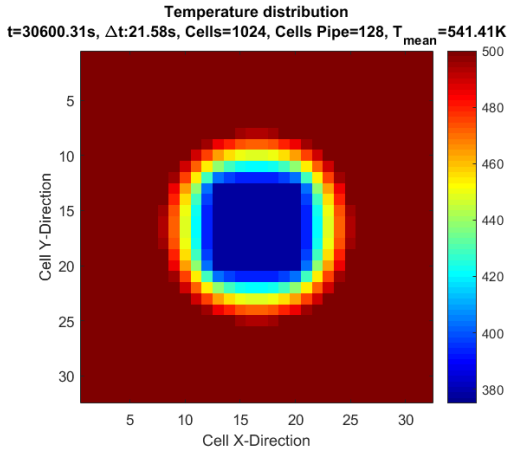

Figure 11.10. Concrete temperature after ∼ 30 600 s (Heatcrete®).

When comparing the two figures after approximately 8.5 h, it is seen that the Heatcrete® is cooled faster than the DLR-concrete. This can be seen from both the colouring of the concrete nearest the pipe and from the mean temperatures: $T_{mean} = 558.27\,\text{K} = 285.12°\text{C}$ for DLR and $T_{mean} = 541.41\,\text{K} = 268.26°\text{C}$ for Heatcrete®. This is due to the generally superior Heatcrete® properties compared to the DLR-concrete as seen in Figure 6.4 page 22. The following figures show concrete temperature results after approximately 91 800 s = 25.5 h.

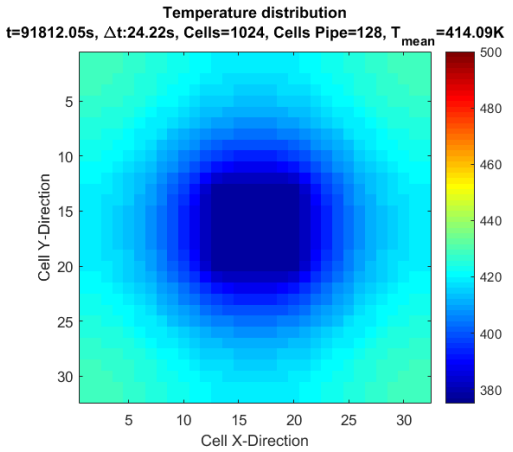

Figure 11.11. Concrete temperature after ∼ 91 800 s (DLR).

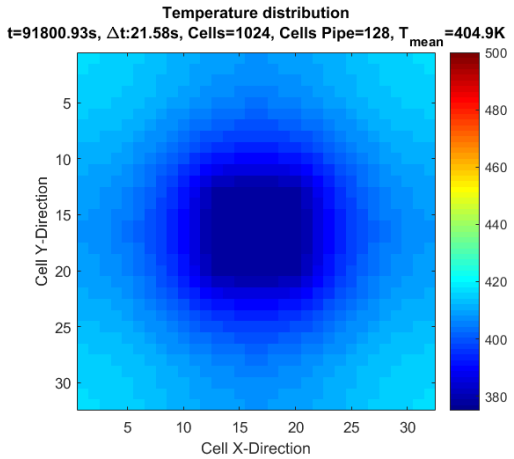

Figure 11.12. Concrete temperature after ∼ 91 800 s (Heatcrete®).

Similarly, after approximately 91 800 s the same tendencies are seen: Heatcrete® is again cooled faster than the DLR-concrete ($T_{mean} = 414.09\,\text{K} = 140.94°\text{C}$ for DLR and $T_{mean} = 404.90\,\text{K} = 131.75°\text{C}$ for Heatcrete®).

From the above evaluation it is assessed that the $k-$ and c_p-values used affect the discharge time of the TES system correctly: Higher values result in faster discharge. Based on the model built-up, presented in section 11.5, and the expressions used, the above results seem reasonable.

11.9 Model Validation: The Energy Balance

As the Lumped-Mass-Model, the FVM-Model is validated based on the system energy balance. For the FVM-Model, the energy balance is checked at a chosen known state, *i.e.* when the TES system is fully discharged and in steady state. At this state, after sufficiency long time with a continuous inlet HTF flow through the pipe, the HTF and concrete will obtain the same temperature of $378.15\,\mathrm{K} = 105°\mathrm{C}$, which is the inlet HTF temperature. When giving this temperature as inputs to the FVM-model for both the HTF flow and the concrete, the temperature of the concrete block should not change over time. This is shown in the following figures.

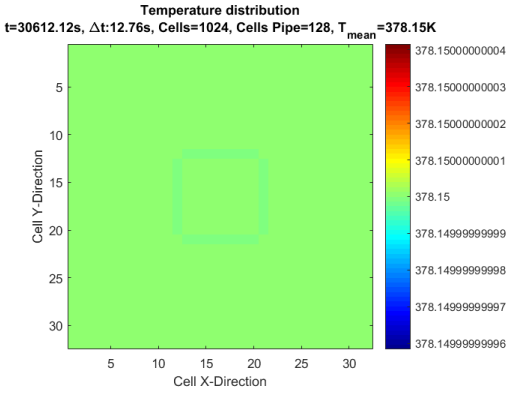

Figure 11.13. Concrete and HTF temperatures after $\sim 30\,612\,\mathrm{s}$ with same initial conditions.

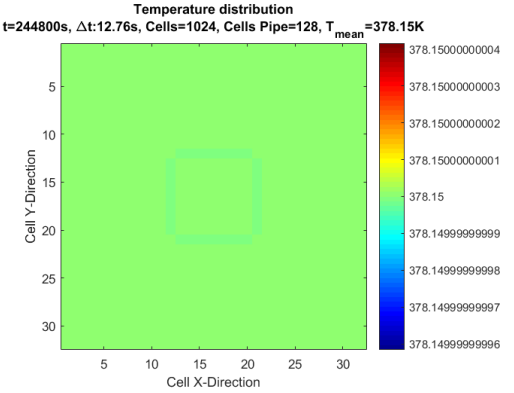

Figure 11.14. Concrete and HTF temperatures after $\sim$ 244 800 s with same initial conditions.

From the figures 11.13 and 11.14 it is seen that the temperatures of the concrete block and the inlet HTF flow remain equal and constant over time, as expected. It is seen that the temperature scale varies slightly, even though physically there should be no change. This variation is due to round-off in the MATLAB code when calculating. Since the change is extremely small, the energy is assessed in balance, and the system does not have any dynamics without the temperature difference between the concrete and HTF. Based on the above it is assessed, that the system has continuity, and the FVM-Model is thereby validated.

Part IV

Analysis and Discussion

12 Model Results

This chapter presents the final results from the Lumped-Mass-Model and the FVM-model. In the chapter the models are run with input values partly based on the model evaluations presented in the chapters 10 and 11 and partly on the knowledge of the TES system. It should be noticed that the x-axes in the following figures vary in order to highlight the significant progressions.

12.1 Results from the Lumped-Mass-Model

In the Lumped-Mass-Model the following values are chosen for the final results: n = 100, m_dot = 10 $\mathrm{kg\,s^{-1}}$, dt = 0.5 s and P = f(T_c,ΔT_{pinch}). Additionally, the values in Table 10.1 page 46 are applied. In the following, plots of the concrete and HTF element temperatures, the HTF element qualities, the heat transferred and the work produced by the turbine are shown over time. First, figures of the concrete and HTF element temperatures are given.

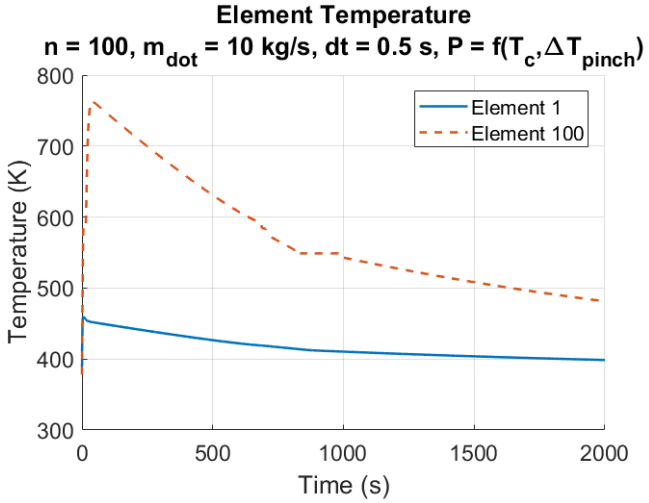

Figure 12.1. Temperature of the first and last HTF element after 2000 s.

From Figure 12.1 similar tendencies of what is presented in section 10.5 is found. It is seen that, for the first HTF element (the **blue line**), the temperature increases rapidly, hereafter decreases, and it never reaches the saturation temperature, as in Figure 10.9 page 48. For the last HTF element (the **red line**), it is seen that the temperature reaches approximately 762 K = 489°C and decreases until the saturation temperature is reached after 687 s. In the time range of [687 ; 989] s the HTF element temperature is at the saturation temperature but since the pressure decreases, the saturation temperature also decreases in this range. Hereafter the HTF element temperature keeps decreasing until the water inlet temperature of 378.15 K = 105°C is reached after approximately 20 000 s = 5.56 h (not shown). However, after approximately 10 000 s = 2.78 h, a temperature of 381.5 K = 108.5°C, which corresponds to a temperature decrease of barely 4 K over the last 2.78 h.

In the following figure a 3D plot of the concrete and HTF element temperatures is given in the time range [0 ; 2000] s.

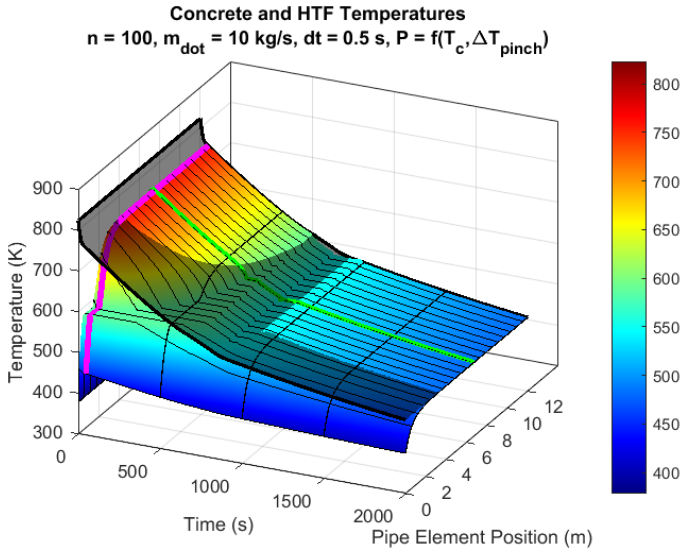

Figure 12.2. 3D plot of the concrete and HTF temperatures after 2000 s.

In Figure 12.2 it is seen that the concrete temperature (the "dark plate") decreases rapidly in the first approximately 14 s, as in Figure 10.13 page 49, due to the relatively high temperature difference between the concrete and HTF. It is seen that the concrete temperature experiences two "bends" during the discharge time of 2,000 s. The first bend occurs after approximately 20 s, when the HTF elements are heated to the concrete temperature, and the temperature difference between the two becomes relatively small (approximately 15 K). The second bend occurs after approximately 900 s, when the pressure has decreased to 60 bar, and the elements are leaving the saturation state. Hereafter, the temperature difference between the concrete and the HTF elements becomes even smaller (approximately 2 K).

Figure 12.3 illustrates some observations of the concrete and HTF temperatures occurring in the time range of [670 ; 1020] s, where the temperature is affected by the pressure decrease.

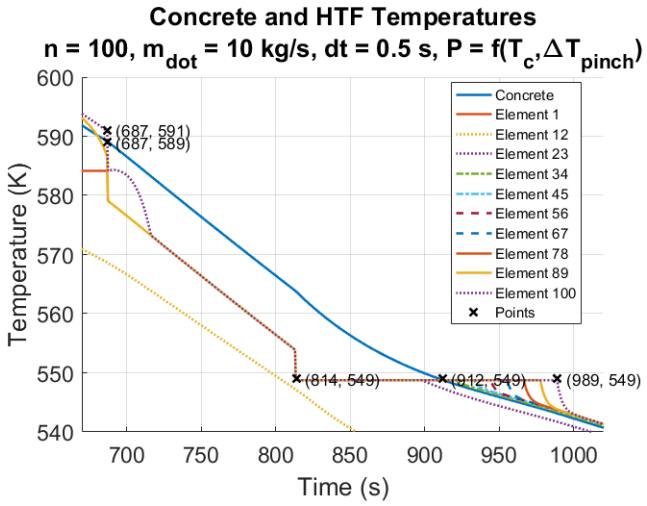

Figure 12.3. Concrete and HTF temperature observations between 670 s and 1020 s.

In Figure 12.3 several points are highlighted. Between the points (687, 591) and (814, 549) the pressure decreases (as seen in Figure 10.23 page 53), meaning that above point (687, 591) the pressure is 100 bar, and below point (814, 549) it is 60 bar. The decrease in pressure (in the time range [686 ; 814] s) causes the saturation temperature to decrease as well. Between the points

(687, 589) and (912, 549) the concrete decreases unaffected, however, the HTF temperatures are affected by the pressure decrease, and decreases to the corresponding saturation temperature. Between the points (814, 549) and (989, 549) the HTF elements leaves the saturation state in turn. The last HTF element is the last element to leave the saturation state, and the temperatures of the HTF elements again surpass the concrete temperature, as seen for 100 bar. This is due the simplification of the concrete block being lumped as explained below Figure 10.13 page 49.

Figure 12.4 illustrates how the quality of the HTF elements changes over time.

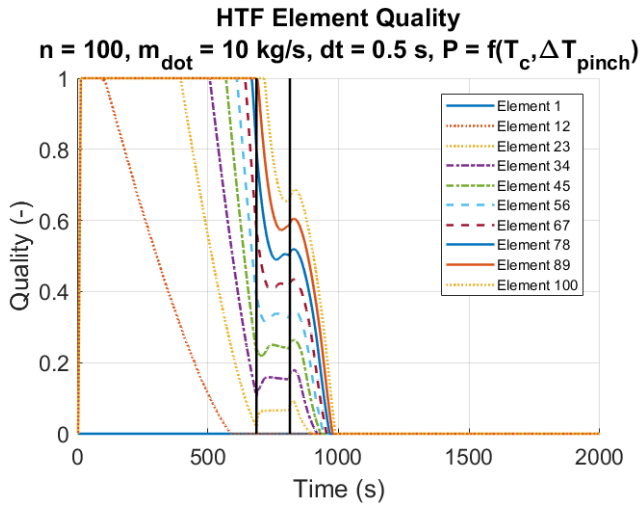

Figure 12.4. HTF quality after 2000 s.

The figure shows that all HTF elements starts out as liquid water (quality = 0). Subsequently, all shown HTF elements, except element 1, rapidly change phase from water to steam as seen in Figure 10.22 page 52, where the elements are rapidly heated by the concrete. Due to the continuous water inlet flow of 378.15 K = 105°C, the HTF elements change phase from steam to water in turn with the HTF elements closest to the inlet changing first, since these are the elements to first experience the inlet water. In the time range of [686 ; 814] s (indicated by vertical black lines) the phase change is affected by the pressure decrease. Before the pressure change, *i.e.* when the pressure is 100 bar, the quality decreases approximately linearly. While the pressure is decreasing from 100 bar to 60 bar, the quality varies due to the change in element energy as seen in Figure 12.5. The remaining part of the quality progression is explained after Figure 12.5.

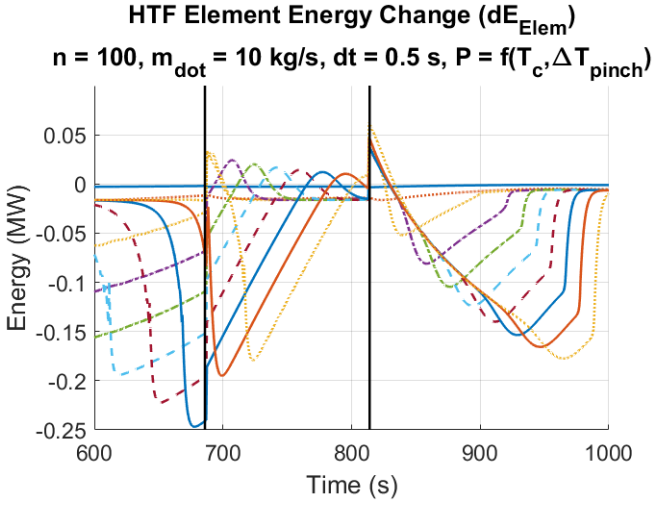

Figure 12.5. Observation of change in element energy, dE_Elem, between 600 s and 1000 s.

Figure 12.5 shows how the HTF element energy change in the time range [600 ; 1000] s. It should be noticed, that a legend is missing. However, the different HTF elements can be distinguished based on the legend in Figure 12.4. When the pressure decreases, between the two black lines, it is seen that "waves" occur due to the energies entering and leaving, respectively, which change.

After the pressure has decreased to 60 bar and becomes constant, in Figure 12.4, it is seen that the quality increases slightly before decreasing again. This is due to the increase in the temperature difference between the concrete and HTF elements, as seen in Figure 12.3 page 66, which occurs after 814 s. At this very second the pressure reaches the lower pressure limit of 60 bar, and this causes the quality to increase slightly, as the temperature difference increases slightly, and more heat is transferred from the concrete to the HTF. The above is seen, when observing Figure 12.6 around $t = 814$ s.

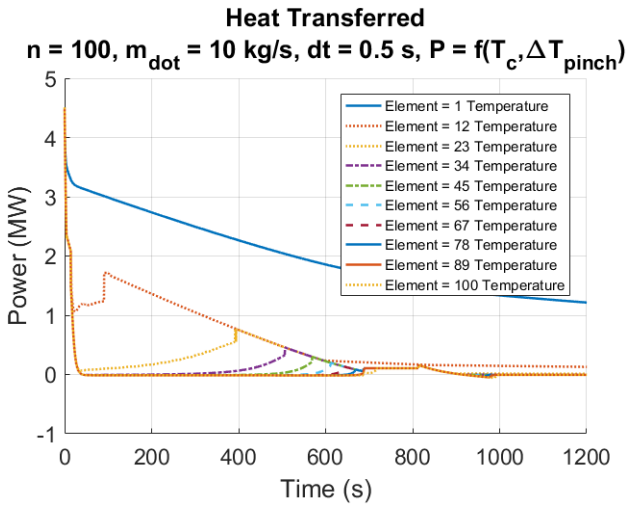

Figure 12.6. Heat transferred from the concrete to the HTF elements after 1200 s.

From Figure 12.6 it is seen that the largest amount of heat is transferred within the first 1000 s of the discharge. Hereafter, the heat transferred is close to zero due to the relatively small temperature difference between the concrete block and the HTF elements. After 1000 s the remaining discharge of the TES system occurs rather slow. At $t = 814$ s a small peak in energy is visible due to the pressure reaching the lower limit, which affects the temperature difference as explained. When comparing Figure 12.6 with Figure 12.4, it is also seen that after 1000 s all the HTF elements have changed phase from steam to water. Additionally, it is seen that the heat transferred decreases with the elements over time, since the temperature difference between the concrete block to the HTF elements decrease with the elements.

Figure 12.7 illustrates the work produced by the turbine over time.

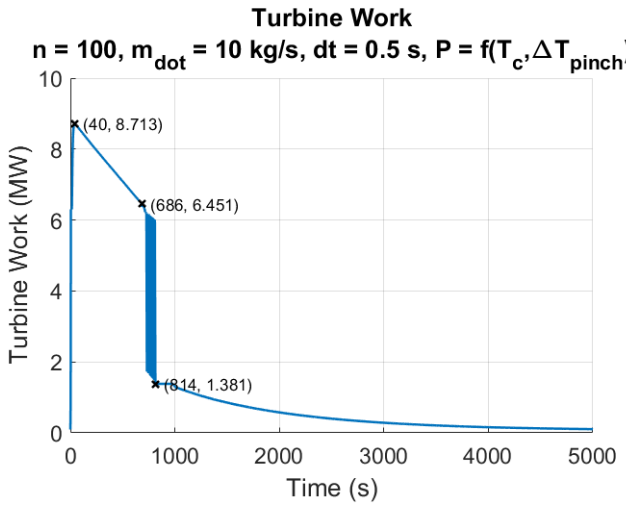

Figure 12.7. Turbine work after 5000 s

From Figure 12.7 it is seen that the turbine work depends on both the temperatures and the pressure of the HTF elements entering the turbine. The rapid increase in the first approximately 40 s is due to the assumption that initially the pipe is filled with water, as seen in Figure 12.1 page 65. Hereafter, in the range of [40 ; 686] s the turbine work decreases linearly due to the decrease in temperature, while the pressure is constant at 100 bar. In the time range of [686 ; 814] s both the pressure and temperature decreases, as seen in the figures 10.23 page 53 and Figure 12.8 below, however, it is seen that the turbine work fluctuates. This behaviour is further investigated below.

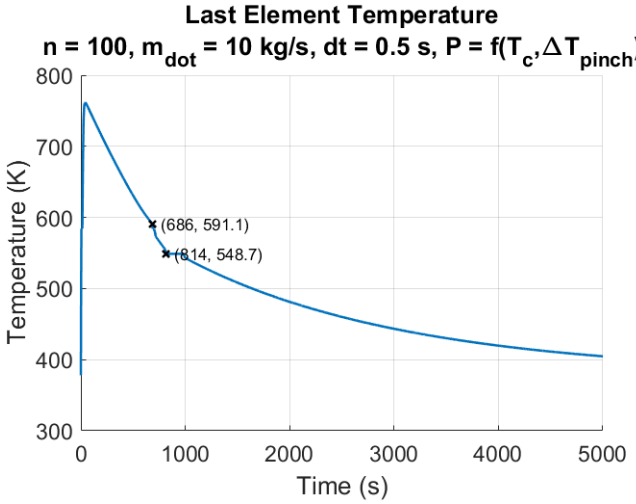

Figure 12.8. Last HTF element with highlighted points after 5000 s.

When observing Figure 10.23 page 53 along with Figure 12.8 above it is seen that neither the pressure nor the temperature fluctuates like the turbine work. When further investigating the MATLAB code and data, the issue seems to originate from *refprop*.

In this section final results from the Lumped-Mass-Model have been presented, and tendencies for the concrete and HTF element temperatures, the HTF element qualities, the heat transferred and the work produced by the turbine have been investigated over time. The concrete temperature is seen to continuously decrease over time, as expected, since heat is continuously transferred to the HTF elements. The temperatures of the HTF elements generally decrease with time and element,

since the amount of heat transferred decreases, as the TES system is discharged. The HTF element qualities changes phase from liquid water to steam to liquid water again over time with the last element entering the pipe changing into liquid water as the last. In general, the heat transferred from the concrete to the HTF elements decrease, when the temperature difference decreases. The temperature difference is highest in the beginning of the discharging. The work produced by the turbine generally follows the tendencies found for the pressure and temperature of the last HTF element, and as the temperature, pressure and heat transferred, also the turbine work decreases over time.

12.2 Results from the FVM-Model

In the FVM-Model the $k-$ and c_p-expressions for Heatcrete®, given in the equations (6.3) and (6.4) page 23, are used. Additionally, the values in Table 11.1 page 58 are applied. In the following, figures of the concrete temperature gradient is shown over time. The TES system is modelled in 2D in the x, y-plane. Figure 12.9 shows the initial conditions for the TES system, and Figure 12.10 shows the TES system after approximately 61 200 s corresponding to 17 h.

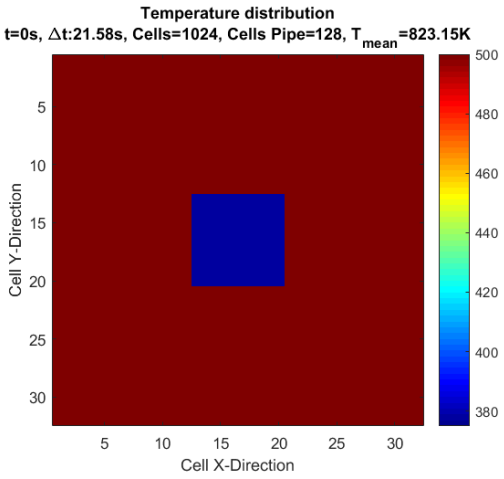

Figure 12.9. Initial temperatures of the FVM-model.

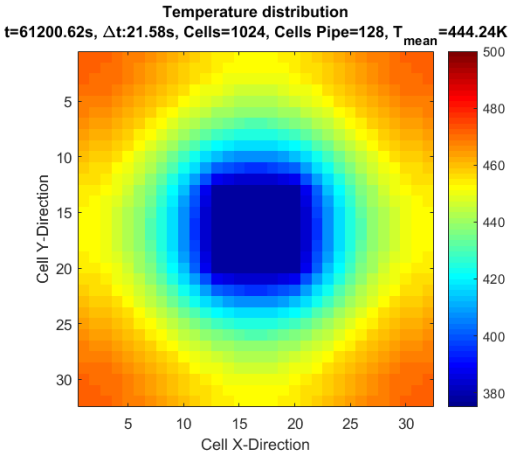

Figure 12.10. Temperatures of the FVM-Model after $\sim$ 61 200 s.

In Figure 12.9 the initial conditions for the TES system are shown: the concrete block (seen in dark red) starts with a uniform temperature of 823.15 K = 550°C, while the HTF flow in the centred pipe (seen in blue) has a temperature of 378.15 K = 105°C.

In Figure 12.10 the TES system is shown after approximately 61 200 s corresponding to 17 h. From the figure it is seen that the temperature of the concrete block has decreased differently from the centred pipe throughout the concrete. Closest to the pipe, the temperature has decreased the most, and furthest from the pipe, the temperature has decreased the least. Comparing to the initial conditions, seen in Figure 12.9, the mean temperature, T_{mean}, has decreased from 823.15 K to 444.24 K = 171.09°C. Due to the squared pipe, the temperature gradients becomes edged. It should be noted that the HTF flow in the centred pipe does not change temperature over time, since the FVM-Model only considers the inlet "slice" of the TES system as explained in section 11.2 page 55.

In the following, Figure 12.11 shows results after $\sim 122\,400\,\text{s}$ correspoding to $\sim 34\,\text{h}$, and Figure 12.12 shows the results after $\sim 244\,800\,\text{s}$ corresponding to $\sim 68\,\text{h}$.

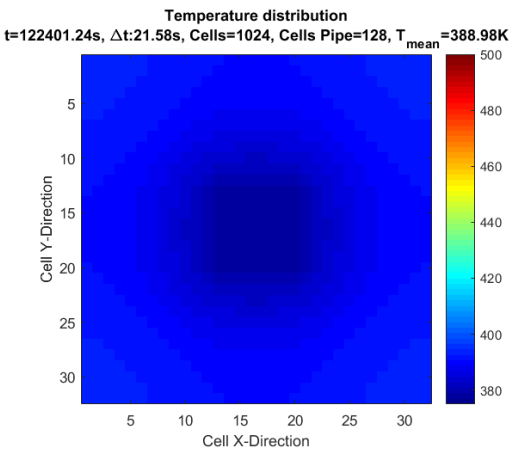

Figure 12.11. Temperatures of the FVM-model after $\sim 122\,400\,\text{s}$.

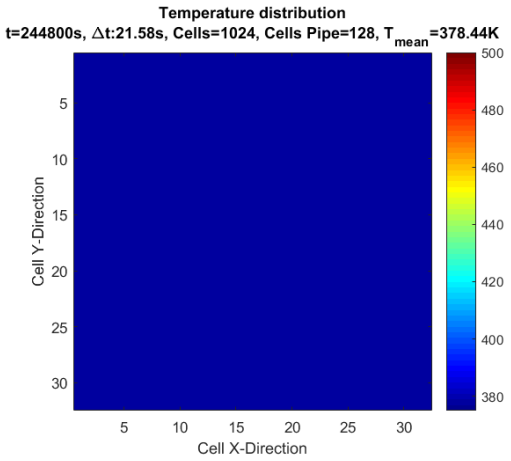

Figure 12.12. Temperatures of the FVM-model after $\sim 244\,800\,\text{s}$.

In Figure 12.11 the TES system is shown after approximately $122\,400\,\text{s}$ corresponding to $34\,\text{h}$. As for Figure 12.10, Figure 12.11 shows a decreasing temperature gradient throughout the concrete block. It is seen that the temperature in general is close to the HTF temperature, meaning that the TES system is close to being completely discharged. The mean temperature, T_{mean}, has decreased to $388.98\,\text{K} = 115.83°\text{C}$, which is only approximately $10\,\text{K}$ above the HTF inlet temperature.

In Figure 12.12 the final conditions for the TES system are shown: the concrete block has cooled down to the HTF inlet temperature, meaning that the TES system is fully discharged. From Figure 12.11 to Figure 12.12 additionally $34\,\text{h}$ have passed in order for the TES system to decrease the remaining $10\,\text{K}$. It is, however, not assessed useful to spend $34\,\text{h}$ for only $10\,\text{K}$, and the TES system might be considered discharged after $34\,\text{h}$ as seen in Figure 12.11. The TES system could even be considered discharged after approximately $91\,800\,\text{s}$ corresponding to $25.5\,\text{h}$, as seen in Figure 11.12 page 61, where approximately $25\,\text{K}$ remains stored in the TES system.

In the following figures, selected cells from the vertical vector, seen in Figure 11.3 page 58, are extracted and shown over time.

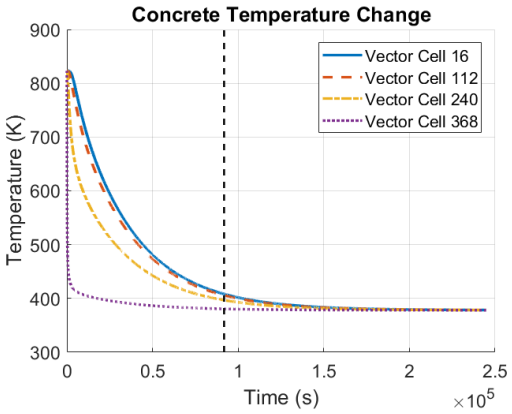

Figure 12.13. Temperature gradients throughout the concrete block after after $\sim 244\,800\,\text{s}$.

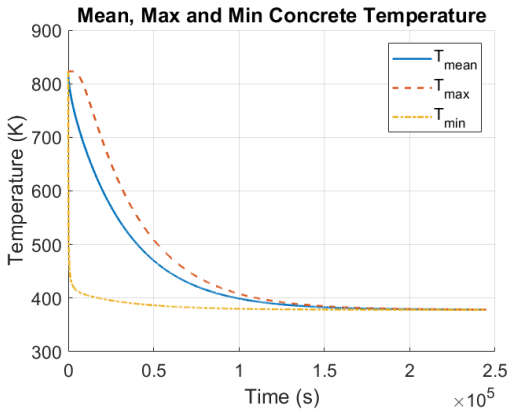

Figure 12.14. Mean, maximum and minimum concrete temperatures after $\sim 244\,800\,\text{s}$.

Figure 12.13 shows the temperature gradient through the cells 16, 112, 240 and 368 (as seen in

Figure 11.3 page 58), where Cell 16 is the cell furthest from the HTF flow within the centred pipe, and Cell 368 is the cell closest to the HTF flow. From the figure it is seen that the cell closest to the HTF flow (Cell 368) decreases fastest over time, while the cell furthest from the HTF flow (Cell 16) decreases the least. This agrees with what is found in the previous figures in this section. The vertical black line corresponds to 25.5 h, as discussed for Figure 12.12.

Figure 12.14 shows the mean, maximum and minimum temperatures of the concrete block over time. From the figure it is seen that the minimum temperature decreases fastest, since this temperature is found close to the HTF flow. The maximum temperature decreases the least, and the mean temperature is between the two, as expected.

In this section final results from the FVM-model have been presented, and it is found that the TES system has a decreasing temperature gradient throughout the concrete over time. The TES system is fully discharged after 244 800 s corresponding to 68 h, however, after 91 800 s corresponding to 25.5 h the remaining energy stored (*i.e.* in the form of a temperature difference of approximately 25 K between the concrete and the HTF) can be considered useless, since it takes barely two extra days to extract the remaining energy stored and fully discharge the TES system.

13 Model Coupling

This chapter presents the approach used for coupling the Lumped-Mass-Model and the FVM-Model. In the chapter the Biot number is evaluated, an efficiency analogy is drawn, and results of the coupling are given.

13.1 Calculation of the Biot Number

The Lumped-Mass-Model simulates the TES system, while considering the concrete block as a lumped mass. Whether the concrete block can be considered as a lumped mass or not is determined by the Biot number, as presented in section 7.2 page 31. The Biot number is calculated, following equation (7.11) page 31, as:

$$\mathrm{Bi} = \frac{3700\,\mathrm{W\,m^{-2}\,K^{-1}} \cdot 0.3\,\mathrm{m}}{2.0\,\mathrm{W\,m^{-1}\,K^{-1}}} = 555 > 0.1 \tag{13.1}$$

where 0.3 m is the diameter of the concrete element with the centred pipe diameter subtracted. From the above calculation, it is seen that the criteria for the Biot number is violated, even for the smallest value of the heat transfer coefficient. This is partly due to the size of the concrete, which is too large to be considered a lumped mass. Additionally, in this context, the heat transfer coefficient is relatively large, and the thermal conductivity is relatively small. This means that, in reality, a temperature gradient throughout the concrete block would be present and affect the discharge time, which increases with a temperature gradient present. The Biot number violation can be accounted for by introducing an efficiency of the temperature gradient throughout the concrete block. This can be done by coupling the Lumped-Mass-Model and the FVM-Model, since the FVM-Model simulates the temperature gradient throughout the concrete block. The models are coupled based on the fin efficiency analogy presented in Chapter 9 page 37.

13.2 Coupling of the Developed Models

In the Lumped-Mass-Model a heat transfer rate analogical to the ideal heat transfer rate from the fin is found as equation 7.1 in section 7.1 page 29. The heat transfer is multiplied by the efficiency calculated in the FVM-Model in section 11.6 page 58:

$$\eta_{\text{storage}} = 100 - \frac{(T_{cell} - T_{ref})}{T_{ref}} \cdot 100 = 85.92\% \tag{13.2}$$

where T_{cell} are temperatures in the extracted vector, seen in Figure 11.3 page 58, and T_{ref} is the reference temperature defined as the temperature nearest the pipe (cell 368). The above is inserted in equation (9.1) page 37 but since the efficiency drawn from the geometry is a matrix, the mean is taken from the vector leading to:

$$\dot{Q}_{actual} = \overline{\eta}_{\text{storage}} \cdot \dot{Q}_{lumped} \tag{13.3}$$

where $\overline{\eta}_{\text{storage}}$ is an average efficiency over time and elements. Equation (13.3) leads to the observations presented in the following. First, the temperature progression within the TES system is shown with an efficiency of 100% (the Lumped-Mass-Model alone), subsequently with the calculated efficiency of 85.92% from the FVM-Model, and finally the temperature progression

with an efficiency of 50% is shown in order to see how much the efficiency affects the final results. In Figure 13.1 the temperature progression with 100% efficiency is shown.

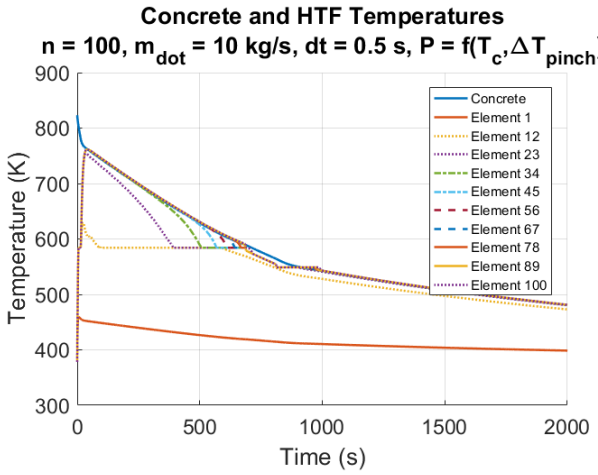

Figure 13.1. Temperature results from the Lumped-Mass-Model with an efficiency of 100%.

Figure 13.1 shows the temperature progression, as analysed in section 12.1 page 65, where the HTF temperatures generally decreases over time. The figure shows 10 HTF elements, where the temperatures decrease the most for the first elements, *i.e.* the elements first entering the pipe. In the following, temperature progressions with implemented efficiencies are shown.

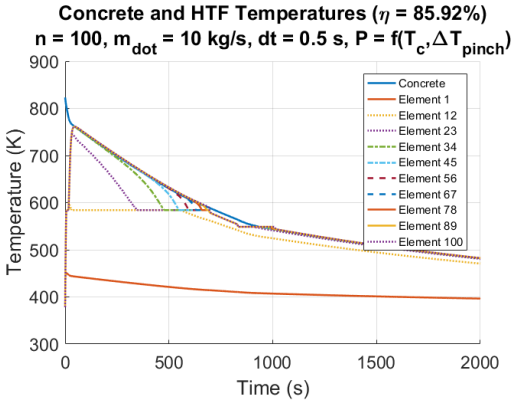

Figure 13.2. Temperature results from the Lumped-Mass-Model with an efficiency of 85.92%.

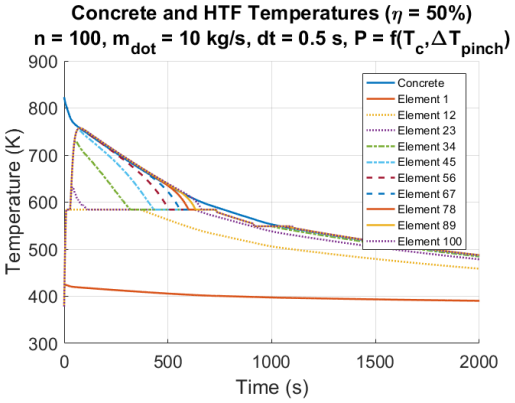

Figure 13.3. Temperature results from the Lumped-Mass-Model with an efficiency of 50%.

In Figure 13.2 it is found, when comparing to Figure 13.1, that *e.g.* element 23 (the **purple line** in both) peaks at 756.2 K corresponding to 483°C at 100% efficiency, while the peak occurs at 746.1 K corresponding to 473°C, later in time, at ∼86% efficiency. Additionally, it is found that element 23 reaches the saturation state after 395 s at 100% efficiency, while the saturation state is reached after only 348 s at ∼86% efficiency.

However, when looking at the temperature of element 23 after 2000 s, a temperature of 480.4 K corresponding to 207°C at 100% efficiency is found, while a temperature of 480.7 K corresponding to 208°C is found at ∼86% efficiency, *i.e.* the temperature is slightly higher for the lower efficiency. The same tendency is found for element 12 (the **yellow line**), element 34 (the **green line**), etc. In Figure 13.3, showing an efficiency of 50%, the same tendencies are found, when comparing to the other efficiencies. This means that even though the temperatures at the lower efficiency appear low in the beginning of the discharge, the temperature progressions are shifted, resulting in the

temperatures for the lower efficiencies to be higher later in the discharge process. This is further seen in Figure 13.4 below.

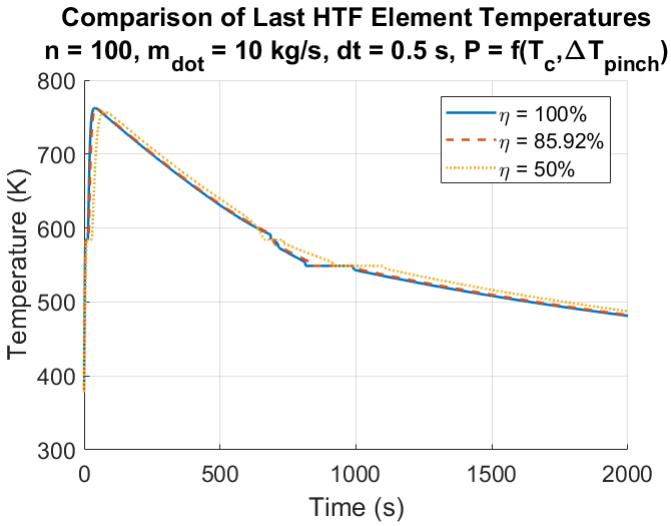

Figure 13.4. Temperature progressions of the last HTF element at efficiencies of $\eta = 100\%$, $\eta \sim 86\%$ and $\eta = 50\%$.

Figure 13.4 shows how the temperature progressions with efficiencies are shifted in time, compared to the results from the Lumped-Mass-Model with 100% efficiency. This results in the lower efficiency progressions to generally results in higher temperatures, at the same times, compared to the Lumped-Mass-Model. From the physical understanding of the TES systems modelled, this is due to the concrete block, with a temperature gradient, storing high-temperature energy furthest from the HTF flow longer, while the lumped concrete block corresponding to 100% has a uniform decreasing temperature over time. This means that every second the total lumped concrete block changes temperature, while the concrete block with a temperature gradient, only partly decreases in temperature nearest the HTF flow. This behaviour is further described below.

In the following, the efficiency influence is investigated for the heat transferred from the concrete to the HTF elements, since this is where the efficiency is implemented in the model as seen in equation (13.3) page 73.

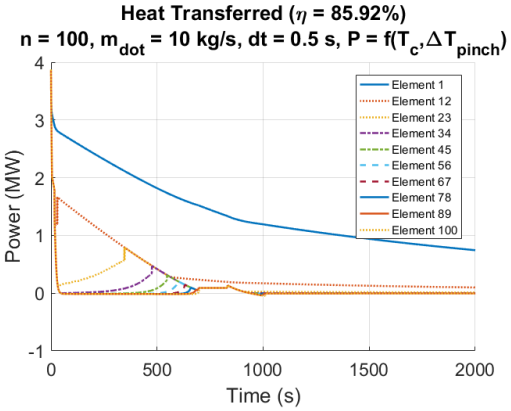

Figure 13.5. Heat transfer rate results from the Lumped-Mass-Model with an efficiency of 85.92%.

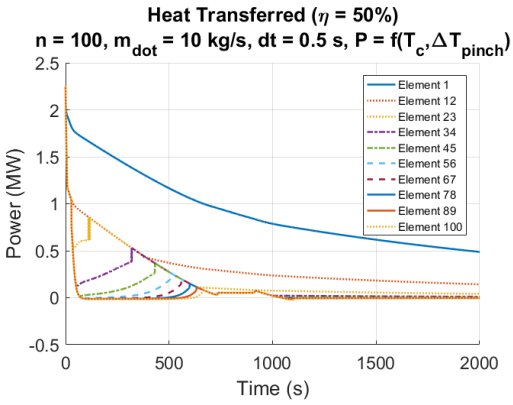

Figure 13.6. Heat transfer rate results from the Lumped-Mass-Model with an efficiency of 50%.

When comparing the above figures to Figure 12.6 page 68, the opposite tendency as for the

temperatures is found, *i.e.* the heat transfer peaks occur earlier in time for the lower efficiencies. When looking at element 23 (the **yellow line** in both) a peak at 0.788×10^6 W after 348 s at ~86% efficiency is found, while the peak occurs at 0.847×10^6 W after 118 s, *i.e* earlier in time, at 50% efficiency. The same tendencies are found for element 34 (the **purple line** in both) etc. However, for the HTF elements before element 23, - *i.e* element 1 (the **blue line**) and element 12 (the **red line**) - the peaks are different. The **blue line** never peaks but only decreases, since the temperature of this element never reaches the saturation temperature. The **red line**, on the other hand, peaks at 1.672×10^6 W after 29 s in Figure 13.5 but never peaks in Figure 13.6 due the saturation temperature, which is not reached. When looking at the heat transfer rate after 2000 s, element 1 (the **blue line**) has reached values of 0.744×10^6 W and 0.487×10^6 W for the efficiencies of ~86% and 50%, respectively. The values of element 12 (the **red line**) are 0.098×10^6 W and 0.143×10^6 W for the efficiencies of ~86% and 50%, respectively. This latter tendency is similar for element 23 (the **yellow line**).

From the temperature progressions given above, it was found that a decrease in efficiency resulted in a slightly higher temperature after *e.g.* 2000 s. This tendency can be explained by observing Figure 13.7 illustrating the two TES systems.

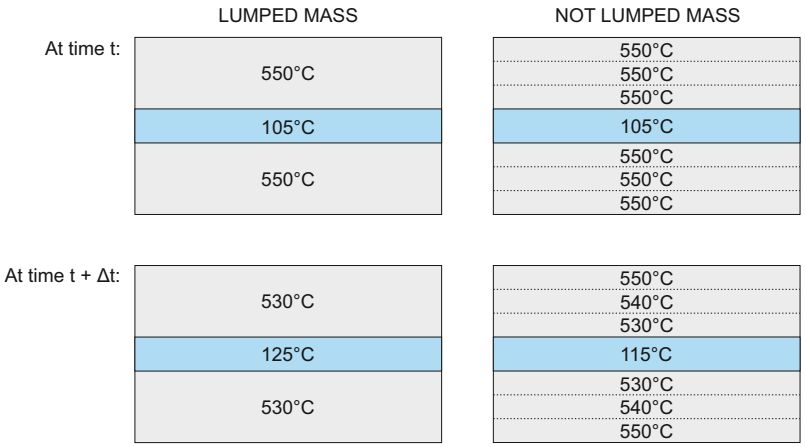

Figure 13.7. Lumped mass TES system versus TES system with temperature gradient principle.

In Figure 13.7 the lumped mass TES system with an efficiency of 100% is given to the left, while the TES system with a temperature gradient throughout the concrete is given to the right. Both systems starts out at $T_{con} = 550°C$ and $T_{HTF} = 105°C$. After a given amount of time the temperature of the lumped mass TES system has decreased to $T_{con} = 530°C$, and the TES system with the temperature gradient has obtained the same, however with a mean temperature of $T_{con,mean} = 540°C$. This means that the lumped mass TES system has transferred energy, corresponding to 20°C, to the HTF, resulting in a temperature difference of $\Delta T = 405°C$, while the TES system with the temperature gradient has transferred 10°C to the HTF, resulting in a temperature difference of $\Delta T = 415°C$. This means that, with the implemented efficiency, the temperature difference in $\dot{Q} = U \cdot A \cdot \Delta T$ is higher due to the temperature gradient throughout the concrete. This is what is observed in Figure 13.4 page 75. The higher temperature difference does, however, not compensate for the efficiency value implemented, thereby resulting in an overall lower heat transfer rate ($\dot{Q} \cdot 0.86 \rightarrow \dot{Q} \downarrow$).

This chapter has investigated a fin efficiency analogy coupling of the two developed models: the Lumped-Mass-Model and the FVM-Model. Based on the above findings, it is assessed that a temperature gradient throughout the concrete, increases the overall performance of the TES system. This is found, since the gradient results in generally higher HTF temperatures along with a generally higher temperature difference between the concrete and the HTF elements, subsequently resulting in a higher heat transfer rate at the same time.

14 Discharge Scenarios

This chapter presents results from different discharge scenarios investigated. First, the scenarios are explained, and subsequently the results are shown. For each scenario the results are discussed.

14.1 Scenarios Investigated

The scenarios investigated can be grouped into two overall investigations with sub points:

1. Short-term storage vs. Long-term storage
    a) Discharge at same outlet temperature
    b) Discharge at same time
2. Normal size storage vs. Double size storage
    a) Size x 1 (as used in the report)
    b) Size x 2 (concrete mass and number of pipes doubled)

Scenario 1 investigates the discharge time, *i.e.* short-term storage vs. long-term storage. The times are reached by varying the mass flow rate. In the scenario, two strategies are followed: 1.a) Discharging until the same outlet temperature is reached and 1.b) Discharging until the same time is reached. These strategies result in different values for the system pressure, the energy extracted from the TES system and the turbine work produced.

Scenario 2 investigates the size of the TES system, *i.e.* the size x 1 (the size modelled and analysed in the previous chapters) vs. the size x 2 (pipes and amount of concrete are doubled). The investigation results in values for the energy extracted from each TES system and the turbine work produced. Furthermore, the costs of each TES system size are also calculated and considered.

14.1.1 Short-term storage vs. Long-term storage

In the short-term/long-term investigation, three discharge times are obtained; one for each of the mass flow rates investigated. The mass flow rates and discharge times are given in Table 14.1.

	Mass flow rate, $\dot{m}$ ($\mathrm{kg\,s^{-1}}$)	Discharge time (s)
Short-term storage	15	3900 s (1.08 h)
Intermediate-term storage	10	5791 s (1.6 h)
Long-term storage	5	11 460 s (3.18 h)

Table 14.1. The mass flow rates and discharge times for the short-term storage versus long-term storage.

In the following, scenario 1.a is presented and discussed.

Discharge at Same Temperature

In this section the discharge of the TES storage is investigated, when discharging to the same temperature, *i.e.* $T_{\text{last element}} = 397\,\mathrm{K} = 123.85°\mathrm{C}$ for all three mass flow rates investigated, $\dot{m} = 5\,\mathrm{kg\,s^{-1}}$, $\dot{m} = 10\,\mathrm{kg\,s^{-1}}$ and $\dot{m} = 15\,\mathrm{kg\,s^{-1}}$. The 397 K is chosen as the temperature to investigate at, since this temperature corresponds to 5% above the final discharge temperature of $378.15\,\mathrm{K} = 105°\mathrm{C}$. As stated in the previous chapters, it takes relatively long time to reach the

final temperature. Therefore the temperature 5% above the final discharge temperature is assessed acceptable as ta final discharge temperature. In the following the temperature of the last HTF element is compared for the three mass flow rates.

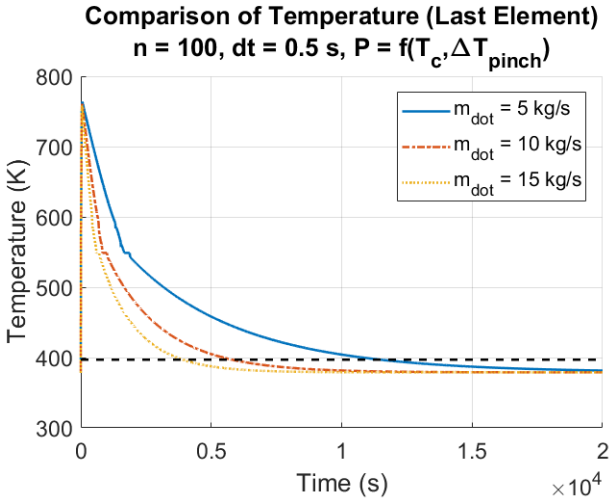

Figure 14.1. Temperature results for discharge (same temperature).

The horisontal black line indicates the temperature of 397 K = 123.85°C. When comparing the three mass flow rates, it is seen that the mass flow rate of $\dot{m} = 15\,\mathrm{kg\,s^{-1}}$ reaches the chosen temperature after 3900 s corresponding to ~ 1.1 h, the mass flow rate of $\dot{m} = 10\,\mathrm{kg\,s^{-1}}$ reaches the 397 K = 123.85°C after 5791 s corresponding to ~ 1.6 h and the mass flow rate of $\dot{m} = 5\,\mathrm{kg\,s^{-1}}$ reaches the 397 K = 123.85°C after 11 460 s corresponding to ~ 3.2 h. This is assessed reasonable, as the highest mass flow rate discharges the TES system the fastest. In the following figure, the ranges of the pressure decreases are investigated.

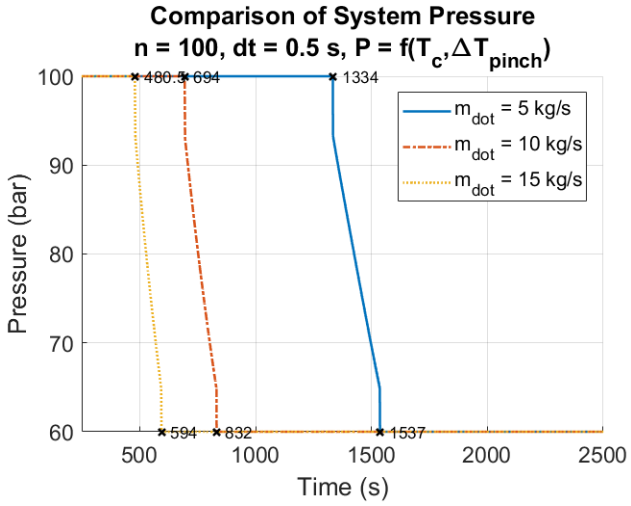

Figure 14.2. Pressure results for each mass flow rate.

From Figure 14.2 it is seen that the pressure decreases over $1537 - 1334 = 203$ s for the mass flow rate of $\dot{m} = 5\,\mathrm{kg\,s^{-1}}$, while the pressure decreases over $832 - 694 = 138$ s for the mass flow rate of $\dot{m} = 10\,\mathrm{kg\,s^{-1}}$, and finally the pressure decreases over $594 - 480.5 = 113.5$ s for the mass flow rate of $\dot{m} = 15\,\mathrm{kg\,s^{-1}}$. This means that the highest mass flow rate corresponds to the fastest decrease. In the following, the accumulated steam is investigated for the three mass flow rates.

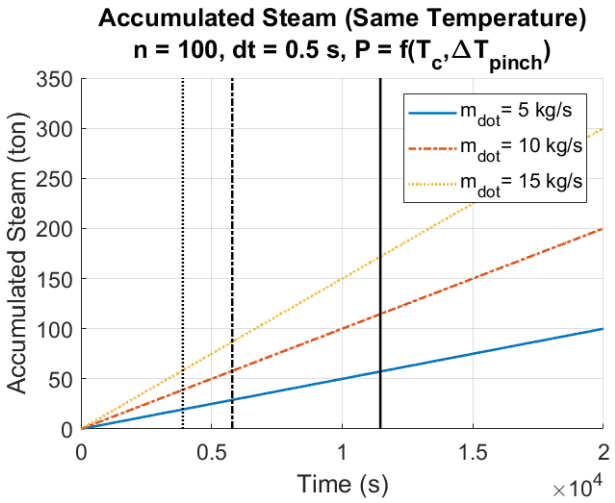

Figure 14.3. Accumulated steam results for each mass flow rate (same temperature).

As stated above, Figure 14.3 shows that different discharge times are needed in order to reach the same discharge temperature of 397 K. This results in the amount of steam accumulated varying as well for the three mass flow rates. It is found that the mass flow rate of $\dot{m} = 5\,\mathrm{kg\,s^{-1}}$ accumulates the least steam, while the mass flow rate of $\dot{m} = 15\,\mathrm{kg\,s^{-1}}$ accumulates the most steam. The black lines in Figure 14.3 corresponds to the discharge times, respectively.

Results from the above figures and additional investigations are presented in Table 14.2.

$\dot{m}$, ($\mathrm{kg\,s^{-1}}$)	5	10	15
T, (K)	397	397	397
t, (s)	11460	5791	3900
$P_{decrease}$, (s)	203	138	114
m_{steam}, (kg)	57300	57910	57965
$\sum \dot{Q}$, (MW)	-7.3638·10^4	-7.3642·10^4	-7.3649·10^4
$\dot{W}_{turb}$, (MW)	1.5847·10^4	1.5704·10^4	1.6445·10^4
	(4.95×10^4 MW h)[1]	(2.513×10^4 MW h)	(1.809×10^4 MW h)

Table 14.2. Results for the short-term storage versus Long-term storage investigation: Discharge at same outlet temperature.

In Table 14.2 it is seen that the long-term storage results in the highest pressure decrease time range but the lowest amount of accumulated steam along with the lowest amount of heat transferred, while the short-term storage results in the lowest pressure decrease time range but the highest amount of accumulated steam along with the highest amount of heat transferred. The pressure decrease, accumulated steam and amount of heat transferred for the intermediate-term storage is in-between. The values of the amount of heat transferred and the turbine work produced are total values at the time given. The highest pressure decrease time range is assessed best for the steam turbine placed after the TES system, since the pressure decrease range can affect the performance and lifetime of the turbine. However, if a relatively fast discharge time and a relatively high amount of heat transferred is needed, a compromise must be made between the turbine performance and the discharge time.

[1] 1.5847×10^4 MW · 3.2 h ≈ 4.950×10^4 MW h.

When looking at the work produced by the turbine, $\dot{W}_{turb}$, it is found that the highest mass flow rate produces the most work. However, the lowest mass flow rate does not produce the least work, as expected. This is assumed due to the fluctuating turbine work seen in Figure 12.7 page 69 caused by the use of *refprop*. It would be expected, that the lowest mass flow rate produces the lowest amount of turbine work. This is further investigated in the following section, where scenario 1.b is presented and discussed.

Discharge at Same Time

In this section the discharge of the TES storage is investigated, when discharging to the same end time of $t = 3900\,\text{s}$ ($\sim 1.1\,\text{h}$) for all three mass flow rates investigated. In the following the temperature of the last HTF element is compared for the three mass flow rates.

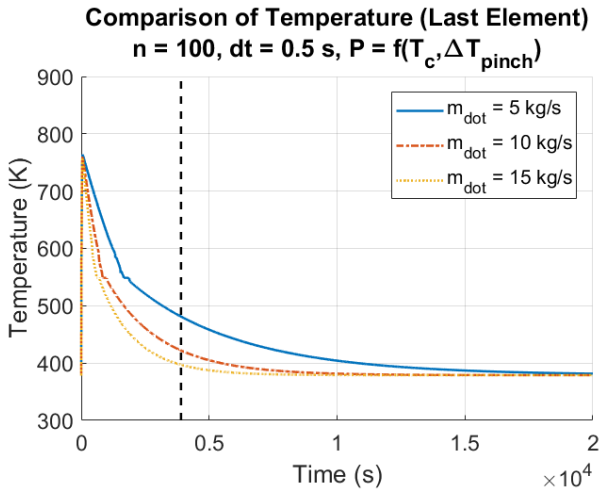

Figure 14.4. Temperature results for discharge (same time).

In Figure 14.4 it is seen that, at the same time, different HTF temperatures exits the TES system. It is found that the highest mass flow rate corresponds to the lowest temperature of $397\,\text{K} = 123.85°\text{C}$, while the lowest mass flow rate corresponds to the highest temperature of $481\,\text{K} = 207.85°\text{C}$. The temperature corresponding to the intermediate mass flow rate is placed in-between ($422\,\text{K} = 148.85°\text{C}$). This is assessed reasonable, since the higher the mass flow rate, the more energy flows through the TES system at the same time. In the following, the accumulated steam is investigated for the three mass flow rates.

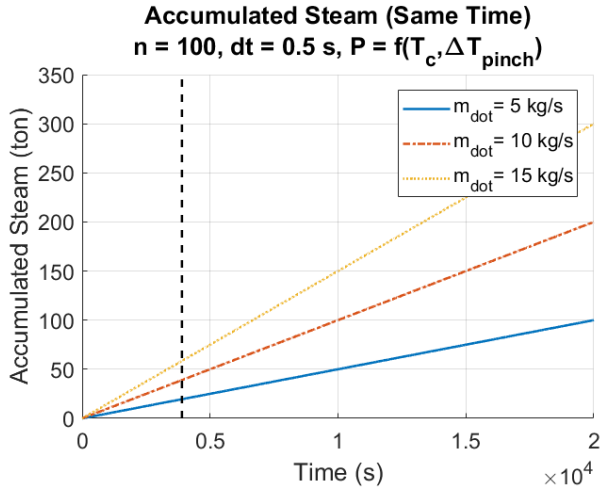

Figure 14.5. Accumulated steam results for each mass flow rate (same time).

In Figure 14.5 it is seen that the highest mass flow rate produces the most steam, as expected, compared to the other two mass flow rates at the same time. The lowest mass flow rate produces the least amount of steam, and the steam production for the intermediate mass flow rate is in-between.

Results from the above figures and additional investigations are presented in Table 14.3.

$\dot{m}$, ($\mathrm{kg\,s^{-1}}$)	5	10	15
T, (K)	481	422	397
t, (s)	3900	3900	3900
$P_{decrease}$, (s)	203	138	114
m_{steam}, (kg)	19500	39000	58500
$\sum \dot{Q}$, (MW)	-5.9133·10^4	-6.9347·10^4	-7.3649·10^4
$\dot{W}_{turb}$, (MW)	1.4191·10^4	1.5263·10^4	1.6445·10^4
	(1.561×10^4 MW h)	(1.679×10^4 MW h)	(1.809×10^4 MW h)

Table 14.3. Results for the short-term storage versus Long-term storage investigation: Discharge at same time.

From the table it is seen that, as for Table 14.2 page 79, the long-term storage results in the highest pressure decrease time range but the lowest amount of accumulated steam along with the lowest amount of heat transferred. Similarly, for the short-term storage and the intermediate-term storage as explained below Table 14.2 page 79. The values of the amount of heat transferred and the turbine work produced are total values at the time given.

As for Table 14.2, the highest pressure decrease time range is assessed best for the steam turbine. In order for the turbine to perform best, a relatively high temperature (corresponding to a low temperature range as input to the turbine) and a relatively high mass flow rate is needed. Therefore a compromise must be made, however now between the turbine performance and the discharge temperature. When looking at the work produced by the turbine, it is found that the highest mass flow rate produces the most work, and the lowest mass flow rate produces the lowest amount of turbine work, as expected.

14.1.2 Normal size storage vs. Double size storage

In this section two TES storage sizes are investigated. The normal size storage has the dimensions of a 2 x 2 x 12 meter concrete block and 25 pipes with a diameter of 0.1 meter, while the double size storage has the dimensions of a 4 x 4 x 24 meter concrete block and 50 pipes with a diameter of 0.1 meter. In this investigation, a mass flow rate of $\dot{m} = 10\,\mathrm{kg\,s^{-1}}$ and an end time of $t = 5791\,\mathrm{s}$ (corresponding to 1.6 h) are used. In the following figure, the temperatures of the last HTF element are compared for the two sizes.

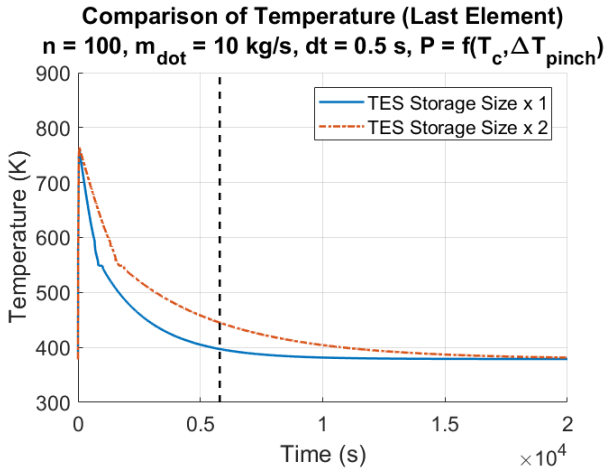

Figure 14.6. Temperature results for different TES system sizes.

In Figure 14.6 it is seen that the temperature of the double size TES system is generally higher than the temperature of the normal size TES system. This is due to the doubled amount of concrete and number of pipes. It is found that the time past before reaching the saturation state increases from 832 s in the normal size TES system to 1664 s in the double size TES system (which is the doubled time). At the time of $t = 5791\,\mathrm{s}$ (indicated by the vertical black line) it is assessed that the normal size TES system is discharged. However, in order for the double size TES system to be discharged to the same temperature, an end time of $t = 11\,460\,\mathrm{s}$ corresponding to half the mass flow rate as investigated in the previous section, is needed. This is slightly less than the time doubled (2.11 % less or 122 s). At the time of $t = 20\,000\,\mathrm{s}$ the temperature difference between the last HTF elements in the two sizes have decreased to 2.6 K (378.9 K = 105.75°C for the normal size TES system and 381.5 K = 108.35°C for the double size TES system). In the following figure, the ranges of the pressure decreases for the two TES systems are seen.

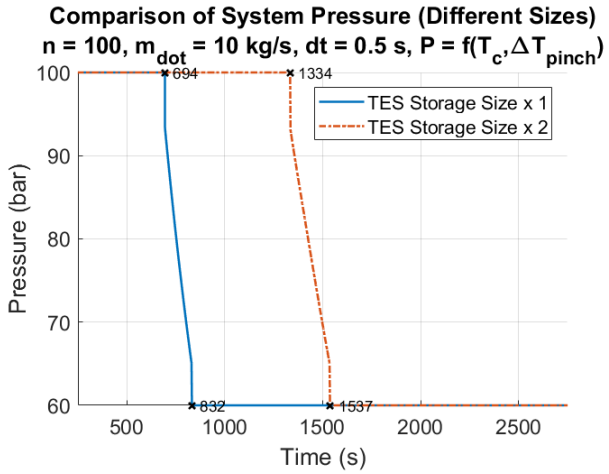

Figure 14.7. Pressure results for different TES system sizes.

From Figure 14.7 it is seen that the pressure decreases over $832 - 694 = 138$ s for the normal size TES system, while the pressure decreases over $1537 - 1334 = 203$ s (corresponding to half the mass flow rate) for the doubled size TES system, as expected.

In Table 14.4 results from the above figures and additional investigations are presented. The material costs seen in the table are calculated in Appendix F.

TES size	x 1	x 2
$\dot{m}$, ($\mathrm{kg\,s^{-1}}$)	10	10
t, (s)	5791	5791
T, (K)	397	445
$P_{decrese}$, (s)	138	203
m_{steam}, (kg)	57910	57910
$\sum \dot{Q}$, (MW)	$-7.3612 \cdot 10^4$	$-1.3072 \cdot 10^5$
$\dot{W}_{turb}$, (MW)	$1.5704 \cdot 10^4$	$2.9969 \cdot 10^4$
	(2.513×10^4 MW h)	(4.795×10^4 MW h)
Material costs, (DKK)	213,000	426,000

Table 14.4. Results for the normal size TES system versus double size TES system investigation.

At the time $t = 5791$ s it is seen that the amount of steam produced from the two TES systems are the same, due to the same mass flow rate. However, the amount of heat transferred from the concrete to the HTF elements is higher in the double size storage due to the higher temperature at this time and the larger TES system. The increase in amount of heat transferred is though not doubled, since the difference between the two amounts is only 77.5%[2] meaning that the doubled size TES system results in 1.775 times the heat transferred compared to the normal size TES system.

The similar is found for the work produced by the turbine, where the difference between the two amounts is 90.4%[3] meaning that the doubled TES system results in 1.908 times the work produced compared to the normal size TES system.

When looking at the time $t = 20\,000$ s the difference between the amounts of heat transferred is found to be 98.8%[4] meaning that almost the doubled heat is transferred for the double size TES system at the end time compared to the normal size TES system.

For the work produced by the turbine the opposite is however found, where the difference between the amounts of work produced has decreased from 90.4% to 88.5%[5] meaning that the doubled TES system, at this time, results in only 1.885 times the work produced compared to the normal size TES system. This is partly due to the different temperature progressions seen in Figure 14.6 page 82, where the temperature slope of the double size TES system is generally smaller than the temperature slope of the normal size TES system. Additionally, the decrease in amount of work produced can be explained by the fluctuating behaviour for the normal size TES system seen in Figure 14.8.

[2]Calculated as: ($-1.3072 \cdot 10^5$ MW - ($-7.3612 \cdot 10^4$ MW)) / $-7.3612 \cdot 10^4$ MW $\cdot$ 100% = 77.5%.
[3]Calculated as: ($2.9969 \cdot 10^4$ MW - $1.5704 \cdot 10^4$ MW) / $1.5704 \cdot 10^4$ MW $\cdot$ 100% = 90.4%.
[4]Calculated as: ($-1.5264 \cdot 10^5$ MW - ($-7.6769 \cdot 10^4$ MW)) / $-7.6769 \cdot 10^4$ MW $\cdot$ 100% = 98.8%.
[5]Calculated as: ($3.2825 \cdot 10^4$ MW - $1.7415 \cdot 10^4$ MW) / $1.7415 \cdot 10^4$ MW $\cdot$ 100% = 88.5%.

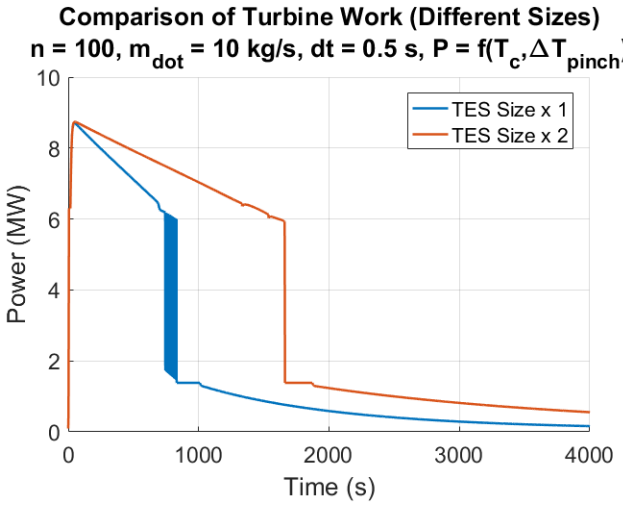

Figure 14.8. Work produced by the turbine for the different TES system sizes.

From Figure 14.8 it is seen that the turbine work for the normal size TES system fluctuates. This is however not visible when observing the double size TES system. As explained earlier, the fluctuations are assumed to be caused by the use of *refprop*.

From the above, it has been found that doubling the TES system size, *i.e.* doubling the material costs, does not correspond to the doubled outcome (1.908 times for $t = 5791\,\mathrm{s}$ and 1.885 times for $t = 20\,000\,\mathrm{s}$ the turbine work). The work produced by the turbine for the normal size TES system however fluctuates as discussed, which is assessed to affect the results. However, discharge of the double size TES system is better related to the performance and lifetime of the following turbine, as discussed in the previous section, since the temperature is generally higher, as seen in Figure 14.6 page 82, and the pressure decrease time range is higher as well.

A compromise must therefore be made between the material costs and the turbine performance regarding what is wanted from the TES system. Finally, it should be noted that buying materials for a larger TES system might not result in the doubled price due to possible quantity discounts of the needed materials. Therefore, the double size TES system could result in a better overall outcome.

15 Discussion

In this chapter different topics of the thesis are discussed. The assumptions made and approached used in the two models (Lumped-Mass-Model and FVM-model) are discussed. Furthermore, the approach for the model coupling, and finally the charge mode of the TES system is briefly discussed.

15.1 Discussion of the Lumped-Mass-Model

In the Lumped-Mass-Model several assumptions are made of which some are more realistic than others. The assumptions are listen in section 10.2 page 41 and discussed in the following.

Assumption 1, regarding the lumped mass approach for the concrete block, is an assumption found to influence the temperature progression in both the concrete block and the HTF elements, since the concrete block in reality has a temperature gradient, and the HTF elements depend on the concrete temperature closest to the pipe, as found in Chapter 12 page 70. This means that, in reality, the temperature difference between the concrete block and the HTF elements would be higher (due to the gradient) resulting in more energy transferred over time, which is not accounted for in the Lumped-Mass-Model. In order words, this means that the Lumped-Mass-Model is discharged faster than the real-life system and would, in reality, store the energy for longer. The influence from the lumped mass approach is further addressed in Chapter 13 page 73, where the assumption, based on the Biot number calculation, is known to be is violated. This is however accounted for by coupling the two models in Chapter 13, where it is found that a temperature gradient throughout the concrete block increases the overall performance of the TES system, since the temperature gradient causes the high-temperature energy to be stored longer in the TES system. The differences between the efficiencies of 100%, 85.92% and 50%, is however relatively small, when comparing the HTF temperatures and the heat transferred, and it is assessed that even though the assumption is violated, the violation does not affect the model results significantly.

Assumption 2, regarding the number of elements, is only valid, when the number of elements is large enough for the temperature within each element to remain constant. In Chapter 10 page 41, 50, 100 and 150 elements are investigated corresponding to element sizes of 24 cm, 12 cm and 8 cm, respectively. If the number of elements used is too small, and the element size is too large, the temperature within each element would increase due to the continuous heat transferred from the concrete block to the HTF elements. This means that the temperature of the HTF elements would both increase and subsequently decrease faster than modelled, resulting in a lower and subsequently higher amount of heat transferred. Since the HTF temperature increase only occurs shortly, the result would in general be a higher amount of heat transferred over time. It is, however, assessed that elements of 12 cm are acceptable for representing the physics of the TES system.

Assumption 3, regarding gathering one centrally placed pipe in the concrete element, which has the same volume as four smaller pipes (as seen in Figure 6.7 page 23), is only valid when considering the volume of the pipes (or the cross-sectional areas). When considering the surface areas of the pipes instead, the assumption is not valid, since the surface area of one gathered pipe only corresponds to the surface area of two small pipes and not all four. Therefore, if this assumption should be more correct, the radius of the one gathered pipe should be doubled for the surface area to correspond to four pipes. A consequence of this assumption is, that the surface area used in the model is half the size of what it should be resulting in a smaller amount of heat transferred than what is occurring in the real TES system.

Assumption 4, regarding the initial conditions of the pipe being water at 105°C, is not correct, since the heat transfer cannot be stopped in time. This means that the pipe in the concrete element will always be filled with steam, which have the same temperature as the concrete, when there is no HTF flowing through. A more realistic assumption would be to assume that the pipe is initially filled with 550°C steam. However, due to *refprop* complications, water at 105°C has been used as initial condition in the Lumped-Mass-Model. This means that, in the modelled TES system, the HTF flow needs to "push out" the initially 105°C water in the pipe, before actually discharging, resulting in the TES system discharge starting too soon. With a mass flow rate of $10\,\mathrm{kg\,s^{-1}}$, corresponding to the fluid flow velocity of $1.27\,\mathrm{m\,s^{-1}}$, it would take the incoming HTF approximately 15 s to "push out" the water in the pipe ($1.27\,\mathrm{m\,s^{-1}} \times 12\,\mathrm{m}$). The heat transferred in these seconds should therefore somehow be "cancelled out" meaning that when the actual discharge begins, *i.e.* when the initial water is "pushed out", the temperature of the concrete block TES system is higher in reality than what is modelled. The time where the HTF and the concrete initially has reached the same temperature is found to be approximately 40 s corresponding to a concrete temperature decrease of $823.15\,\mathrm{K} - 762.40\,\mathrm{K} = 60.75\,\mathrm{K}$. This "temperature loss" could be accounted for by defining a higher initial temperature of the concrete of $823.15\,\mathrm{K} + 60.75\,\mathrm{K} = 883.90\,\mathrm{K}$ resulting in a generally higher amount of heat transferred.

Assumption 5, regarding the overall system pressure being constant and all pressure loss begin neglected, is strictly speaking not valid, since pressure losses throughout the system always will be present. It is however assessed, that the pressure losses are relatively small compared to the overall system pressure. The modelling of the varying system pressure is assessed valid, since it is known that the pressure will decrease over time, if the pinch temperature is kept constant as seen in Figure 15.1 below.

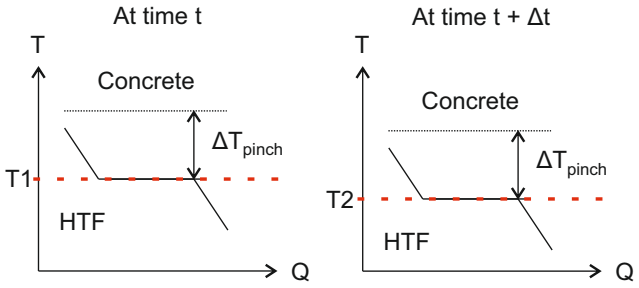

Figure 15.1. System temperature decreasing over time with the system pressure.

From the figure it is seen that, over time, the temperature progressions of the concrete and the HTF elements will decrease, resulting in a pressure decrease as well. It is however assessed that the pressure implementation is valid, since the pressure is defined as a function of the concrete temperature and the pinch temperature.

Assumption 6, regarding the mass flow rate of the HTF being constant, is only valid, if the valves in the TES system, seen in Figure 6.8 page 24, are controlled correspondingly to the system pressure. As the system pressure decreases over time, the mass flow rate would decrease as well. When briefly studying Stodolas equation[1], it is however found that the mass flow rate does not decrease significantly (from $10\,\mathrm{kg\,s^{-1}}$ to $8.13\,\mathrm{kg\,s^{-1}}$ for 100 bar to 60 bar pressure decrease).

Assumption 7, regarding the HTF and concrete densities being constant, is valid for the HTF, since the density is only implemented in the initial conditions, where the HTF always starts out as 105°C water. Within the pipe flow the HTF density will decrease with an increase in temperature, however, for the water inlet the density is constant. For the concrete block, a density value of

[1] $C_T = \dot{m} \cdot \sqrt{\frac{P_1 \cdot v_1}{P_1^2 - P_2^2}}$ [Nielsen, 2014].

$2250\,\mathrm{kg\,m^{-3}}$ is used, which is an experimental value obtained for HT concrete valid for 350°C [Laing et al., 2012]. The density of concrete might, however, not be constant, as it depends on its aggregate materials and the moisture content, which depends on the temperature. This means that in reality the density of the concrete would increase with a decrease in temperature [Naus, 2005], but experimental data would be needed in order to know the actual temperature-dependent density.

Finally, Assumption 8, regarding the TES system being completely isolated, is partly valid, since it corresponds to the TES system being well isolated. This is assessed valid based on the knowledge of the assembly of the TES storage as seen in Figure 6.3 page 22. However, there will always be some kind of energy losses to the surroundings over time but with a well isolated system, these will be rather small compared to the storage capacity of the TES system.

In the Lumped-Mass-Model Euler's method is used to solve the differential equations. This method is known to be the simplest numerical method for solving first order differential equations, and the method requires relatively small steps to achieve an acceptable accuracy, as presented in Appendix D section D.5 page 118. In the figures 10.19 and 10.20 page 52 the accuracy of Euler's method is visible, since the larger time step results in fluctuating temperature values. Therefore, time steps of dt = 0.5 have been used in the Lumped-Mass-Model for which the error is assessed acceptable. Euler's method is a first order method meaning that when reducing the step size, the error is reduced the same. If a large time step is needed, *e.g.* if the computational time of the model is too long, a more accurate numerical method, such as Heun's method, which is a second order method (*i.e.* the error is halved with the step size), or the Runge-Kutta method, which is a fourth order method (*i.e.* the error is four times smaller with the step size), could be used instead.

15.2 Discussion of the FVM-Model

Also in the FVM-Model several assumptions are made of which some are more realistic than others. The assumptions are listed in section 11.2 page 55 and discussed in the following.

Assumption 1, regarding the TES system being modelled as a 2D unsteady heat conduction problem, is valid for the simplified system presented in section 11.3 page 55, where the TES system is viewed from the x, y-direction. In the model the HTF temperature is constant, and the pipe thickness is neglected. These assumptions are discussed in later paragraphs. However, if the TES system like the one considered in the Lumped-Mass-Model is considered, a third direction (the z-direction) should be taken into account, and in this case the 2D unsteady heat conduction problem would not be valid, and a 3D approach would be needed instead.

Assumption 2 and 3, regarding the TES system and the HTF pipe being quadratic in the x, y-direction is only valid for the simplification made in section 11.3 page 55, as the real TES system consists of circular pipes and not quadratic pipes. However, in order to simplify the FVM-Model this assumption is assessed valid, since it requires rather complex calculations to model the concrete block and centred pipe as circles, *e.g.* when converting from Cartesian coordinates to polar coordinates etc. Additionally, it is known from general FVM-modelling, that in most cases a geometry can be approximated with squares, if the squares are placed strategically and are small enough. If the modelled TES system should be closer to the real TES system, the circular shapes could be modelled with squares approximating circles without extensive further calculations. The circular pipe could *e.g.* be approximated by reducing the number of pipes in the cells from 64 to 52 by removing 3 cells around each corner, thereby representing the circular pipe as a "toothed" square. The above is illustrated in Figure 15.2 below, where the pipe is seen in dark blue, and parts of the concrete is seen in grey. The similar could be made for the circular concrete element.

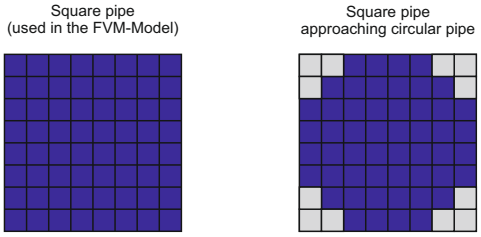

Figure 15.2. Squares approximating a circular pipe for the FVM-Model.

Assumption 4, regarding gathering one centrally water pipe in the concrete element, which has the same volume as four smaller pipes (as seen in Figure 6.7 page 23), is only valid when considering the volume of the pipes (or the cross-sectional areas) as discussed in the Lumped-Mass-Model Assumption 4.

Assumption 5, regarding no heat flux across the outer boundaries of the total control volume, is only valid when investigating a single concrete element, where the surroundings are not considered. When several concrete elements, next to each other, are investigated, these will transfer energy across the boundaries and a heat flux between them will be present. Therefore, this assumption is not completely valid, since the TES system presented in Figure 6.6 page 23 have 25 concrete elements next to each other, which in reality have a heat flux between the boundaries.

Assumption 6, regarding no thermal contact resistance between the concrete and pipe, is only valid for the ideal case, where there is no slip between the two surfaces. In reality, there will be a slip resulting in thermal contact resistance, which will induce a temperature decrease between the surfaces of the concrete and the pipe. However, in the FVM-Model these slips are assumed sufficiently small and therefore insignificant.

Assumption 7, regarding neglecting the thickness of the pipe, is only partly valid, since the thickness of the pipe, if significantly large enough, will affect the heat transfer rate between the concrete and pipe. However, if the thickness of the pipe is sufficiently small, compared to the size of the TES system and the heat transfer through the concrete and the pipe, the influence from the pipe thickness will be rather small. Therefore, the assumption is assessed acceptable.

Assumption 8, regarding the thermal conductivity and specific heat capacity being an average based on linear functions depending on the temperature throughout the concrete block, can be considered partly valid, since the expressions for the functions are based on experiments, as explained in section 6.1.1 page 22. However, an average is used, which might not represent the correct values at all temperatures, since the functions are temperature dependent. Nevertheless, this assumption is made in order to simplify the calculation time and general complexity of the model.

Assumption 9, regarding the HTF temperature to be constant in the considered concrete "slice", is only valid for the inlet "slice", which is the one considered in the FVM-Model. If other "slices", along the z-direction of the TES system, were to be considered, the temperature of the HTF must change with time, since the HTF is not constant over time in the z-direction of the TES system, as modelled in the Lumped-Mass-Model.

Assumption 10, regarding the lengths and widths of the control volumes to be constant and identical throughout the concrete block, is valid, since this is how the FVM-Model is defined based on general FVM-modelling knowledge.

Assumption 11, regarding the geometry being valid to represent the entire cross section of the concrete block, is valid for the simplified system, where the concrete block and pipe can be considered as quadratics in the x, y-direction. If the simplified system was not considered, the cross section of the concrete block would not be valid, as the concrete elements and pipes would

be circular and have air space between the concrete elements, as seen in Figure 6.5 page 23, which would need further investigation.

Finally, Assumption 12, regarding the TES system being completely isolated, is assessed valid, as discussed for Assumption 8 in the Lumped-Mass-Model.

For the FVM-Model a grid independence study is conducted to find a sufficiently accurate solution. In the study the cell (control volume) size is varied, and a vector of temperatures is extracted and compared. The FVM-Model is originally simulated with 1024 cells, and in the grid independence study the model is simulated with 256 and 4096 cells as well. The extracted vectors of temperatures are compared, and the results show that the temperature in the simulation with 256 cells varies between 0.8% and 7.5% corresponding to approximately 4 K and 40 K compared to the simulation with 1024 cells. Similarly, the simulation with 4096 cells varies between 0.2% and 3% corresponding to approximately 2 K and 20 K. The latter variations are rather large, however, the simulation with 4096 cells varies the least compared to the simulation with 1024 cells. In the FVM-Model, the small variation is assessed acceptable, since the deviation of the temperatures has become smaller, and the simulation time is more acceptable. The simulation with 4096 cells, which might be considered the most accurate, requires the longest simulation time of 1.5 h, while the simulation with 1024 cells only requires 2.5 minutes of simulation. When considering both the deviation and the simulation time, the simulation with 1024 cells seems sufficient.

15.3 Discussion of the Model Coupling

In Chapter 13 page 73 the coupling of the Lumped-Mass-Model and the FVM-Model is presented, and results are given. The results show that when combining the two models with an efficiency of 85.92% and 50%, respectively, the temperature peak occurs earlier in time compared with an efficiency of 100%. Furthermore, the temperature after 20 000 s is slightly higher in the coupled models with efficiencies lower than 100%. This is discussed in section 13.2 page 73. The approach for coupling the two models is based on an analogy from fin efficiencies as presented in Chapter 9 page 37. However, this approach might not be completely correct, since the coupling simply reduces to an efficiency calculated in the FVM-Model added to the Lumped-Mass-Model, when considering the concrete block as the fin and the fin base as the pipe wall. Another approach might give more accurate results. An approach could be to merge the two models into one model, where the differential equations solved in the Lumped-Mass-Model are solved for each control volume in the FVM-Model. However, this model approach could be rather comprehensive and would need more time and further understanding of the TES system.

15.4 Discussion of the Charge Mode of the TES System

In this thesis, the discharge mode of the developed TES system is modelled and analysed. Additionally, the charge mode of the same TES system could be interesting to model and analyse as well. The process would be expected to occur opposite with the HTF would entering the TES system as 550°C steam transferring energy to the concrete. The concrete would then be heated up concurrently as the energy is stored. At first it would be expected, that the progression of the temperatures of the concrete and HTF, respectively, would be opposite of those analysed in Chapter 12. However, other parameters might be needed accounted for, when charging the TES system instead of discharging it.

When changing only the initial temperature values from discharge to charge (*i.e.* $T_{con} = 105°C$ and $T_{wat} = 550°C$), with no other model engagement, the following results are obtained from the Lumped-Mass-Model.

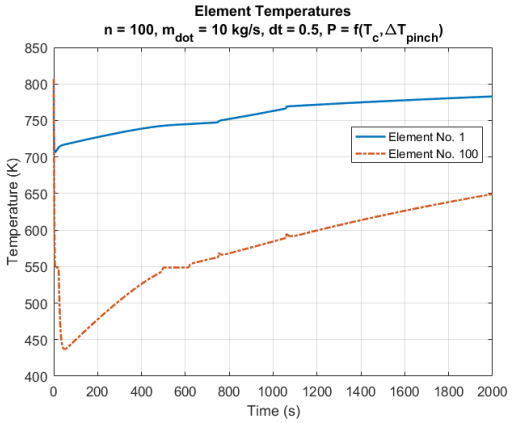

Figure 15.3. Temperature results of HTF elements in the Lumped-Mass-Model during charge mode.

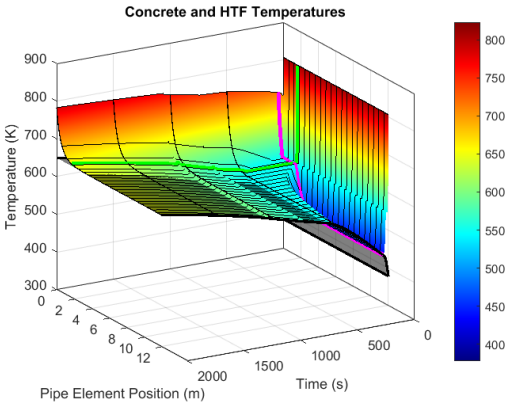

Figure 15.4. 3D temperature results of HTF elements in the Lumped-Mass-Model during charge mode.

From both figures it is seen how that temperature progressions are opposite to those shown in the figures 12.1 page 65 and 12.2 page 66, since the TES system (*i.e.* the concrete), during charge, is heated by the HTF elements. The exact same tendencies are found as explained for the figures 12.1 and 12.2, however opposite as expected.

When correspondingly changing the initial temperature values in FVM-Model the following results are obtained.

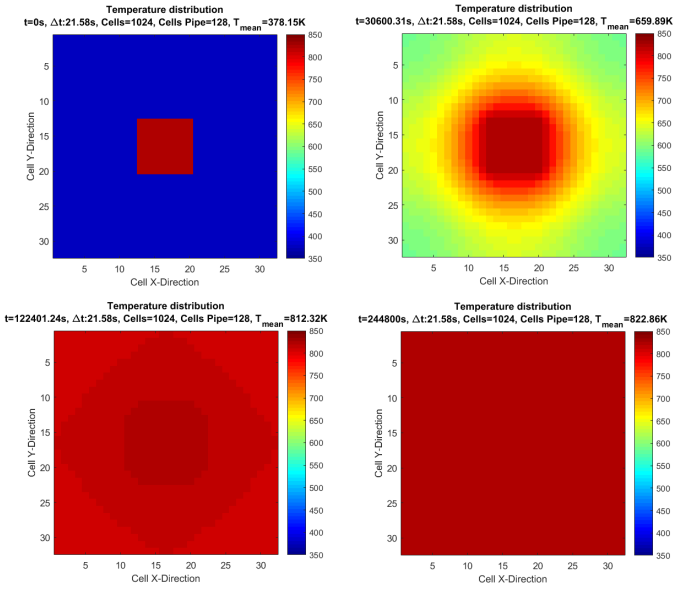

Figure 15.5. Temperature results of the concrete in the FVM-Model during charge mode.

From the figures, it is seen how the HTF enters the TES system with a temperature of 550°C, while the concrete temperature initially is 105°C. As expected, also in this model, the concrete is heated over time, until it reaches the same temperature as the HTF. From the above results the charge mode is, at first glance, assessed to be the opposite of the discharge mode, as expected. However, with a more detailed analyse of charge mode, there might appear parameters, which need further investigation and modelling. It is thereby assessed, that the two developed models simulate the charge/discharge correctly for the simplified TES system with the applied assumptions presented in section 10.2 page 41 and section 11.2 page 55.

Part V

Project Closure

16 Conclusion

This Master's thesis has concerned the design, modelling and analysis of a sensible and passive thermal energy storage (TES) system using a high-temperature concrete mixture (Heatcrete®) as storage material and water/steam as heat transfer fluid (HTF). In the thesis, the discharge process of the TES system has been investigated with focus on the processes in the economiser, evaporator and superheater parts of the TES system, and the output of the TES system has been coupled to a simple power plant turbine.

The TES system developed is inspired by the TES system under development by Aalborg CSP and EnergyNest, and a simplified TES system has been modelled using two different dynamic modelling approaches. The model simplifications have concerned the number and location of the concrete elements within the TES system module (Figure 6.5 page 23) along with the number, size and geometry of the pipes in the concrete elements (Figure 6.7 page 23 and Figure 11.1 page 56).

Firstly, in Chapter 10, the TES system has been modelled as a lumped mass system, in the y, z-plane, consisting of a lumped concrete block with 25 concrete elements each with a single centred pipe. This model has resulted in temperature progressions for the concrete and HTF elements along with the system pressure progression, and the turbine work produced over time. The concrete block initially starts with a temperature of $T_{con} = 823.15\,\mathrm{K} = 550°\mathrm{C}$, while the HTF starts as liquid water with a temperature of $T_{HTF} = 378.15\,\mathrm{K} = 105°\mathrm{C}$ at a pressure of 100 bar.

From the Lumped-Mass-Model results, presented in section 12.1, it is concluded that the concrete temperature decreases over time, as expected, since the TES storage is discharged. The HTF element temperatures first increase, due to the assumption of initial water in the pipe and the heat transferred from the concrete in that period, and later decrease as a result of the decreasing concrete temperature, while the TES system is discharging. After approximately 10 000 s, corresponding to a discharge time of 2.78 h, the HTF element temperatures have decrease to the water inlet temperature, since no more energy is left in the concrete block, and the temperature difference between the concrete and HTF elements is close to zero. As the temperatures, the system pressure and turbine work produced are also concluded to decrease over time. The system pressure decreases from 100 bar to 60 bar, which is defined as the upper and lower pressure limits, respectively, for the TES system. The turbine work is concluded to decrease from approximately 9 MW to approximately 1.23 MW, when the TES storage has been discharged after approximately 900 s (15 min). Hereafter, the HTF elements change phase from steam to water, and another turbine or discharge strategy should be implemented to make use of the remaining stored energy.

Additionally, in Chapter 11, the TES system has been modelled as finite volumes, in the x, y-plane, in order to study the temperature gradient throughout the concrete block in a single concrete element. Besides a temperature gradient over time, the model has resulted in an average efficiency of the concrete block related to the temperature gradient with the temperature closest to the pipe wall defined as 100% (corresponding to a lumped mass). In the model only an inlet "slice" with a constant water temperature of $T_{wat} = 378.15\,\mathrm{K} = 105°\mathrm{C}$ is considered.

From the FVM-Model results, presented in section 12.2, it is concluded that the concrete experiences a decreasing temperature gradient from the outer concrete boundaries towards the centred pipe. It is concluded that after approximately 122 400 s, corresponding to 34 h, the temperature of the concrete block has decreased from $823.15\,\mathrm{K} = 550°\mathrm{C}$ to a mean temperature of $388.98\,\mathrm{K} = 115.83°\mathrm{C}$ (approximately 10 K above the water inlet temperature), and it is found that additionally 34 h are needed to further decrease the concrete temperature until the water

inlet temperature is reached. It is therefore concluded, that the TES system, according to the FVM modelling, can be assessed discharged after 34 h. The average efficiency of the FVM-Model is concluded to be 85.92%, where the control volumes closest to the pipe are discharged first, hereafter the following control volumes are discharged over time.

In Chapter 13 the two developed models are coupled in order to study the influence on the discharge results of the temperature gradient, found in the FVM-Model, on the results from the Lumped-Mass-Model. Results from efficiencies of 100% (*i.e.* the lumped mass), 85.92% (found in the FVM-Model) and 50% are compared. The efficiencies are implemented in the calculation of the heat transfer rate, following the fin efficiency analogy presented in Chapter 9. From the coupling results, it is concluded that for a lower efficiency the temperature gradient in general causes the HTF element temperatures to peak lower, however later in time, resulting in generally higher temperatures when looking at the same discharge times. This is due to the concrete block, with the temperature gradient, storing high-temperature energy furthest from the HTF flow longer, compared to the lumped mass, which changes temperature uniformly at every time step. For the heat transferred an opposite trend is found, since the heat transfer peaks occur earlier in time, and the implemented efficiencies result in generally less heat transferred. From the coupling results, it can therefore be concluded that the implementation of a temperature gradient decreases the heat transfer rate from the concrete to the HTF elements over time, since the slightly higher temperatures do not compensate for the efficiency value implemented. It is however concluded, that the implemented efficiencies do not affect the results significantly.

In Chapter 14 several discharge scenarios for the TES system are investigated and analysed: A short-term TES system is compared to a long-term TES system at the same discharge temperature and time, and a normal size TES system is compared to double size TES system according to discharge output and material costs. From the analysis, it is concluded that when discharging to the same temperature, the TES system outputs ($\sum \dot{Q}$ and $\dot{W}_{turb}$) only vary slightly, but the discharge time is longer at lower mass flow rate. However, when discharging to the same time, it is concluded that the short-term TES system (with the highest mass flow rate) has the highest output values. A compromise should therefore be made between the turbine performance and the discharge rate, since the short-term TES system also results in the lowest time range for the pressure decrease. When comparing the two different TES system sizes, it is concluded that the double size TES system has a doubled pressure decrease time range along with an almost doubled amount of heat transferred, however a compromise should be made between the material costs, which are also doubled, the turbine performance and the discharge time.

Finally, it is concluded that the problem statement, presented in section 5.1 page 17, has been fulfilled. Two dynamic models have been developed and analysed, a lumped mass model and a FVM model, along with a model coupling approach with an analogy drawn to the fin efficiency theory. Additionally, several discharge scenarios for the TES system have been investigated.

17 Future Work

This chapter presents future work ideas for the topic of HT-concrete TES systems, which could be implemented in order to extend and improve the findings of this Master's thesis.

In the thesis, the discharge mode of a HT-concrete TES system is designed, modelled and analysed. The charge mode of the TES system is only briefly discussed in Chapter 15, and it could be interesting to further investigate and model the charge mode of the TES system in order to simulate the complete cycle of the TES system.

In the Lumped-Mass-Model, it is assumed that the TES system initially is filled with liquid water at 105°C due to *refprop* issues. It could be interesting to further investigate this issue and model the TES system with steam at 550°C as initial condition instead, which is expected to appear in a real-life TES system.

The simplified TES system, presented in section 6.2 page 23, considers a concrete element consisting of only one centrally placed HTF pipe, which has the same volume as the four smaller pipes in the Aalborg CSP/EnergyNest TES design. It could be interesting to implement the single pipe with the same surface area as the four smaller pipes in stead of the same volume (and cross-sectional area) and compare the results from the different pipe dimensions. Additionally, it could be interesting to replace the one larger pipe with the four smaller pipes in both the Lumped-Mass-Model and the FVM-Model and thereby simulate a TES system, which better resembles the Aalborg CSP/EnergyNest TES design.

In the FVM-Model, the concrete element is simplified to a square pipe. It could however be interesting to further investigate this geometry and how it influences the temperature gradient throughout the concrete block. Instead of a square pipe, the concrete element could be modified to approximate a circular pipe, as illustrated in Figure 15.2 page 15.2, with a high enough resolution to approximate a fully circular pipe. Additionally, dimensions in polar coordinates could be implemented and compared to the results from the Cartesian coordinate approach.

Furthermore, it could be interesting to expand the FVM-Model to model the TES system in the z-direction, since the FVM-model only considers the inlet position of the TES system corresponding to $z = 0$. It would then be possible to model and analyse the temperature progression of the HTF, as done in the Lumped-Mass-Model, instead of assuming a constant HTF temperature.

Bibliography

Aalborg CSP, **2017a**. Aalborg CSP. *About Us.* Webpage, 2017. URL `http://www.aalborgcsp.com/about/about-us/`. Last seen 28.02.17.

Aalborg CSP, **2017b**. Aalborg CSP. *Thermal Energy Storage (TES).* Webpage, 2017. URL `http://www.aalborgcsp.com/business-areas/thermal-energy-storage-tes/high-temperature-steam-storage/`. Last seen 28.02.17.

Bai and Xu, **2011**. Fengwu Bai and Chao Xu. *Performance analysis of a two-stage thermal energy storage system using concrete and steam accumulator.* Applied Thermal Engineering, 31, 2764–2771, 2011.

Bayon et al., **2010**. Rocio Bayon et al. *Analysis of the experimental behaviour of a 100 kW th latent heat storage system for direct steam generation in solar thermal power plants.* Applied Thermal Engineering, 30, 2643–2651, 2010. Co-authors: Esther Rojas, Loreto Valenzuela, Eduardo Zarza and Javier Leon.

Bergan and Greiner, **2014**. Paal G. Bergan and Christopher J. Greiner. *A new type of large scale thermal energy storage.* Energy Procedia, 58, 152–159, 2014.

BINE, **2017**. BINE. *Energy research for applications - Latent heat storage in buildings.* Webpage, 2017. URL `http://www.bine.info/en/publications/publikation/latentwaermespeicher-in-gebaeuden/`. Last seen 02.04.2017.

Cengel et al., **2012**. Yunus A. Cengel et al. *Fundamentals of Thermal-Fluid Sciences.* McGraw Hill, 4th edition, 2012. Co-authors: John M. Cimbala and Robert H. Turner.

Christansen, **2017**. *Thomas Christansen*, 2017. Victor A/S. Personal communication.

Collier, **1981**. John Gordon Collier. *Convective Boiling and Condensation.* McGraw Hill, 2nd edition, 1981.

Condra, **2017**. *Thomas Condra*, 2017. Personal communication.

Crowe, **2006**. Clayton T. Crowe. *Multiphase Flow Handbook.* Taylor and Francis Group, 2006.

Dincer and Rosen, **2011**. Ibrahim Dincer and Marc A. Rosen. *Thermal Energy Storage - System and Applications.* John Wiley and Sons, Ltd., second edition, 2011.

electrical4u.com, **2017**. electrical4u.com. *Economiser in Thermal Power Plant.* Webpage, 2017. URL `https://www.electrical4u.com/economiser-in-thermal-power-plant-economiser/`. Last seen 30.5.17.

EnergyNest, **2017**. EnergyNest. *Our Technology.* Webpage, 2017. URL `http://www.energy-nest.com/technology/`. Last seen 5.4.17.

Engineers Edge, **2017**. Engineers Edge. *Mechanics of Materials - Pressure Vessel Design and Calculators.* Webpage, 2017. URL `http://www.engineersedge.com/material_science/hoop-stress.htm`. Last seen 22.05.17.

Gabbrielli and Zamparelli, **2009**. R. Gabbrielli and C. Zamparelli. *Optimal Design of a Molten Salt Thermal Storage Tank for Parabolic Trough Solar Power Plants.* Journal of Solar Energy Engineering, 131, 041001–1 – 041001–10, 2009.

Gil et al., 2009. Antoni Gil et al. *State of the art on high temperature thermal energy storage for power generation. Part 1 - Concepts, materials and modellization.* Renewable and Sustainable Energy Reviews, 14, 31–55, 2009. Co-authors: Marc Medrano, Ingrid Martorell, Ana Lazaro, Pablo Dolado, Belen Zalba and Luisa F. Cabeza.

Greiner, 2014. Christopher J. Greiner. *Balancing Supply and Demand with Thermal Energy Storage.* PDF, 2014. Senior Engineer and Project Manager at EnergyNest.

Herrmann and Kearney, 2002. Ulf Herrmann and David W. Kearney. *Survey of Thermal Energy Storage for Parabolic Trough Power Plants.* Journal of Solar Energy Engineering, 124, 145–152, 2002.

Hewitt, 2011. Geoffrey F. Hewitt. *Multiphase Flow.* Web-page, 2011. URL `http://www.thermopedia.com/content/4`. Last seen 30.5.17.

Hoivik, 2016. Nils Hoivik. *Thermal Energy Storage - Technology and Masdar Pilot performance.* PowerPoint (PDF), 2016.

Nils Hoivik et al. Demonstration of EnergyNest Thermal Energy Storage (TES) Technology. Co-authors: Christopher Greiner, Eva Bellido, Juan Barragan, Paal Bergan, Geir Skeie, Pablo Blanco and Nicolas Calvet. Unpublished, 2016.

IAGT, 2009. IAGT. *Industrial Application of Gas Turbines.* PowerPoint (PDF), 2009. Industrial Application of Gas Turbines Committee.

Jensen, 2017. *Peter Badstrue Jensen*, 2017. Aalborg CSP. Personal communication.

Jerz, 2015. Jaroslav Jerz. *Heat Storage in Future Zero-Energy Buildings.* International Journal of Innovative Research in Science, Engineering and Technology (IJIRSET), 4(8), 6722–6728, 2015. Co-authors: Peter Tobolka, Vaclav Michenka and Tomas Dvorak.

Jian et al., 2015. Y. Jian et al. *Control strategy of the module concrete thermal energy storage for parabolic trough power plants.* Energy Procedia, 69, 891–899, 2015. Co-authors: F. Bai, Q. Falcoz and Z. Wang.

John et al., 2013. Emerson John et al. *Concrete as a thermal energy storage medium for thermocline solar energy storage systems.* Solar Energy, 96, 194–204, 2013. Co-authors: Micah Hale and Panneer Selvam.

Kuravi et al., 2013. Sarada Kuravi et al. *Thermal energy storage technologies and systems for concentrating solar power plants (Review).* Progress in Energy and Combustion Science, 39, 285–319, 2013. Co-authors: Jamie Trahan, D. Yogi Goswami, Muhammad M. Rahman and Elias K. Stefanakos.

Laing et al., 2006. Doerte Laing et al. *Solid media thermal storage for parabolic trough power plants.* Solar Energy, 80, 1283–1289, 2006. Co-authors: Wolf-Dieter Steinmann, Rainer Tamme and Christoph Richter.

Laing et al., 2008. Doerte Laing et al. *Solid Media Thermal Storage Development and Analysis of Modular Storage Operation Concepts for Parabolic Trough Power Plants.* Journal of Solar Energy Engineering, 130, 011006–1 – 011006–5, 2008. Co-authors: Wolf-Dieter Steinmann, Michael Fiss, Rainer Tamme, Thomas Brand and Carsten Bahl.

Laing et al., 2009. Doerte Laing et al. *Test Results of Concrete Thermal Energy Storage for Parabolic Trough Power Plants.* Journal of Solar Energy Engineering, 131, 041007–1 – 041007–6, 2009. Co-authors: Dorothea Lehmann, Michael Fiss and Carsten Bahl.

Laing et al., 2010a. Doerte Laing et al. *Development of a Thermal Energy Storage System for Parabolic Trough Power Plants with Direct Steam Generation.* Journal of Solar Energy Engineering, 132, 021011–1 – 021011–8, 2010. Co-authors: Thomas Bauer, Dorothea Lehmann and Carsten Bahl.

Laing et al., 2010b. Doerte Laing et al. *Thermal energy storage for direct steam generation.* Solar Energy, 85, 627–633, 2010. Co-authors: Carsten Bahl, Thomas Bauer, Dorothea Lehmann and Wolf-Dieter Steinmann.

Laing et al., 2012. Doerte Laing et al. *High-Temperature Solid-Media Thermal Energy Storage for Solar Thermal Power Plants.* Proceedings in the IEEE, 100(2), 516–524, 2012. Co-authors: Carsten Bahl, Thomas Bauer, Michael Fiss, Nils Breidenbach and Matthias Hempel.

Learn Engineering, 2016. Learn Engineering. *Boiler, How it works?* Youtube video, 2016. https://www.youtube.com/watch?v=nL-J5tT1E1k. Last seen 30.5.17.

Lele, 2017. Satish Lele. *Two Phase Flow.* Web-page, 2017. URL `http://www.svlele.com/piping/two_phase_flow.htm`. Last seen 6.5.17.

Lund and Condra, 2014. Erik Lund and Thomas Condra. *Notes and Exercises for Numerical Methods.* PDF, 2014.

Martins et al., 2015. Matthieu Martins et al. *New concentrating solar power facility for testing high temperature concrete thermal energy storage.* Energy Procedia, 75, 2144–2149, 2015. Co-authors: Uver Villalobos, Thomas Delclos, Peter Armstrong, Paal G. Bergan and Nicolas Calvet.

McGhie, 2016. Steffen McGhie. *Nyt energilager skal opsamle grøn energi i varme sten.* Webpage, 2016. URL `https://ing.dk/artikel/nyt-energilager-skal-opsamle-groen-energi-varme-sten-189135`. DTU project. Last seen 30.5.17.

Medrano et al., 2009. Marc Medrano et al. *State of the art on high temperature thermal energy storage for power generation. Part 2 - Case studies.* Renewable and Sustainable Energy Reviews, 14, 56–72, 2009. Co-authors: Antoni Gil, Ingrid Martorell, Xavi Potau and Luisa F. Cabeza.

Miro et al., 2014. Laia Miro et al. *Embodied energy in thermal energy storage (TES) systems for high temperature applications.* Applied Energy, 137, 793–799, 2014. Co-authors: Eduard Oro, Dieter Boer and Luisa F. Cabeza.

Naus, 2005. D. J. Naus. *The Effect of Elevated Temperature on Concrete Materials and Structures - A Literature Review*, Oak Ridge National Laboratory, 2005.

Nemgrus, 2017. Nemgrus. *Stoebemix 0/16.* Webpage, 2017. URL `http://www.nemgrus.dk/produkter/st%C3%B8bemix-016/st%C3%B8bemix-016_81`. Last seen 26.5.2017.

Nielsen, 2014. Mads Pagh Nielsen. *Modeling of part-load conditions.* PDF, 2014. Lecture 9 in the course Thermodynamic Systems and Machinery.

Odesie, 2014. Odesie. *HRSG Components.* Webpage, 2014. URL `https://www.myodesie.com/wiki/index/returnEntry/id/2994#HRSGComponents`. Last seen 11.04.2017.

Olesen, 2015. Anders Christian Olesen. *Gas-Luquid, Two-Phase Flow in Pipes.* PowerPoint, 2015. From the course Aerodynamics and Flow (lecture 6 and 7).

Optimera, 2017. Optimera. *Aalborg Portland Basis cement 25 kg.* Webpage, 2017. URL `http://optimera.dk/da-dk/webshop/byggematerialer/murerartikler/cement/25-kg/p-245150125/aalborg-portland-basis-cement-25-kg`. Last seen 26.5.2017.

Powell, 2017. Kody Powell. *Modeling and Optimization of Thermal Energy Storage Systems.* Webpage, 2017. URL `https://kodypowell.che.utah.edu/energy-storage/`. Last seen 02.04.2017.

Salomoni et al., 2014. Valentina A. Salomoni et al. *Thermal storage of sensible heat using concrete modules in solar power plants.* Solar, 103, 303–315, 2014. Co-authors: Carmelo E. Majorana, Giuseppe M. Giannuzzi, Adio Miliozzi, Rosa Di Maggio, Fabrizio Girardi, Domenico Mele and Marco Lucentini.

Shi et al., 2014. Juan Shi et al. *Expersystems and numerical study on effective thermal conductivity of novel form-stable basalt fiber composite concrete with PCMs for thernal storage.* Applied Thermal Engineering, 66, 156–161, 2014. Co-authors: Zhenqian Chen, Shuai Shao and Jiayi Zheng.

Skinner et al., 2014. Joel E. Skinner et al. *Testing of High-Performance Concrete as a Thermal Energy Storage Medium at High Temperatures.* Journal of Solar Energy Engineering, 136, 021004–1 – 021004–6, 2014. Co-authors: Matthew N. Strasser, Brad M. Brown and R. Panneer Selvam.

Steinmann et al., 2009. Wolf-Dieter Steinmann et al. *Development of PCM Storage for Process Heat and Power Generation.* Journal of Solar Energy Engineering, 131, 041009–1 – 041009–4, 2009. Co-authors: Doerte Laing and Rainer Tamme.

Stekli et al., 2013. Joseph Stekli et al. *Technical Challenges and Opportunities for Concentrating Solar Power With Thermal Energy Storage.* Journal of Thermal Science and Engineering Applications, 5, 021011–1 – 021011–12, 2013. Co-authors: Levi Irwin and Ranga Pitchumani.

Teir and Kulla, 2002. Sebastian Teir and Antto Kulla. *Steam-Water Circulation Design.* eBook (PDF), 2002. Helsinki University of Technology Department of Mechanical Engineering, Steam Boiler Technology eBook.

Tian and Zhao, 2012. Y. Tian and C.Y. Zhao. *A review of solar collectors and thermal energy storage in solar thermal applications.* Applied Energy, 104, 538–553, 2012.

VDI Heat Atlas, 2010. VDI Heat Atlas. *VDI Heat Atlas.* Springer, 2nd edition, 2010. Co-editors: Prof. Dr.-Ing. Stephan Kabelac, Prof. Dr.-Ing. Matthias Kind, Prof. Dr.-Ing. Holger Martin, Prof. Dr.-Ing. Dr. H. C. Dieter Mewes and Prof. Dr.-Ing. Karlheinz Schaber.

Versteeg and Malalasekera, 2007. H. K. Versteeg and W. Malalasekera. *An Introduction to Computational Fluid Dynamics - The Finite Volume Method.* Pearson Prentice Hall, 2nd edition, 2007.

Warkhade et al., 2016. Ganesh S. Warkhade et al. *Experimental investigation of sensible thermal energy storage in small sized, different shaped concrete material packed bed.* World Journal of Engineering, 13(5), 386–393, 2016. Co-authors: A. Veeresh Babu, Santosh Mane and Katam Ganesh Babu.

Whalley, 1996. P. B. Whalley. *Two-Phase Flow and Heat Transfer.* Oxford University Press, 1996.

Wittrup, 2014. Sanne Wittrup. *Siemens vil lagre strøm i kæmpe sandbunker.* Webpage, 2014. URL `https://ing.dk/artikel/siemens-vil-lagre-stroem-i-kaempe-sandbunker-172557`. Siemens project. Last seen 30.5.17.

Wittrup, 2016. Sanne Wittrup. *Siemens bygger fuldskala ellager efter dansk ide.* Webpage, 2016. URL `https://ing.dk/artikel/siemens-bygger-fuldskala-ellager-efter-dansk-ide-187203`. Siemens project. Last seen 30.5.17.

Wu et al., 2013. Ming Wu et al. *The impact of concrete structure on the thermal performance of the dual-media thermocline thermal storage tank using concrete as the solid medium.* Applied Energy, 113, 1363–1371, 2013. Co-authors: Mingjia Li, Chao Xu, Yaling He and Wenquan Tao.

Xu et al., 2012. Ben Xu et al. *Extending the validity of lumped capacitance method for large Biot number in thermal storage application.* Solar Energy, 86, 1709–1724, 2012. Co-authors: Pei-Wen Li and Cho Lik Chan.

List of Figures

1 The Aalborg CSP/EnergyNest TES system with 56 concrete elements. iii
2 Simplified TES system with 25 concrete elements. iii
3 3D temperature plot in the Lumped-Mass-Model after 2000 s (33 min). iv
4 Temperature of the FVM-Model after ∼ 61 200 s (17 h). iv

3.1 Overview of the three TES technologies. 7
3.2 Overview of the active and passive TES-systems. 8
3.3 The TES system developed at Aalborg CSP [Jensen, 2017]. 10

6.1 Illustration of the Aalborg CSP/EnergyNest TES system design [Hoivik, 2016]. 21
6.2 Cross-sectional view of a cylindrical concrete element [Hoivik et al., 2016]. 22
6.3 Illustration of the Aalborg CSP/EnergyNest TES system, inspired by [Hoivik et al., 2016]. 22
6.4 Thermal properties for Heatcrete® and DLR-concrete, inspired by [Hoivik, 2016]. . . . 22
6.5 The Aalborg CSP/EnergyNest TES system with 56 concrete elements. 23
6.6 Simplified TES system with 25 concrete elements. 23
6.7 The TES system pipe simplification. 23
6.8 Simplified overview of the processes occurring during discharge. 24
6.9 The ideal Rankine Cycle, inspired by [Cengel et al., 2012]. 25
6.10 Development of the two phases in a water/steam flow, inspired by [Teir and Kulla, 2002]. 27

7.1 Heat transferred through conduction from the concrete to the pipe. 29
7.2 Heat transferred through convection from the pipe to the HTF. 29
7.3 Heat transferred from the concrete to the HTF through the pipe, inspired from [Cengel et al., 2012]. 30
7.4 Parameters and mechanisms involved in lumped system analysis, inspired by [Cengel et al., 2012]. 31

8.1 Grid generation in 2D, inspired by [Versteeg and Malalasekera, 2007]. 33

9.1 Temperature distribution in an ideal (a) and actual (b) fin [Cengel et al., 2012]. 37
9.2 Temperature distribution in the concrete, analogue to the fin efficiency theory. 37

10.1 Simple lumped TES system with a concrete block and one pipe. 41
10.2 Simple lumped TES system divided into elements. 41
10.3 Illustration of ΔT_{pinch} evaluation between the concrete and HTF temperatures. 43
10.4 Pressure implementation in the Lumped-Mass-Model. 43
10.5 Illustration of where the inlet energy are calculated. 44
10.6 Illustration of where the outlet energy are calculated. 44
10.7 HTF element movement in the pipe over time. 46
10.8 Flow diagram showing the set-up of the Lumped-Mass-Model in MATLAB. 47

10.9 Base model result for the first HTF element after 250 s. 48
10.10Base model result for the first five HTF elements after 2000 s. 48
10.11Base model result for the last HTF element after 1000 s. 49
10.12Base model result for 10 HTF elements after 15 000 s. 49
10.133D plot of the concrete and HTF temperatures after 200 s. 49
10.14Temperature results from the base model for comparison. 50
10.15Parameter study result for the number of elements ($n = 50$). 50
10.16Parameter study result for the number of elements ($n = 150$). 50
10.17Parameter study result for the mass flow rate ($\dot{m} = 5\,\mathrm{kg\,s^{-1}}$). 51
10.18Parameter study result for the mass flow rate ($\dot{m} = 15\,\mathrm{kg\,s^{-1}}$). 51
10.19Temperature observations at time step dt = 0.5 s. 52
10.20Temperature observations at time step dt = 1 s. 52
10.21Parameter study result for the pressure ($P = 60\,\mathrm{bar}$). 52
10.22Parameter study result for the pressure ($P = f(T_c, \Delta T_{pinch})$. 52
10.23System pressure decrease in the base model. 53
10.24Energy balance for the base model. 53

11.1 Simplification to square geometry chosen for the FVM-Model. 56
11.2 The geometry of the FVM-Model divided into quadratic control volumes. 56
11.3 Efficiency vectors drawn from the concrete temperature solutions. 58
11.4 Flow diagram showing the set-up for the FVM-Model in MATLAB. 59
11.5 Run 1, Run 2 and Run 3 geometries compared in the FVM-Model. 59
11.6 Illustration of cells in each run, which are compared in the FVM-Model. 60
11.7 Comparison of the first element for Run 1, Run 2 and Run 3. 60
11.8 Comparison of the last element for Run 1, Run 2 and Run 3. 60
11.9 Concrete temperature after $\sim 30\,600$ s (DLR). 61
11.10Concrete temperature after $\sim 30\,600$ s (Heatcrete®). 61
11.11Concrete temperature after $\sim 91\,800$ s (DLR). 61
11.12Concrete temperature after $\sim 91\,800$ s (Heatcrete®). 61
11.13Concrete and HTF temperatures after $\sim 30\,612$ s with same initial conditions. 62
11.14Concrete and HTF temperatures after $\sim 244\,800$ s with same initial conditions. 62

12.1 Temperature of the first and last HTF element after 2000 s. 65
12.2 3D plot of the concrete and HTF temperatures after 2000 s. 66
12.3 Concrete and HTF temperature observations between 670 s and 1020 s. 66
12.4 HTF quality after 2000 s. 67
12.5 Observation of change in element energy, dE_Elem, between 600 s and 1000 s. 67
12.6 Heat transferred from the concrete to the HTF elements after 1200 s. 68
12.7 Turbine work after 5000 s 69
12.8 Last HTF element with highlighted points after 5000 s. 69
12.9 Initial temperatures of the FVM-model. 70
12.10Temperatures of the FVM-Model after $\sim 61\,200$ s. 70
12.11Temperatures of the FVM-model after $\sim 122\,400$ s. 71
12.12Temperatures of the FVM-model after $\sim 244\,800$ s. 71
12.13Temperature gradients throughout the concrete block after after $\sim 244\,800$ s. 71
12.14Mean, maximum and minimum concrete temperatures after $\sim 244\,800$ s. 71

13.1 Temperature results from the Lumped-Mass-Model with an efficiency of 100%. 74
13.2 Temperature results from the Lumped-Mass-Model with an efficiency of 85.92%. 74
13.3 Temperature results from the Lumped-Mass-Model with an efficiency of 50%. 74
13.4 Temperature progressions of the last HTF element at efficiencies of $\eta = 100\%$, $\eta \sim 86\%$ and $\eta = 50\%$. 75
13.5 Heat transfer rate results from the Lumped-Mass-Model with an efficiency of 85.92%. 75

13.6 Heat transfer rate results from the Lumped-Mass-Model with an efficiency of 50%. . . 75
13.7 Lumped mass TES system versus TES system with temperature gradient principle. . . 76

14.1 Temperature results for discharge (same temperature). 78
14.2 Pressure results for each mass flow rate. 78
14.3 Accumulated steam results for each mass flow rate (same temperature). 79
14.4 Temperature results for discharge (same time). 80
14.5 Accumulated steam results for each mass flow rate (same time). 80
14.6 Temperature results for different TES system sizes. 82
14.7 Pressure results for different TES system sizes. 82
14.8 Work produced by the turbine for the different TES system sizes. 84

15.1 System temperature decreasing over time with the system pressure. 86
15.2 Squares approximating a circular pipe for the FVM-Model. 88
15.3 Temperature results of HTF elements in the Lumped-Mass-Model during charge mode. 90
15.4 3D temperature results of HTF elements in the Lumped-Mass-Model during charge mode. 90
15.5 Temperature results of the concrete in the FVM-Model during charge mode. 90

A.1 Example of packed bed sensible heat storage (model), inspired by [Wu et al., 2013]. . . 107
A.2 Example of packed bed sensible heat storage (experiment) from [Warkhade et al., 2016]. 107
A.3 Stratification in a SHS TES system, inspired by [Powell, 2017]. 107
A.4 Temperature profile as a function of amount of heat stored for two different heat storage systems, inspired by [BINE, 2017]. 108
A.5 Principle of thermochemical heat storage, inspired by [Jerz, 2015]. 108
A.6 A direct (upper) and an indirect (lower) TES system, inspired by [Stekli et al., 2013]. 109

B.1 Typical evaporator including the steam drum, the lower drum, several riser tube modules, inspired by [IAGT, 2009]. 111
B.2 Natural circulation principle with ECO-, EVA- and SH-sections, inspired by [Teir and Kulla, 2002]. 111
B.3 Mass quality and void fraction for different pressures, inspired by [Whalley, 1996]. . . 112

C.1 Vertical flow patterns, inspired by [Whalley, 1996]. 113
C.2 Horisontal flow patterns, inspired by [Whalley, 1996]. 113
C.3 The Baker map, inspired by [Whalley, 1996]. 114

D.1 Illustration of Euler's method [Lund and Condra, 2014]. 118

E.1 FVM grid generation in 1D, inspired by [Versteeg and Malalasekera, 2007]. 119
E.2 System of notation in 1D, inspired by [Versteeg and Malalasekera, 2007]. 119

List of Tables

3.1 Advantages and disadvantages of SHS, LHS and TCHS. 8
3.2 Advantages and disadvantages of different types of TES-system. 9

4.1 State-of-the-art between 2006 and 2016. 12

7.1 Applied heat transfer mechanisms during discharge. 29

10.1 The Lumped-Mass-Model input values. 46
10.2 Parameters investigated in the Lumped-Mass-Model. 48

11.1 Input values for the FVM-Model. 58

14.1 The mass flow rates and discharge times for the short-term storage versus long-term storage. 77
14.2 Results for the short-term storage versus Long-term storage investigation: Discharge at same outlet temperature. 79
14.3 Results for the short-term storage versus Long-term storage investigation: Discharge at same time. 81
14.4 Results for the normal size TES system versus double size TES system investigation. . 83

D.1 Euler's method applied. 118

F.1 Overview of estimated material costs for the TES system. 123

Appendix

A Elaboration on TES Technologies and Types

This appendix elaborates the TES technologies, materials and types presented in Chapter 3.

A.1 Sensible Heat Storage (SHS)

As mentioned in section 3.1.1 page 7, the storage material in SHS can be either solid or liquid. Solid materials are typically used in packed beds, which are illustrated in the following figures.

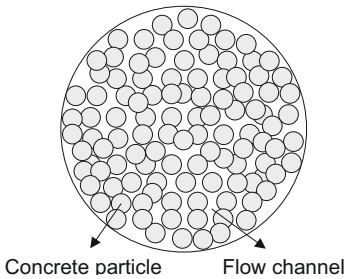

Figure A.1. Example of packed bed sensible heat storage (model), inspired by [Wu et al., 2013].

Figure A.2. Example of packed bed sensible heat storage (experiment) from [Warkhade et al., 2016].

Both figures illustrate concrete particles used as the solid storage material, and it is seen that a fluid is required in the flow channels to exchange the heat. Packed beds favour thermal stratification, where energy stored in the warmer strata easily can be extracted, and fluid from the colder strata can be taken out. If the heat capacity of the fluid is very low, the solid is the only storage material. However, when the fluid is a liquid, its capacity cannot be neglected, and the system is thus a dual storage system. An advantage of this type of system is the lower cost, since inexpensive solids like rock, sand or concrete and be used in conjunction with a more expensive fluid such as thermal oil. A disadvantages is however the possibility of a high pressure loss and thus parasitic energy consumption [Herrmann and Kearney, 2002].

Liquid materials have an advantage of maintaining natural thermal stratification due to the difference in densities in the hot and cold fluids. In order to utilise this advantages, the hot fluid has to be supplied during charging in the upper part of the storage system, whilst the cold fluid has to be extracted during discharge from the bottom part [Herrmann and Kearney, 2002]. This is illustrated in Figure A.3.

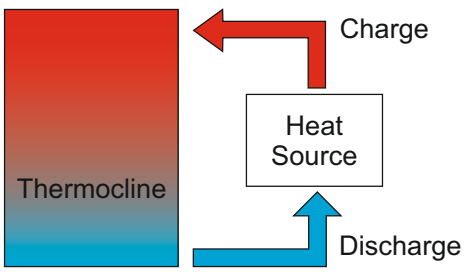

Figure A.3. Stratification in a SHS TES system, inspired by [Powell, 2017].

Figure A.3 illustrates how the hot and cold fluids, top and bottom respectively, are divided by a thermocline and how the storage tank is connected to the heat source. If natural thermal stratification is not established, another mechanism has to be used in order to avoid mixing and make sure the fluid enters the storage at the correct level in accordance with the temperature [Herrmann and Kearney, 2002]. Examples of solid materials are sand-rock materials, reinforced concrete, cast iron. Examples of liquid materials are solar salt, mineral oil, synthetic oil, nitrite salts [Tian and Zhao, 2012].

A.2 Latent Heat Storage (LHS)

LHS systems, presented in section 3.1.2 page 7 has the advantage of storing and releasing the energy nearly isothermally. This makes this technology very favourable in applications, where the working temperatures are very strict [Tian and Zhao, 2012]. This is illustrated in Figure A.4 that compares a combined-sensible-and-latent heat storage system to a sensible heat storage system.

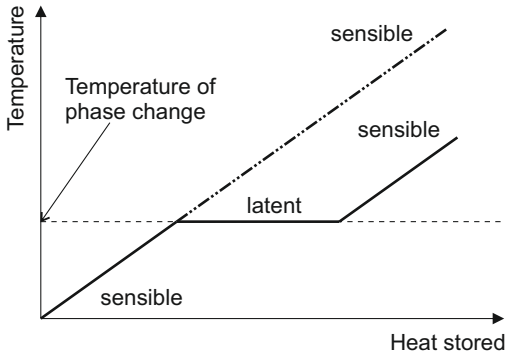

Figure A.4. Temperature profile as a function of amount of heat stored for two different heat storage systems, inspired by [BINE, 2017].

As seen in Figure A.4, latent heat is stored at a constant temperature resulting in an overall smaller temperature difference compared to a storage system using only sensible heat. A disadvantage of LHS systems is the typically low thermal conductivities, which require heat transfer enhancement technologies such as insertion of metal fins or beads or the use of carbon fibres [Tian and Zhao, 2012].

A.3 Thermochemical Heat Storage (TCHS)

The principle of thermochemical heat storage is given in Figure A.5.

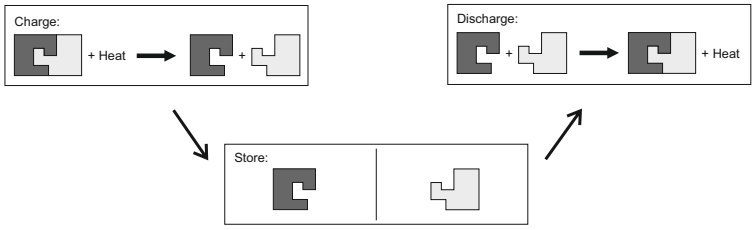

Figure A.5. Principle of thermochemical heat storage, inspired by [Jerz, 2015].

In Figure A.5, the processes of charging, storing and discharging of a thermochemical heat storage are given. Materials that are suited for TCHS, presented in section 3.1.3 page 8, can be organic or inorganic, just as long as their reversible chemical reactions involve absorption and release of heat. There are three main requirements, when designing a thermochemical storage

system: "*excellent chemical reversibility, large chemical enthalpy change and simple reaction conditions*" [Tian and Zhao, 2012]. This type of thermal energy storage is an attractive possibility for the future storages and could offer relatively low costs [Gil et al., 2009]. Advantages of thermochemical storage systems are high storage densities ($GJ\,m^{-3}$) compared to LHS systems ($MJ\,m^{-3}$) and indefinitely long storage duration near ambient temperature. Disadvantages are that thermochemical storage systems are not yet extensively researched, complexity of the technology, uncertainty in the properties of the reaction components and limitation regarding applications [Herrmann and Kearney, 2002].

A.4 Active TES-systems (Direct or Indirect)

In active TES systems, presented in section 3.2.1 page 9, liquids are typically used as storage material, since they have a higher energy density and thermal conductivity compared to gasses. However, the liquid used has to be stable at the operating temperature, which is not always economical. Other cheaper materials, may however not possess the needed high thermal conductivity, which is needed in the discharge process in order to discharge the energy efficiently [Kuravi et al., 2013].

As seen in Figure 3.2 page 8, different types of active systems exist. The first type of active system is a *two-tank system* which can be direct or indirect, and the system uses a liquid storage material such as molten salts or synthetic oils. In 2013 this type of system was the most commercial technology used [Kuravi et al., 2013]. A two-tank TES system for storing energy from a solar field is given in Figure A.6, comparing the direct and indirect TES technologies.

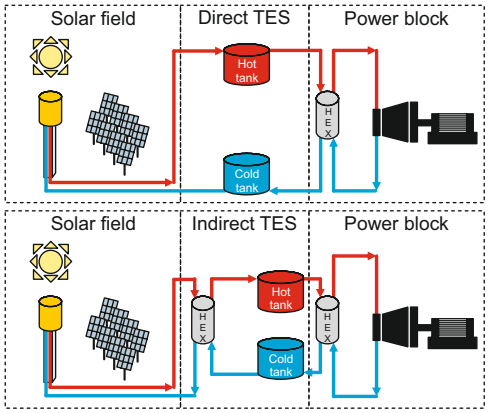

Figure A.6. A direct (upper) and an indirect (lower) TES system, inspired by [Stekli et al., 2013].

From the figure it is seen, that the direct TES system uses the same HTF in the solar field as well as in the TES system, while two different HTFs are used in the indirect TES system. It is seen, that the latter requires an additional heat exchanger in order to exchange heat between the two HTFs [Stekli et al., 2013].

Advantages of this type are that the cold and hot materials are stored separately, it is a low-risk approach, and there is a possibility to raise the output temperature to 450-500°C. Disadvantages are high costs of the HTF, storage material and heat exchangers, the need for two tanks and the temperature difference between the hot and cold fluid, which is relatively small [Gil et al., 2009].

The second type of active system is a *thermocline system*, which is a single tank system, also using liquid as storage material as seen in Figure A.3 page 107. The system is called thermocline because of the thermal gradient, which develops within the system. A downside to this system is the difficulty to separate the hot and cold fluids inside the tank. Therefore, a filler material is sometimes inserted in the system in order to maintain the temperature difference. The filler

material acts as the primary storage material and thus makes the system passive [Kuravi et al., 2013]. Advantages of this type of system are the possibility of reducing the costs, since the hot and cold fluid are in one tank, and low costs of filler materials. Disadvantages are the relatively high freezing points of the molten salts mixtures, the difficulty of separating the hot and cold fluids, losses due to the high outlet temperature, requirements of a controlled charging and discharging procedure, in order to maintain the thermal stratification, and methods or devices to avoid mixing of the fluids and finally the possibility of a more complex system design [Gil et al., 2009].

The third type of active system is *steam accumulators* in which water is used as storage material. Discharging occurs when the pressure of the storage tank decreases, resulting in production of saturated steam with a decreasing pressure. However, if superheated steam is desired as output, another system component is required in order to increase the steam temperature [Kuravi et al., 2013]. An advantage of this system is that it has been widely investigated and used for fossil fuel fired power plants. A disadvantage is that when using a steam accumulator, only saturated steam is obtained, as mentioned earlier. Due to a decrease in pressure and temperature, during discharge, the steam accumulator needs to be designed and operated to meet the turbine cycle needs [Kuravi et al., 2013]. This is further addressed in [Bai and Xu, 2011].

A.5 Passive TES-systems

In passive TES systems, presented in section 3.2.2 page 9, advantages are low costs, high heat transfer rates due to the good contact between the storage material and piping, facility of handling of the material and low degradation of the heat transfer between the heat exchanger and storage material [Gil et al., 2009]. Disadvantages are the costs of the heat exchangers and the possibility of a more problematic and low heat transfer, when the storage material is in solid phase rather than liquid phase.

There are several heat transfer mechanisms such as embedded tubes or pipes and mechanisms using packed bed storages [Kuravi et al., 2013]. Many researchers have studied embedded structures for improving the heat transfer at both low and high temperatures. However, if the material has a high thermal conductivity, they have to be compatible with the storage material and the HTF [Kuravi et al., 2013]. Different approaches have been made such as integrating tubular heat exchangers into the storage material [Laing et al., 2009], placing a horizontal transfer structure of graphite or aluminium between the layers of pre-cast concrete [Laing et al., 2012] and adding fin materials of graphite or aluminium [Steinmann et al., 2009].

In packed bed systems, the HTF transfers heat to the storage material by flowing between different storage material elements of various shapes and sizes. The HTF is in direct contact with the storage material, which makes it possible for the heat transfer coefficients to be large. The thermal gradient can be maintained when materials like rocks, which have a low conductivity, are used. The packed bed systems are typically single tanks systems, which acts like a thermocline. The costs of the systems can be low compared to two-tank systems, since the storage material is solid and only need one tank [Kuravi et al., 2013].

B The Evaporator Parts and Process Explained

This appendix elaborates the working principle of the evaporator and explains the key parameters.

B.1 Drums, Tube Modules and Steam Drum Volume

As mentioned in Chapter 6, an evaporator typically consists of a steam drum and two types of tube modules: risers and downcomers. This is illustrated in the figures B.1 and B.2.

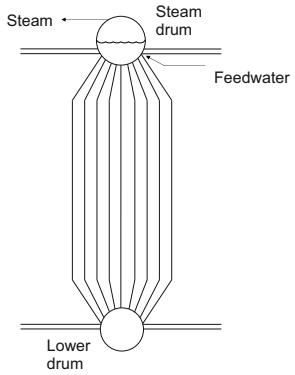

Figure B.1. Typical evaporator including the steam drum, the lower drum, several riser tube modules, inspired by [IAGT, 2009].

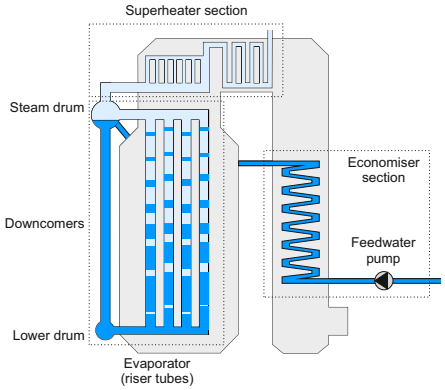

Figure B.2. Natural circulation principle with ECO-, EVA- and SH-sections, inspired by [Teir and Kulla, 2002].

As shown in the figures the water level in the steam drum is approximately 50%, *i.e.* 50% of the drum volume is water, and 50% is steam. Several riser tube modules are seen to combine the two drums. The downcomers are similar tube modules, usually of much larger diameter, placed outermost in the system, *i.e.* outside the boiler, as seen in Figure B.2. This is to prevent the water in the downcomers from evaporating, which would decrease the driving force of the circulation [Teir and Kulla, 2002]. Typically the number of risers to downcomers is approximately 100:1 [Condra, 2017].

When discharging, water enters from the economiser through the steam drum and continues down to the lower drum and further into the evaporator [Teir and Kulla, 2002]. Due to heat applied to the water from the concrete, the water is heated up and rises naturally through the riser tube modules to the steam drum in the top of the evaporator, also seen in the figure. The natural circulation is due to the density differences between the water and steam in the risers and downcomers. In the steam drum water and steam are separated, as steam is diverted to the superheater, while water is led through the downcomer tube modules to the lower drum, maintaining the water level in the steam drum. For the tube modules the following relationship applies: $\Delta P_{\text{riser}} = \Delta P_{\text{downcomer}}$. An ideal downcomer is as short as possible and has a flow velocity as high as possible [Teir and Kulla, 2002].

The volume of the steam drum is typically determined from [Condra, 2017]:

$$V_{\text{steam drum}} = 2 \cdot \frac{\dot{m}}{\rho_{sat.steam} \cdot 10^3} \tag{B.1}$$

where $\dot{m}$ is the mass flow rate in $(\text{kg}\,\text{h}^{-1})$.

B.2 Circulation Number

Related to the drums and tube modules is the circulation number. The circulation number is determined as the ratio between the mass flow rate of water fed to the risers divided by the mass flow rate of the generated steam leaving the steam drum [Teir and Kulla, 2002]:

$$N_c = \frac{\dot{m}_{\text{riser}}}{\dot{m}_{\text{generated steam}}} = \frac{1}{x_{\text{out}}} \tag{B.2}$$

where x_{out} is the evaporator outlet quality of the steam ranging from 0 to 1. For natural circulation, the circulation number varies between 5 and 100 [Teir and Kulla, 2002], and in the industry, a circulation number between 20-40 is typically obtained.

As mentioned in section B.1, the density differences between the water and steam in the risers and downcomers drives the natural circulation, while the driving pressure is defined as [Teir and Kulla, 2002]:

$$\Delta P_{\text{driving}} = g \cdot (H_{\text{evaporator}} - H_{\text{boiling}}) \cdot (\rho_{\text{downcomers}} - \rho_{\text{risers}}) \tag{B.3}$$

where g is the gravitational acceleration, $H_{\text{evaporator}}$ is the height of the evaporator, H_{boiling} is the height where the water has a high enough temperature to boil, called the boiling height, and $\rho_{\text{downcomers}}$ and ρ_{risers} are the average densities in the downcomers and risers, respectively.

B.3 Mass Quality Vs. Void Fraction

In Figure B.3 the mass quality vs. void fraction is illustrated for different pressures.

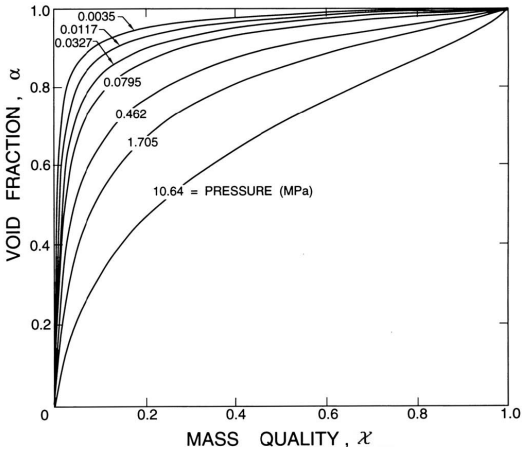

Figure B.3. Mass quality and void fraction for different pressures, inspired by [Whalley, 1996].

From Figure B.3, it is seen that a low mass quality gives a high void fraction. When the pressure is low, the void fraction increases rapidly, when the mass quality is above zero compared to high pressures. This means that low steam pressures result in a high circulation number compared to high steam pressures, as seen in equation (B.2).

C Elaboration on Multiphase Flow

This appendix elaborates the theory behind multiphase flows including the definition, different types of flows and typical flow patterns and maps. Furthermore, two-phase models and the pressure gradient are briefly presented.

A multiphase flow is defined as a flow in which more than one phase occurs, and the phases can be mixed. The most common types of multiphase flows are two-phase flows, which are gas-liquid, gas-solid, liquid-liquid and liquid-solid flows [Hewitt, 2011].

The solid phase in a two-phase flow is typically particles or lumps that are carried along the flow. The movement of the solids strongly depends upon the size of the particles and the motion of the fluids *i.e.* small particles follow the motion of the fluid, and large particles are less responsive. The liquid phase in a two-phase flow can be either continuous or discontinuous. The continuous phase contains dispersed solids in form of particles, gases in the form of bubbles or other liquids in form of drops. The discontinuous phase is in the form of drops suspended in a gas phase or in another liquid phase. The gas phase in a two-phase flow has the same properties as the liquid phase regarding response to forces, but it is highly compressible in comparison to solids and liquids [Hewitt, 2011].

Gas-liquid flows can be bubbles in a liquid or droplets in a conveying gas stream. Gas-liquid flows in pipes can have different configurations like bubbly flow and annular flow. Gas-solid flows are usually gas with suspended solid particles and have the configuration of a granular flow. Liquid-solid flows are when solid particles are being carried by the liquid and typically have the configuration of a slurry flow [Crowe, 2006].

C.1 Flow Patterns and Maps

In multiphase flows the different phases can have various geometric configurations and these configurations are called flow patterns or flow regimes. When determining the flow pattern of a flow, the important parameters are surface tension and gravity. Surface tension keeps the channel wall wet and tends to make liquid drops and gas bubbles spherical, and gravity tends to pull the liquids downwards to the bottom of the channel [Whalley, 1996]. For vertical flows in circular tubes, in which all phases are flowing upwards, the common flow patterns are given in Figure C.1. Similar is shown in Figure C.2 for horisontal flow in circular tubes.

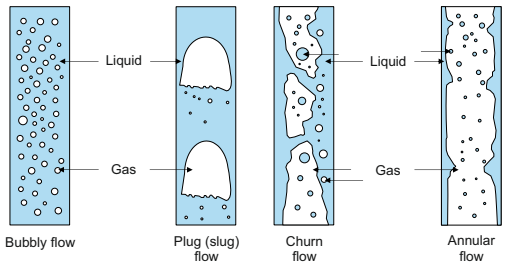

Figure C.1. Vertical flow patterns, inspired by [Whalley, 1996].

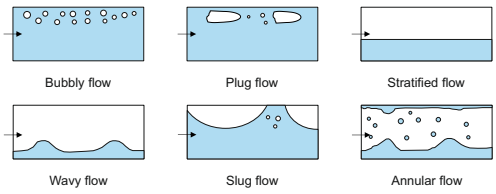

Figure C.2. Horisontal flow patterns, inspired by [Whalley, 1996].

In Figure C.1 four different flow patterns are shown: bubbly flow, plug/slug flow, churn flow and annular flow. In bubbly flow, gas bubbles of approximately uniform size are located in the liquid.

In plug/slug flow, the gas flows as large bullet-shaped bubbles in the liquid, but there are also small gas bubbles distributed in the liquid. In churn flow, the liquid continually pulses up and down near the wall, and this type of flow is highly unstable of an oscillatory nature. The last flow is the annular flow, where the liquid is partly small drops distributed in the gas, which is in the center of the flow, and partly flows as annular film on the walls [Whalley, 1996].

In Figure C.2 six different flow patterns are shown: bubbly flow, plug flow, stratified flow, wavy flow, slug flow and annular flow. In bubbly flow, the gas bubbles, distributed in the liquid, tend to rise to the top of the tube. In plug flow, the individual small gas bubbles has united to produce long plugs distributed in the liquid at the top of the tube. In stratified flow, the interface of the liquid and gas is smooth and this type of flow pattern does not usually occur, since the interface is typically wavy. In wavy flow, the interface of the gas and liquid is wavy, and the amplitude of the waves depend upon the gas velocity; when the gas velocity increases, the wave amplitude increases. In slug flow, the interface of the gas and liquid is also wavy, and the amplitude of the wave is so large, that the wave touches the top of the tube. Finally in annular flow, which is very similar to the one in vertical flow, the liquid is partly drops and partly annular film. The difference from the vertical flow is, that the liquid film is thicker at the bottom of the tube compared to the top of the tube in horisontal flow [Whalley, 1996].

Flow pattern maps are two-dimensional graphs that separates the space into different areas, which correspond to the various flow patterns. An example is the Baker map for horisontal flow, which is given in Figure C.3.

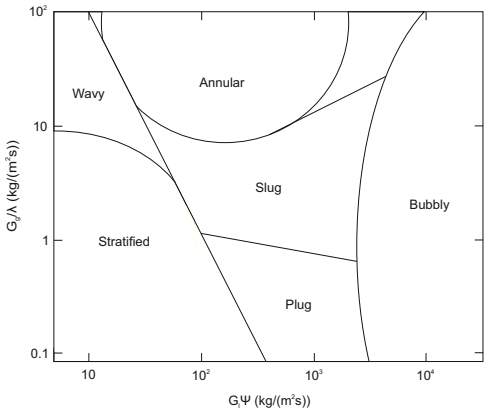

Figure C.3. The Baker map, inspired by [Whalley, 1996].

In Figure C.3 the two-dimensional graph is divided into areas that correspond to the flow patterns given in Figure C.2. The x-axis is $G_l\psi$ and the y-axis is $\frac{G_g}{\lambda}$, where:

$$G_l = \frac{\text{liquid mass flow rate}}{\text{tube cross-sectional area}} \qquad \text{(C.1)} \qquad \psi = \frac{\gamma_{wat}}{\gamma_l}\left(\frac{\mu_l}{\mu_{wat}}\left(\frac{\rho_{wat}}{\rho_l}\right)^2\right)^{1/3} \qquad \text{(C.2)}$$

$$G_g = \frac{\text{gas mass flow rate}}{\text{tube cross-sectional area}} \qquad \text{(C.3)} \qquad \lambda = \left(\frac{\rho_g}{\rho_{air}}\frac{\rho_l}{\rho_{wat}}\right)^{1/2} \qquad \text{(C.4)}$$

where G is the mass flux, ψ and λ are dimensionless factors, γ is the surface tension, μ is the viscosity and ρ is the density. l and g refers to the liquid and gas, respectively [Whalley, 1996]. A map for vertical flows is the Hewitt and Roberts map, which is similar to the Baker map, but with the axes: x-axis $= \frac{G_l^2}{\rho_l}$ and y-axis $= \frac{G_g^2}{\rho_g}$ [Whalley, 1996].

C.2 Models for Two-Phase Flows

When dealing with two-phase flows, several models have been developed for modelling the flows. The different models are [Lele, 2017]:

- *Single Phase Model*: One single steady-state, isothermal phase with constant cross section area.
- *Two-Fluid Model*: Two separated, steady-state, isothermal phases without mass transfer between the fluids. This model can model various flow patterns.
- *Homogeneous Model*: Two phases assumed to flow with the same velocity. The flow is treated as being analogous to a single phase flow, and the no-slip condition between the true phase velocities is applied.
- *Multi-Fluid Model*: Separate conservation equations are written for each phase, and these equations contain terms which describe the interaction between the phases.
- *Drift Flux Model*: The flow is described in terms of a distribution parameter and an averaged local velocity difference between the phases.
- *Lockhart-Martinelli Correlation*: Estimates the two-phase pressure gradient with a two-phase flow multiplier.

C.3 Pressure Gradient

The mass and momentum equation for a single-phase pipe flow is given by [Olesen, 2015]:

$$\text{Mass:} \quad \frac{d}{dz}(\rho u) = \dot{m} = 0 \Rightarrow \rho u = G = const. \tag{C.5}$$

$$\text{Momentum:} \quad \frac{d}{dz}(\rho u u) - \frac{d\tau}{d} = -\frac{dp}{dz} + \rho g \sin(\theta) \tag{C.6}$$

$$\Rightarrow \frac{d}{dz}(\rho u u) = \frac{d}{dz}\left(\rho \frac{GG}{\rho\rho}\right) = G^2 \frac{d}{dz}\left(\frac{1}{\rho}\right) \text{ and } \frac{d\tau}{dz} = \tau_w \frac{P}{A} \tag{C.7}$$

From the above equation the basic pressure gradient is given by [Whalley, 1996]:

$$\underbrace{-\frac{dp}{dz}}_{\text{Total pressure gradient}} = \underbrace{\tau_w \frac{P}{A}}_{\text{Frictional}} + \underbrace{\rho g \sin(\theta)}_{\text{Gravitational}} + \underbrace{G^2 \frac{d}{dz}\left(\frac{1}{\rho}\right)}_{\text{Accelerational}} \tag{C.8}$$

As seen in equation (C.8) the total pressure gradient consists of a frictional, gravitational and accelerational pressure gradient. Depending on the two-phase model used, these expressions can be derived differently. For the homogeneous model the pressure gradient is given as [Olesen, 2015]:

$$-\frac{dp}{dz} = \tau_h \frac{P}{A} + \rho_h g \sin(\theta) + G^2 \frac{d}{dz}\left(\frac{1}{\rho_h}\right) \tag{C.9}$$

$$-\frac{dp}{dz} = \frac{2}{d} f_h \frac{G^2}{\rho_h} + \rho_h g \sin(\theta) + G^2 \frac{d}{dz}\left(\frac{1}{\rho_h}\right) \tag{C.10}$$

In equation (C.9), the two momentum conservation equations are summarised, and the no-slip condition is applied between the true phase velocities so: $U_h = U_l = U_g$. In equation (C.10) the model is based on a pipe diameter D, circumference $P = \pi D$, cross-sectional area $A = \frac{\pi}{4} D^2$ and the mixture Darcy friction factor, f_h, which depends upon the mixture Reynolds number Re_h, mixture density, ρ_h and mixture viscosity, μ_h. The latter two depend upon the mass quality. In the homogeneous model the frictional and accelerational gradients can be written in the forms [Olesen, 2015]:

$$\left(\frac{dp}{dz}\right)_F = \tau_g \frac{P_g}{A_g} + \tau_l \frac{P_l}{A_l} = \tau_h \frac{P}{A} = f_h \frac{1 G^2 P}{2 \rho_h A} \tag{C.11}$$

$$\left(\frac{dp}{dz}\right)_A = \frac{d}{dz}(G_g U_G + G_l U_l) = G^2 \frac{d}{dz}\left(\frac{1}{\rho}\right) \tag{C.12}$$

C.3.1 Two-Phase Multipliers

Two-phase pressure gradients can also be expressed by two-phase multipliers [Whalley, 1996]:

Two-phase Pressure Gradient	=	Single-Phase Pressure Gradient	x	Two-phase Multiplier

which for the frictional pressure gradient corresponds to:

$$-\left(\frac{dp}{dz}\right)_F = \left(\frac{dp}{dz}\right)_{Fl} \text{ x } \Phi_l^2 \tag{C.13}$$

$$-\left(\frac{dp}{dz}\right)_F = \left(\frac{dp}{dz}\right)_{Fg} \text{ x } \Phi_g^2 \tag{C.14}$$

where Φ^2 is the two-phase multiplier, which is a factor that $-(dp/dz)$ for the single-phase has to be multiplied with in order to get the the two-phase pressure gradient based on a flow of liquid or gas alone.

D Elaboration on the Theory Applied in the Lumped-Mass-Model

This appendix elaborates the heat transfer theory along with Euler's method used in the Lumped-Mass-Model.

D.1 Heat and Heat Transfer

The energy in excess is stored as heat in the TES system through several heat transfer mechanisms. In this chapter the theory of the mechanisms are described. Heat is defined as "*the form of energy that can be transferred from one system to another as a result of temperature difference*" and due to the second law of thermodynamics heat transfer will always occur in the direction of the lowest temperature. The energy balance can generally be described by [Cengel et al., 2012]:

$$\dot{Q} = \dot{m} \cdot \bar{c}_p \cdot (T_2 - T_1) \tag{D.1}$$

where $\dot{m}$ is the mass flow rate, $\bar{c}_p$ is the mean specific heat capacity, T_1 is the initial temperature and T_2 is the final temperature. Equation (D.1) can also be written based on enthalpies:

$$\dot{Q} = \dot{m} \cdot (H_2 - H_1) \tag{D.2}$$

where H_1 is the initial enthalpy value and H_2 is the final enthalpy value. Heat can be transferred through three different mechanisms: convection, conduction and radiation [Cengel et al., 2012]. The three mechanisms and their influence on the TES system are described in the following sections.

D.2 Conduction

Conduction is defined as "*the transfer of energy from the more energetic particles of a substance to the adjacent less energetic ones as a results of interactions between the particles*" [Cengel et al., 2012] and can take place in either solids, liquids or gases. In the case of the TES system, conduction occurs within the concrete, a single solid and further between the pipe and concrete, two different solids. This is further illustrated in Figure 7.1 page 29. In general heat conduction is described as:

$$\dot{Q}_{cond} = k \cdot A_s \cdot \frac{dT}{dx} \tag{D.3}$$

where k is the thermal conductivity of the solid material, A_s is the heat transfer surface area, T is the temperature and x is the layer thickness. From the expression it is seen that the rate of heat conduction through a plane layer is proportional to the heat transfer area and the temperature different across the layer but inversely proportional to the layer thickness. Equation (D.3) is also known as "Fourier's law of heat conduction".

D.3 Convection

Convection is defined as "*the mode of energy transfer between a solid surface and the adjacent liquid or gas that is in motion*" [Cengel et al., 2012], and is a heat transfer mechanism encountered in the storage, as the HTF flows through pipes in the concrete. Convection thereby occurs between the

HTF and the piping, and heat is transferred from the pipes to the HTF. This is further illustrated in Figure 7.2 page 29. In general heat convection is described as:

$$\dot{Q}_{conv} = h \cdot A_s \cdot (T_s - T_\infty) \tag{D.4}$$

where h is the convection heat transfer coefficient, A_s is the surface area, T_s is the surface temperature and T_∞ is the temperature sufficiently far from the surface. Equation (D.4) is also known as "Newton's law of cooling" [Cengel et al., 2012].

D.4 Radiation

Radiation is defined as "*the energy emitted by matter in the form of electromagnetic waves (or photons) as a result of the changes in the electronic configurations of the atoms or molecules*" [Cengel et al., 2012]. Thermal radiation is the form of radiation that is emitted by bodies because of their temperature, and this type of radiation is typically of interest in heat transfer studies. In the case of the TES system, however, thermal radiation is neglected, since the effects of radiation in concrete are assumed very small compared to the former two heat transfer mechanisms.

D.5 Euler's Method

In the equations (10.18) and (10.19) page 45 it is seen that the method used for finding the HTF and concrete energies at the next time is Euler's method. Euler's method is commonly seen in equation (D.5) [Lund and Condra, 2014]. The method, however, needs a relatively small time step to achieve an acceptable accuracy as illustrated in Figure D.1.

$$y_{n+1} = y_n + h \cdot f(x_n, y_n) \tag{D.5}$$

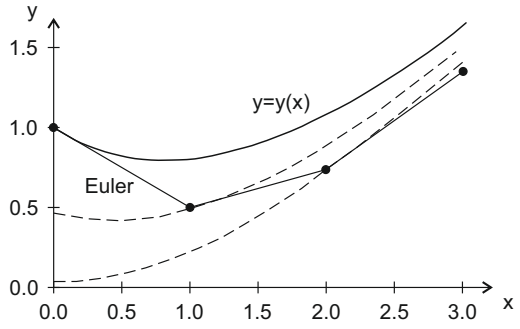

Figure D.1. Illustration of Euler's method [Lund and Condra, 2014].

where y_n is the current value, h is the time step, $f(x_n, y_n)$ is the derivative at the current value and y_{n+1} is the value at the new time. Euler's method is known to be the simplest method when solving first order differential equations.

From Figure D.1 it is seen that with a time step of $h = 1.0$ Euler's method is very inaccurate compared to the exact solution $y = y(x)$. In order to get a more accurate solution, the time step used must be smaller, *e.g.* $h = 0.5$ or $h = 0.1$. Euler's method is a first order method of $O(h^1)$ [Lund and Condra, 2014], and the method related to the equations (10.18) and (10.19) page 45 are seen in Table D.1.

Method	**Expression**						
Euler	y_{n+1}	$=$	y_n	$+$	h	$\cdot$	$y_n^{'}$
	$\text{Wat.E}^{(\text{it}+1)}$	$=$	$\text{Wat.E}^{(\text{it})}$	$+$	dt	$\cdot$	$\frac{\text{dEelem}^{(\text{it})}}{\text{dt}}$

Table D.1. Euler's method applied.

E Elaboration on the FVM-Theory and Model

This appendix elaborates the general FVM-theory in 1D and presents the derived 2D-model equations used in the FVM-Model along with the grid independence study.

E.1 The Finite Volume Method in 1D

The Finite Volume Method (FVM) is a method in which an unknown state variable φ, *e.g.* temperature, is approximated by integration of the governing equations over all finite control volumes. The FVM has advantages in handling derivative boundary conditions, discontinuous source terms and complex geometries [Lund and Condra, 2014]. Overall, the method requires the following steps [Versteeg and Malalasekera, 2007]:

1. Grid generation
2. Discretisation
3. Solution of equations

These steps are elaborated in the following.

E.1.1 Grid Generation

The first step in the FVM is to divide the investigated domain into discrete control volumes. This is typically done by placing nodal points in the domain as seen in Figure E.1 [Versteeg and Malalasekera, 2007]. In general, the system of notation used is given in Figure E.2 [Versteeg and Malalasekera, 2007].

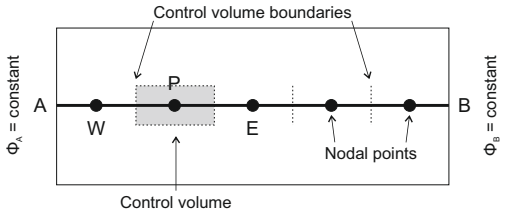

Figure E.1. FVM grid generation in 1D, inspired by [Versteeg and Malalasekera, 2007].

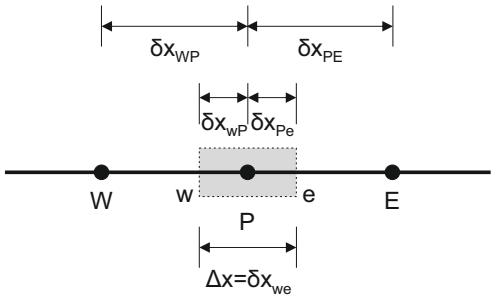

Figure E.2. System of notation in 1D, inspired by [Versteeg and Malalasekera, 2007].

From Figure E.1 it is seen that several nodal points are placed, equally spaced, between the end points A and B. It is also seen that the faces of each control volume are placed midway between adjacent nodes, which implies that each node is surrounded by a control volume, *i.e.* a cell (seen in grey). The end points A and B are placed at the outwards faces of the outermost control volumes. For the domain defined in Figure E.1, steady state diffusion is governed by [Versteeg and Malalasekera, 2007]:

$$\frac{d}{dx}\left(\Gamma\frac{d\varphi}{dx}\right)+S=0 \tag{E.1}$$

where Γ is the diffusion coefficient and S is the source term.

Figure E.2 shows that the nodal point investigated is termed P, while its x-directional neighbours are termed W (western neighbour) and E (eastern neighbour). The faces of the control volume surrounding P is termed w and e, corresponding to the neighbouring points. Additionally, it is seen that δx-distances are named according to the left and right boundaries. The control volume width is seen to equal the distance between the western face and the eastern face of the control volume: $\Delta x = \delta x_{we}$ [Versteeg and Malalasekera, 2007].

E.1.2 Discretisation

The key in the FVM is the discretisation, which converts the integral equations into a system of algebraic equations to be solved. The control volume integration express the exact conservation of the state variable of interest, φ, in integral form for a finite cell size [Lund and Condra, 2014]. For the domain seen in Figure E.1, the following equation can be developed [Versteeg and Malalasekera, 2007]:

$$\int_{\Delta V} \frac{d}{dx}\left(\Gamma \frac{d\varphi}{dx}\right) dV + \int_{\Delta V} S dV = \left(\Gamma A \frac{d\varphi}{dx}\right)_e - \left(\Gamma A \frac{d\varphi}{dx}\right)_w + \bar{S}\Delta V = 0 \tag{E.2}$$

where ΔV is the control volume and A is the cross-sectional area. Equation (E.2) is a balance equation for the control volume and implies that the diffusive flux of φ leaving the east face minus the diffusive flux of φ entering the west face equals the generation of φ.

The above can be rearranged to:

$$\Gamma_e A_e \left(\frac{\varphi_E - \varphi_P}{\delta x_{PE}}\right) - \Gamma_w A_w \left(\frac{\varphi_P - \varphi_W}{\delta x_{WP}}\right) + (S_u + S_P \varphi_P) = 0 \tag{E.3}$$

$$\Downarrow$$

$$\left(\frac{\Gamma_e}{\delta x_{PE}} A_e + \frac{\Gamma_w}{\delta x_{WP}} A_w - S_P\right) \varphi_P = \left(\frac{\Gamma_w}{\delta x_{WP}} A_w - S_P\right) \varphi_W + \left(\frac{\Gamma_e}{\delta x_{PE}} A_e\right) \varphi_E + S_u \tag{E.4}$$

$$\Downarrow$$

$$a_P \varphi_P = a_W \varphi_W + a_E \varphi_E + S_u \tag{E.5}$$

where the coefficients a_P, a_W and a_E are:

$$a_P = a_W + a_E - S_P \quad \text{(E.6)} \qquad a_W = \frac{\Gamma_w A_w}{\delta x_{WP}} \quad \text{(E.7)} \qquad a_E = \frac{\Gamma_e A_e}{\delta x_{PE}} \quad \text{(E.8)}$$

The equations (E.1) through (E.5) are correspondingly extended to 2D [Versteeg and Malalasekera, 2007]:

$$\frac{\partial}{\partial x}\left(\Gamma \frac{\partial \varphi}{\partial x}\right) + \frac{\partial}{\partial y}\left(\Gamma \frac{\partial \varphi}{\partial y}\right) + S_\varphi = 0 \tag{E.9}$$

$$\Downarrow$$

$$\int_{\Delta V} \frac{\partial}{\partial x}\left(\Gamma \frac{\partial \varphi}{\partial x}\right) dxdy + \int_{\Delta V} \frac{\partial}{\partial y}\left(\Gamma \frac{\partial \varphi}{\partial y}\right) dxdy + \int_{\Delta V} S dV = 0 \tag{E.10}$$

$$\Downarrow$$

$$a_P \varphi_P = a_W \varphi_W + a_E \varphi_E + a_N \varphi_N + a_S \varphi_S + S_u \tag{E.11}$$

where a_W and a_E are as given in equations (E.7) and (E.7) page 120, while

$$a_P = a_W + a_E + a_N + a_S - S_P \quad \text{(E.12)} \qquad a_N = \frac{\Gamma_n A_n}{\delta x_{PN} A_n} \quad \text{(E.13)} \qquad a_S = \frac{\Gamma_s A_s}{\delta x_{SP} A_e} \quad \text{(E.14)}$$

E.1.3 Solution of Equations

Discretised equations in the form given in equation (E.5) are set up for each nodal point in order to solve the problem. The resulting system of linear algebraic equations can then be solved to obtain the distribution of φ at the nodal points [Versteeg and Malalasekera, 2007].

E.2 Discretisation Schemes

In section 8.2.1 page 34 the weighting parameter θ is presented. When the θ-values seen in the equations (8.7), (8.8) and (8.9) are used, the scheme is commonly referred to as the "explicit scheme", the "Crank-Nicolson scheme" and the "fully implicit scheme", respectively [Versteeg and Malalasekera, 2007].

E.2.1 The Explicit Scheme

When substituting $\theta = 0$ into equation (8.12), the following is obtained:

$$a_P T_P = a_W T_W^0 + a_E T_E^0 + [a_P^0 - (a_W - a_E - S_P]T_P^0 + S_u \tag{E.15}$$

since the source term is linearised as $b = S_u + S_P T_P^0$. The right hand side of the equation only contains values at the previous time step, t. This means that the left hand side is calculated by going forward in time. The equation requires that all coefficients are positive for physically realistic and bounded results. This is fulfilled if:

$$a_P^0 - a_W - a_E > 0 \Rightarrow \rho c \frac{\Delta x}{\Delta t} - \frac{k_w}{\delta x_{WP}} - \frac{k_e}{\delta x_{PE}} > 0 \tag{E.16}$$

For a constant k-value and a uniform grid, the above reduces to:

$$\rho c \frac{\Delta x}{\Delta t} - \frac{2k}{\delta x} > 0 \Rightarrow \Delta t < \rho c \frac{(\Delta x)^2}{2k} \tag{E.17}$$

The above sets a maximum time step size limit that means it becomes relatively expensive to improve the accuracy in space. It is seen that the possible maximum time step needs to be reduced with Δx squared, which is a serious limitation for the explicit scheme.

E.2.2 The Crank-Nicolson Scheme

When substituting $\theta = \frac{1}{2}$ into equation (8.12), the following is obtained:

$$a_P T_P = a_W \left[\frac{T_E + T_E^0}{2}\right] + a_E \left[\frac{T_W + T_W^0}{2}\right] + \left[a_P^0 - \frac{a_W}{2} - \frac{a_E}{2}\right] T_P^0 + S_u + \frac{1}{2} S_P T_P^0 \tag{E.18}$$

since the source term is linearised as $b = S_u + \frac{1}{2} S_P T_P + \frac{1}{2} S_P T_P^0$. It is seen that this method is implicit, since more than one unknown temperature at the next time step is present. This induces that simultaneous equations for all node points need to be solved at each time step. Also for this scheme, it is important to ensure that all coefficients are positive. This is fulfilled if:

$$a_P^0 > \left[\frac{a_W + a_E}{2}\right] \Rightarrow \Delta t < \rho c \frac{\Delta x^2}{k} \tag{E.19}$$

Compared to the inequality given in (E.17), the inequality in (E.19) is seen to be less restrictive, since only x is squared.

E.2.3 The Fully Implicit Scheme

When substituting $\theta = 1$ into equation (8.12), the following is obtained:

$$a_P T_P = a_W T_W + a_E T_E + a_P^0 T_P^0 + S_u \tag{E.20}$$

since the source term is linearised as $b = S_u + S_P T_P$. It is seen that both sides of equation (E.20) contains temperatures at the next time step, $t + \Delta t$. This means that a system of algebraic equations must be solved at each time step starting with a given initial temperature field of T^0.

Additionally, it is seen that all coefficients are positive. This means that the implicit scheme is unconditionally stable for any size of time step.

E.3 Model Equations

The equations used for the development of the FVM-Model are given in the following. The equations are implemented in the matrix, K, and the vector, Q, in equation (11.3) page 57.

No.	Equation
I	$\left(\frac{\rho c\Delta x}{\Delta t} + \frac{4\theta k}{\Delta x}\right) T_P = \frac{\theta k}{\Delta x}(T_E + T_W + T_N + T_S) + (1-\theta)\frac{k}{\Delta x}(T_E^0 + T_W^0 + T_N^0 + T_S^0) + \left(\frac{\rho c\Delta x}{\Delta t} - (1-\theta)\frac{4k}{\Delta x}\right) T_P^0$
II	$\left(\frac{\rho c\Delta x}{\Delta t} + \frac{2\theta k}{\Delta x}\right) T_P = \frac{\theta k}{\Delta x}(T_E + T_S) + (1-\theta)\frac{k}{\Delta x}(T_E^0 + T_S^0) + \left(\frac{\rho c\Delta x}{\Delta t} - (1-\theta)\frac{2k}{\Delta x}\right) T_P^0$
III	$\left(\frac{\rho c\Delta x}{\Delta t} + \frac{3\theta k}{\Delta x}\right) T_P = \frac{\theta k}{\Delta x}(T_E + T_W + T_S) + (1-\theta)\frac{k}{\Delta x}(T_E^0 + T_W^0 + T_S^0) + \left(\frac{\rho c\Delta x}{\Delta t} - (1-\theta)\frac{3k}{\Delta x}\right) T_P^0$
IV	$\left(\frac{\rho c\Delta x}{\Delta t} + \frac{2\theta k}{\Delta x}\right) T_P = \frac{\theta k}{\Delta x}(T_W + T_S) + (1-\theta)\frac{k}{\Delta x}(T_W^0 + T_S^0) + \left(\frac{\rho c\Delta x}{\Delta t} - (1-\theta)\frac{2k}{\Delta x}\right) T_P^0$
V	$\left(\frac{\rho c\Delta x}{\Delta t} + \frac{3\theta k}{\Delta x}\right) T_P = \frac{\theta k}{\Delta x}(T_W + T_N + T_S) + (1-\theta)\frac{k}{\Delta x}(T_W^0 + T_N^0 + T_S^0) + \left(\frac{\rho c\Delta x}{\Delta t} - (1-\theta)\frac{3k}{\Delta x}\right) T_P^0$
VI	$\left(\frac{\rho c\Delta x}{\Delta t} + \frac{2\theta k}{\Delta x}\right) T_P = \frac{\theta k}{\Delta x}(T_W + T_N) + (1-\theta)\frac{k}{\Delta x}(T_W^0 + T_N^0) + \left(\frac{\rho c\Delta x}{\Delta t} - (1-\theta)\frac{2k}{\Delta x}\right) T_P^0$
VII	$\left(\frac{\rho c\Delta x}{\Delta t} + \frac{3\theta k}{\Delta x}\right) T_P = \frac{\theta k}{\Delta x}(T_E + T_W + T_N) + (1-\theta)\frac{k}{\Delta x}(T_E^0 + T_W^0 + T_N^0) + \left(\frac{\rho c\Delta x}{\Delta t} - (1-\theta)\frac{3k}{\Delta x}\right) T_P^0$
VIII	$\left(\frac{\rho c\Delta x}{\Delta t} + \frac{2\theta k}{\Delta x}\right) T_P = \frac{\theta k}{\Delta x}(T_E + T_N) + (1-\theta)\frac{k}{\Delta x}(T_E^0 + T_N^0) + \left(\frac{\rho c\Delta x}{\Delta t} - (1-\theta)\frac{2k}{\Delta x}\right) T_P^0$
IX	$\left(\frac{\rho c\Delta x}{\Delta t} + \frac{3\theta k}{\Delta x}\right) T_P = \frac{\theta k}{\Delta x}(T_E + T_N + T_S) + (1-\theta)\frac{k}{\Delta x}(T_E^0 + T_N^0 + T_S^0) + \left(\frac{\rho c\Delta x}{\Delta t} - (1-\theta)\frac{3k}{\Delta x}\right) T_P^0$
X	$\left(\frac{\rho c\Delta x}{\Delta t} + \frac{5\theta k}{\Delta x}\right) T_P = \frac{\theta k}{\Delta x}(T_E + T_W + T_N) + \frac{2k}{\Delta x} T_{HTF} + (1-\theta)\frac{k}{\Delta x}(T_E^0 + T_W^0 + T_N^0) + \left(\frac{\rho c\Delta x}{\Delta t} - (1-\theta)\frac{5k}{\Delta x}\right) T_P^0$
XI	$\left(\frac{\rho c\Delta x}{\Delta t} + \frac{5\theta k}{\Delta x}\right) T_P = \frac{\theta k}{\Delta x}(T_E + T_N + T_S) + \frac{2k}{\Delta x} T_{HTF} + (1-\theta)\frac{k}{\Delta x}(T_E^0 + T_N^0 + T_S^0) + \left(\frac{\rho c\Delta x}{\Delta t} - (1-\theta)\frac{5k}{\Delta x}\right) T_P^0$
XII	$\left(\frac{\rho c\Delta x}{\Delta t} + \frac{5\theta k}{\Delta x}\right) T_P = \frac{\theta k}{\Delta x}(T_E + T_W + T_S) + \frac{2k}{\Delta x} T_{HTF} + (1-\theta)\frac{k}{\Delta x}(T_E^0 + T_W^0 + T_S^0) + \left(\frac{\rho c\Delta x}{\Delta t} - (1-\theta)\frac{5k}{\Delta x}\right) T_P^0$
XIII	$\left(\frac{\rho c\Delta x}{\Delta t} + \frac{5\theta k}{\Delta x}\right) T_P = \frac{\theta k}{\Delta x}(T_W + T_N + T_S) + \frac{2k}{\Delta x} T_{HTF} + (1-\theta)\frac{k}{\Delta x}(T_W^0 + T_N^0 + T_S^0) + \left(\frac{\rho c\Delta x}{\Delta t} - (1-\theta)\frac{5k}{\Delta x}\right) T_P^0$

F Estimated TES System Material Costs

In this appendix an overview of the estimated material costs for the TES system is given. It should be noted that only the costs of the pipes and concrete are considered. Assembly, man-hours etc. are not considered. The costs are summarised in Table F.1.

Material	Amount	Cost (DKK)	Total Cost (DKK)
Steel pipe (Ø100 4 mm)	25 x 12 m	225 DKK/m	67500
Cement	475 x 25 kg	50 DKK/unit	23750
Sand/stone mixture	55 m^3 = 93.5 ton	1300 DKK/ton	121550
Total cost			***212,800***

Table F.1. Overview of estimated material costs for the TES system.

In Table F.1 the costs of the pipes are seen to be 225 DKK/m [Christansen, 2017] corresponding to a total cost of 67500 DKK for 25 x 12 m pipes. It is also seen that the cost of a 25 kg bag of cement is 50 DKK/unit [Optimera, 2017] corresponding to a total cost of 23750 DKK for 475 x 25 kg cement. The cost of 1 ton sand/stone mixture is 1300 DKK/ton [Nemgrus, 2017] corresponding to a total cost of 121550 DKK for 93.5 ton sand/stone mixture. In total this results in a cost of 212800 DKK for the material used to produce the TES system modelled.

It is assessed, that when doubling the size of the TES system, as investigated Chapter 14, the material costs will double as well, since the number of pipes and amount of concrete is doubled.